

FREE CARRIERS IN NANOCRYSTALLINE TITANIUM DIOXIDE THIN FILMS

THÈSE N° 2934 (2004)

PRÉSENTÉE À LA FACULTÉ SCIENCES DE BASE

Institut de physique de la matière complexe

SECTION DE PHYSIQUE

ÉCOLE POLYTECHNIQUE FÉDÉRALE DE LAUSANNE

POUR L'OBTENTION DU GRADE DE DOCTEUR ÈS SCIENCES

PAR

Simon SPRINGER

physicien diplômé de l'Université de Bâle
de nationalités suisse et américaine et originaire de Bâle (BS)

acceptée sur proposition du jury:

Dr P.E. Schmid, directeur de thèse
Prof. A. Pignolet, rapporteur
Dr D. Rosenfeld, rapporteur
Prof. P. Stadelmann, rapporteur

Lausanne, EPFL
2004

To my parents, Anita and Mirjam.

Abstract

This thesis analyzes the properties of heavily doped nanocrystalline titanium dioxide. Thin films were deposited by magnetron sputtering with either water vapor as reactive gas or a periodically interrupted oxygen supply. The samples were at the same time electrically conducting and transparent. They consisted of mixtures of rutile, anatase and amorphous phases.

Titanium dioxide is chemically stable, hard, non-toxic, transparent, and inexpensive. Due to a high refractive index it is often found in optical applications as a thin film coating. For many purposes it is interesting to take advantage of a combination of good transparency and electrical conductivity. An even larger field of applications would open if the electric conductivity of TiO_2 could be increased in a controlled manner. Conventional bulk doping is limited, however, by low solubility limits. Highly conducting nanocrystalline TiO_2 thin films have been obtained recently by sputtering in presence of water vapor. The present project intends to elucidate the doping mechanisms at work in such films. In addition, an alternative process to achieve grain-boundary doping of TiO_2 was explored.

Spectrophotometry over a wide spectral range (0.05 to 5 eV) was the main tool in probing the mobile electrical charge carriers. The interpretation of these optical measurements required appropriate models. The models developed took many structural properties into account, such as thickness, surface roughness, density, anisotropy and crystalline phase composition. The phase and morphology of the films were analyzed by X-ray diffraction and reflection, scanning probe microscopy, and electron microscopy. The chemical analyses included electron-probe microanalyses, Rutherford backscattering and elastic recoil detection analysis. The DC electrical properties were measured between room temperature and 250 °C.

Most water-deposited samples showed semiconducting behavior with an activation energy of the order of 100 meV. The optical measurements revealed a broad absorption band around 1 eV. The absorption coefficient scaled with conductivity. It was successfully modelled as a Lorentzian. Similar absorption bands have been reported for reduced rutile and anatase single crystals.

Water-deposited samples containing anatase exhibited a metallic behavior. In these samples the thermal activation energy was reduced to about 30 meV and the charge carriers displayed a high mobility ($3 \text{ cm}^2\text{V}^{-1}\text{s}^{-1}$). The infrared absorption band was about 10 times less important than in the samples devoid of anatase.

Thin films of TiO_2 intercalated with the equivalent of nanometer-thick layers of Ti were prepared. By changing the period in the oxygen supply the grain size, and thereby the film properties, could be modified. The films obtained in this way had many properties in common with water-deposited films. They showed the same absorption band in the infrared, had comparable charge carrier densities and were electrically conductive (10^2 to 10^4 Sm^{-1} at room temperature). To our knowledge, this was the first time that such high electrical conductivities were achieved by sputtering in an oxygen plasma.

Résumé

Ce travail analyse les propriétés du dioxyde de titane nanocristallin hyper-dopé. Des films minces ont été déposés par pulvérisation cathodique en présence de vapeur d'eau ou sous un flux d'oxygène périodiquement interrompu. Les films produits sont en même temps conducteurs et transparents. Ils sont constitués des phases rutile, anatase et dioxyde amorphe.

Le dioxyde de titane est chimiquement stable, dur, non toxique, transparent et bon marché. Grâce à son indice de réfraction élevé, il est souvent utilisé dans des applications optiques. Pour différentes applications, il est intéressant de tirer avantage de la combinaison d'une bonne transparence et d'une bonne conductivité électrique. Le champ des applications pourrait s'élargir si la conductivité électrique du TiO_2 pouvait être augmentée de façon contrôlée. Le dopage conventionnel dans la masse est cependant limité par une trop faible solubilité dans ce matériau. Des films fins nanocristallins de TiO_2 hautement conducteurs ont été obtenus récemment par pulvérisation en présence de vapeur d'eau. Le projet présenté ici tente d'élucider les mécanismes de dopage actifs dans de tels films. En outre, une alternative dans la réalisation de dopage aux joints de grain de TiO_2 a été explorée.

La spectrophotométrie sur un large spectre (0.05 à 5 eV) a été le principal outil pour caractériser les propriétés des porteurs de charge électrique. L'interprétation des mesures optiques demande l'élaboration de modèles appropriés. Les modèles développés prennent en compte des propriétés structurales telles que l'épaisseur, la rugosité de surface, la densité, l'anisotropie et le degré de cristallinité. La structure cristalline et la morphologie des films ont été analysées par diffraction et réflexion des rayons X, par microscopies à sonde atomique (STM, AFM) et par microscopie électronique. Les analyses chimiques comprennent la microsonde électronique, la rétro-diffusion de Rutherford et l'analyse par détection du recul élastique. Les propriétés électriques ont été mesurées entre la température ambiante et 250 °C.

La plupart des films déposés en présence de vapeur d'eau présentent un comportement semi-conducteur avec une énergie d'activation de l'ordre de 100 meV. Les mesures optiques révèlent une large bande d'absorption autour de 1 eV. Le coefficient d'absorption augmente avec la conductivité. Ceci a été modélisé avec succès par une Lorentzienne. Des bandes d'absorption similaires ont été observées dans des monocristaux réduits de rutile et d'anatase.

Les films déposés en présence de vapeur d'eau et contenant de l'anatase présentent un comportement métallique. Dans ces films, l'énergie d'activation thermique était d'environ 30 meV et les porteurs de charge sont caractérisés par une grande mobilité ($3 \text{ cm}^2\text{V}^{-1}\text{s}^{-1}$). La bande d'absorption dans l'infra-rouge était à peu près 10 fois moins importante que dans les films dépourvus d'anatase.

Des films minces de TiO_2 intercalés par des couches d'épaisseur nanométrique de Ti ont été déposés. En modifiant périodiquement l'alimentation en oxygène, la taille des grains et par conséquent les propriétés du film ont été modifiées. Les films ainsi obtenus ont un grand nombre de propriétés en commun avec les films déposés en présence de vapeur d'eau. Ils présentent la même bande d'absorption dans l'infra-rouge et des densités comparables de porteurs de charge. Ils sont conducteurs (de 10^2 à 10^4 Sm^{-1} à la température ambiante). A notre connaissance, c'est la première fois que des conductivités électriques aussi élevées sont obtenues par pulvérisation dans un plasma d'oxygène.

Kurzfassung

Die vorliegende Dissertation untersucht die Eigenschaften von stark dotiertem nanokristallinem Titandioxid. Mittels reaktiver Magnetron-Kathodenzerstäubung wurden dünne Schichten abgeschieden. Als Reaktivgas wurde Wasserdampf oder periodisch zugeführter Sauerstoff verwendet. Die Proben waren sowohl elektrisch leitend als auch transparent. Die Schichten bestanden aus einer Mischung von Rutil, Anatase und amorphen Anteilen.

Titandioxid ist chemisch stabil, hart, ungiftig, transparent und preiswert. Wegen seinem hohen Brechungsindex findet man es oft als dünne Schichten in optischen Anwendungen. Für viele Verwendungszwecke ist eine Kombination von guter optischer Transparenz und elektrischer Leitfähigkeit von Vorteil. Ein noch breiteres Anwendungsfeld lässt sich erschliessen, falls die elektrische Leitfähigkeit von Titandioxid auf kontrollierte Art erhöht werden kann. Die Dotierung des Kristallvolumens ist jedoch beschränkt durch niedere Löslichkeit. Vor kurzem sind hochleitende nanokristalline dünne Schichten aus Titandioxid mittels Kathodenzerstäubung mit Wasserdampf hergestellt worden. Das vorliegende Projekt untersucht die Dotierungsmechanismen in solchen Schichten. Ausserdem wurde ein alternativer Prozess zum Erhalt von über die Korngrenzen dotiertem TiO_2 ausgeleuchtet.

Das wichtigste Mittel zur Untersuchung der elektrischen Ladungsträger war die Spektrophotometrie über einen weiten Spektralbereich (0.05 bis 5 eV). Zur Interpretation dieser Messungen müssen geeignete Modelle entwickelt werden. Die entwickelten Modelle berücksichtigen die Struktur der Proben. Dazu gehören die Schichtdicken, die Oberflächenrauigkeit, die Dichte, die Anisotropie und die Zusammensetzung der kristallinen Phasen. Zur Charakterisierung der Morphologie und Phasenzusammensetzung dienten die Röntgen-Strukturanalyse, Röntgen-Reflektometrie, Raster-Sonden-Mikroskopie und die Elektronen-Mikroskopie. Die chemischen Analysen schlossen Elektronenstrahl-Mikroanalyse, Rutherford-Spektroskopie und 'Elastic Recoil Detection Analysis' mit ein. Die elektrischen Eigenschaften wurden zwischen Raumtemperatur und 250 °C unter Gleichstrom gemessen.

Unter Verwendung von Wasserdampf als Reaktivgas waren die meisten Schichten halbleitend mit einer Aktivierungsenergie nahe 100 meV. Die optischen Messungen zeigten ein breites Absorptionsband bei 1 eV. Dieses nahm mit zunehmender Leitfähigkeit zu. Mit einem Lorentzbeitrag hat sich die Absorption erfolgreich modellieren lassen. Ähnliche Absorptionsbänder sind in Rutil- und Anatase-Kristallen beobachtet worden.

Die Anatase enthaltenden und mit Wasserdampf hergestellten Proben zeigten elektrische Eigenschaften eines Metalles. Die Aktivierungsenergie war auf etwa 30 meV reduziert, und die Ladungsträger hatten eine hohe Mobilität ($3 \text{ cm}^2\text{V}^{-1}\text{s}^{-1}$). Das Absorptionsband im infraroten Spektralbereich war zehnmal schwächer als das Band in den Proben ohne Anatase.

Dünne Titandioxidschichten mit nanometer-dicken Titan-Zwischenlagen sind abgeschieden worden. Durch Wechsel in der Periode der Sauerstoffzufuhr konnten die Korngrösse und damit die Filmeigenschaften beeinflusst werden. Solche Schichten hatten ähnliche Eigenschaften wie die mit Wasserdampf hergestellten Schichten. Sie zeigten ein ähnliches Absorptionband im Infrarotbereich, eine vergleichbare Dichte von Ladungsträgern und waren elektrisch leitend (10^2 bis 10^4 Sm^{-1} bei Zimmertemperatur). Das war unseres Wissens das erste Mal, dass eine solch hohe Leitfähigkeit durch Kathodenzerstäubung mit einem Sauerstoffplasma erreicht worden ist.

Contents

<i>Chapter 1</i>	Introduction	1
<i>Chapter 2</i>	Properties of TiO ₂	7
2.1	Crystal structure.....	7
2.2	Electrical properties	9
2.3	Optical properties.....	11
<i>Chapter 3</i>	Sample preparation.....	17
3.1	Reactive magnetron sputtering	17
3.1.1	Residual vacuum.....	17
3.1.2	Process gases.....	18
3.1.3	Magnetron targets	18
3.1.4	Power supply and electrical circuit	19
3.2	Substrate.....	19
3.3	Process monitoring	20
<i>Chapter 4</i>	Characterization techniques	23
4.1	Morphology	23
4.1.1	Profilometry	23
4.1.2	X-ray diffraction	23
4.1.2.1	Phase composition	23
4.1.2.2	Grain size.....	24
4.1.3	X-ray reflectivity.....	25
4.1.4	Atomic force microscopy.....	26
4.1.5	Scanning tunneling microscopy	26
4.1.6	Scanning electron microscopy	26
4.1.7	Transmission electron microscopy	27
4.2	Chemical composition	27
4.2.1	Electron probe microanalysis.....	27
4.2.2	Rutherford backscattering analysis and Elastic recoil detection analysis.....	28
4.2.3	Electron energy loss spectrometry	28
4.3	Electrical properties	29
4.4	Optical properties.....	31
4.4.1	Ellipsometry.....	31
4.4.2	Transmission.....	31
4.4.3	Reflection.....	32
4.4.4	Infrared transmission	32
<i>Chapter 5</i>	Analyzing the optical properties of a thin film	35

<i>Chapter 6</i>	Water vapor as reactive gas.....	39
6.1	Introduction.....	39
6.2	Reactive sputtering with water vapor	40
6.3	Results.....	42
6.3.1	Chemical composition	42
6.3.2	Morphology and crystalline structure	43
6.3.2.1	X-ray diffraction	43
6.3.2.2	SEM observation of the film morphology	46
6.3.2.3	Density determination from RBS and profilometry	46
6.3.2.4	Thickness and density determination from XRR	47
6.3.3	Electrical conductivity	49
6.3.4	Optical properties.....	51
6.3.4.1	Optical model for stoichiometric and insulating TiO ₂	51
6.3.4.2	Absorption in films deposited with H ₂ O vapor	53
6.3.4.3	Optical model for samples containing anatase	58
6.3.5	Absorption and conductivity.....	61
6.4	Discussion.....	63
6.4.1	Charge carrier density	64
6.4.2	Possible models for the IR absorption	65
6.4.3	The anatase content.....	66
6.4.4	Influence of the reactive gas	67
6.5	Conclusions.....	68
<i>Chapter 7</i>	Triple layer structures of TiO ₂	71
7.1	Preparation of TiO ₂ films with Ti-rich interlayers using O ₂ as reactive gas	71
7.2	Results.....	71
7.2.1	Morphology and crystalline structure	72
7.2.1.1	Stratified sample structure	72
7.2.1.2	Crystallinity dependence on interlayer thickness	72
7.2.1.3	TEM cross section of a triple layer structure.....	74
7.2.1.4	X-ray reflectivity of a triple layer structure.....	76
7.2.2	Chemical composition	77
7.2.2.1	RBS depth profile	77
7.2.2.2	EELS chemical composition on the cross section	78
7.2.3	Electrical properties	79
7.2.4	Optical properties.....	81
7.2.4.1	Modelling of the optical properties	82
7.3	Discussion.....	84
7.4	Conclusions.....	85
<i>Chapter 8</i>	Periodicity in the oxygen supply.....	87
8.1	Introduction.....	87
8.2	Sample preparation	87
8.3	Results.....	89
8.3.1	Morphology and crystalline structure	89
8.3.1.1	X-ray diffraction	89
8.3.1.2	Surface characterization by AFM and STM.....	91
8.3.1.3	Cross section characterization by TEM.....	91

8.3.2	Electrical properties	93
8.3.3	Optical properties.....	94
8.3.3.1	Model I: EMA for a stratified structure.....	96
8.3.3.2	Model II: Metallic inclusions arranged in layers.....	97
8.3.3.3	Model III: Homogeneous layer with absorption band.....	99
8.4	Discussion.....	102
8.4.1	Optical and electrical properties	102
8.4.2	Periodicity in process parameters and nanostructure of the films	104
8.5	Conclusions.....	105
<i>Chapter 9</i> Conclusions		107
<i>Appendix A</i> Optical properties of a stratified medium		109
A.1	Definitions	109
A.2	Fresnel coefficients for reflection and transmission at a planar interface between isotropic media	110
A.3	Fresnel coefficients for reflection and transmission at a planar interface perpendicular to the optical axis of two uniaxial media	111
A.4	Matrix formalism for a stratified medium	112
<i>Appendix B</i> Dielectric function of heterogeneous media		115
<i>Appendix C</i> Modelling the dielectric function of a solid		117
<i>Appendix D</i> Optical modelling of the substrates.....		119
<i>Appendix E</i> X-ray reflectivity		121
E.1	Basic concepts of X-ray reflectivity	121
E.1.1	Geometry of the experiment	121
E.1.2	Refractive index in the X-ray range.....	122
E.1.3	Specular and diffuse scans.....	123
E.2	Features in the X-ray reflectivity curve	124
E.2.1	Critical angle and density.....	125
E.2.2	Kiessig fringes and thickness.....	126
E.2.3	Damping and roughness.....	127
E.3	Methods of analysis	127
E.3.1	Data reduction.....	127
E.3.2	Kiessig fringe position	128
E.3.3	Determining thickness and index from the Kiessig fringes	128
E.3.4	Modelling of the XRR curves	129
Acknowledgements.....		131
Curriculum vitae		133

Chapter 1 Introduction

Titanium dioxide is chemically stable, relatively hard, non-toxic, bio-compatible, largely transparent and inexpensive. Its particularities are a high dielectric constant and an interesting photocatalytic activity. It is a wide gap semiconductor with a large range of electrical conductivity depending on its chemical composition. These are reasons why there has been an important research activity on titanium dioxide spanning a vast variety of applications.

Anatase and rutile are the two stable crystalline phases of TiO_2 that are found most often. The crystal structure of rutile was first described by Vegard [1]. Since natural rutile crystals were usually impure, investigations were limited to ceramic samples until the early 1950s. Then, colorless, large single crystals of synthetic rutile were grown by the boule technique [2, 3]. From then on research concentrated on the investigation on optical and electrical properties and their anisotropy as well as on the defect structure of rutile single crystals [2-7]. The chemical composition of the TiO_2 crystals could be changed by annealing in a controlled gas atmosphere [5, 8-11]. In the 1960s several researchers embarked on a discussion about whether the behavior of charge carriers in rutile could be understood by a small polaron model [12-14] or not [15]. It was generally assumed that the properties of anatase would be similar to those of rutile [16]. This was proven wrong by the success of using anatase in a new solar cell concept which was not possible with rutile [17]. With the possibility of growing synthetic anatase single crystals [18] people became interested in the difference between rutile and anatase. As before on rutile, researchers started to investigate systematically electronic and optical properties of anatase [16, 19-24].

The native oxide layer on titanium is about 4 nanometers thick and protects the metal from further oxidation. It consists mostly of rutile and anatase TiO_2 , some Ti_2O_3 and TiO are also possible [25]. Its passivating effect causes high chemical resistance against corrosive environments and it is found for instance on the surface of titanium implants for orthopedic and dental applications [25]. As a powder, the most common application of TiO_2 is as a pigment for providing brightness, whiteness and opacity in many products such as paints, coatings, plastics, paper, inks, fibers, nutrients, toothpaste, and cosmetics [26, 27]. The high refractive index makes it interesting for optical applications [28, 29], including antireflection coatings [30], narrow band filters [31], and optical waveguides [32, 33]. Often the wanted properties are obtained by multilayers of TiO_2 (high refractive index) and SiO_2 (low refractive index) [34]. TiO_2 structures with a large surface are also investigated as gas sensor with selectivity for NO_x , oxygen, different carbon hydrides, and other compounds [35-39]. The surface of TiO_2 acts as a catalyst under illumination with solar light. For instance water pollutants as dissolved organic molecules can be dissociated on TiO_2 surfaces [40-44]. The photoelectrochemical decomposition of water is possible [45]. Gas-phase photocatalysis using TiO_2 nanoporous films has been realized, too [46]. In dye-sensitized solar cells and electrochromic devices titanium dioxide electrodes are used [17, 47, 48]. Porous TiO_2 layer show promising results in solid-state photovoltaic solar cells [49-51]. TiO_2 has been used as a photoelectrochemical anti-corrosion coating material in 1995. The attractiveness of this material is also due to its self-cleaning property [52]. Furthermore, it has been found that the water contact angle for TiO_2 surface changes reversibly to zero degrees upon UV irradiation [53]. This phenomenon has been termed 'superhydrophilicity'. Because of the high

dielectric constant, rutile TiO_2 is investigated as a dielectric material in electronic applications [54]. Local oxidation of titanium thin films by scanning probe microscopes yields a convenient lithographic patterning technique which does not require any etching [55]. Microelectronic elements have been obtained by this technique [56]. TiO_2 films loaded with Ag nanoparticles showed multicolor photochromism. After monochromatic visible light irradiation, these films adopt the corresponding color [57]. A great number of new applications could become possible, such as rewritable color copy paper or high density multi-wavelength optical memories [58]. For optical applications rutile is preferred to anatase because of its higher refractive index. Films should be dense and smooth with as few voids as possible. On the other hand, all the applications related to photocatalytic activity, gas sensing, and solar cells have a preference for anatase due to its higher mobility and its catalytic properties [17, 36, 42]. Here usually porous structures are advantageous because of a large surface to volume ratio. Fabrication techniques of doped or undoped titanate thin films of versatile morphology include sol-gel, chemical vapor deposition (CVD), and physical vapor deposition (PVD) techniques. An overview of the available techniques can be found in [59-61].

The deposition technique used in this work is magnetron sputtering, one of the PVD techniques commonly used for industrial coatings. In this method charged ions are accelerated by an electrical potential drop toward a target electrode. As a result, atoms are expelled from the target and deposited on the substrate. In reactive magnetron sputtering, the presence of a reactive gas allows for instance the deposition of oxidized films from a metallic target. Dense and smooth polycrystalline thin films of sub-stoichiometric TiO_{2-x} are commonly deposited by this method. Magnetron sputtering is often used in industry because it is inexpensive and suitable for large substrates [62].

Titanium dioxide is a wide band-gap semiconductor (3 eV gap). Bulk oxygen vacancies and titanium interstitials are known to generate shallow electron donor levels that contribute to the electric conductivity of TiO_2 [11]. Recent theoretical calculations [63] have proposed that reduced crystal surfaces, too, exhibit donor states close to the bottom of the conduction band. Lately A. Bally [64] replaced oxygen as reactive gas by water vapor. This has led to a remarkable increase in electrical conductivity compared to films deposited with oxygen as reactive gas.

The purpose of this work was to investigate further the electrical and optical properties of such films. Furthermore, a hydrogen-free process to deposit similar films was explored. The influence of hydrogen might be elucidated if such a process was found in which no H_2O was present. Spectrophotometry was the main tool used for probing electrical charge carriers. These optical measurements could only be interpreted by comparing with appropriate models. They took many structural properties into account, such as thickness, surface roughness, density, anisotropy and anatase to rutile ratio. Structural characterizations of the samples were performed, such as X-ray diffraction and reflection, scanning probe microscopy and electron microscopy. Our samples were deposited by magnetron sputtering with either oxygen or water vapor as reactive gas. The films obtained were polycrystalline with a mixture of rutile, anatase, and amorphous phases. In a later stage, stoichiometric dioxide layers were deposited alternately with titanium-rich layers.

The manuscript is divided into nine chapters. The properties of TiO_2 as reported in the literature are summarized in Chapter 2. Chapters 3 and 4 give an overview of the techniques for the sample preparation and characterization, respectively. For every technique the basic

physical principle involved, the quantities measured and the possible sources of errors are presented. Chapter 5 summarizes the basic principles needed for the analysis of the optical measurements. In Chapter 6 a thorough characterization of TiO₂ films deposited with water vapor is presented. The electrical and optical properties of the films were put in relation with the rutile and anatase content of the films. In Chapter 7 a titanium-rich layer was intercalated between two TiO₂ layers. Its influence on the properties of the neighboring oxide layers and interface reactions were investigated. Chapter 8 discusses a hydrogen-free process for obtaining conductive and transparent titanium dioxide thin films. The samples were deposited as Ti/TiO₂ multilayers with many periods. In Chapter 9 a summary and general conclusions are presented. The Appendices A to D contain a collection of equations that support the optical modelling. An introduction to the X-ray reflectivity technique can be found in Appendix E.

Please note that in the text the terms 'TiO₂' and 'titanium dioxide' are generally used for slightly substoichiometric films of the composition TiO_{2-x} with $x < 0.1$ which consist in a mixture of rutile, anatase and amorphous crystalline phases. For clarity, the expression 'film' stands for the whole material deposited on the substrate whereas 'layer' represents one part of a stratified film as they are discussed in Chapters 7 and 8.

References

1. L. Vegard, *Philos. Mag.* **32** (1916), 505.
2. D.C. Cronemeyer, *Phys. Rev.* **87** (1952), 876.
3. R.G. Breckenridge and W.R. Hosler, *Phys. Rev.* **91** (1953), 793.
4. G.H. Johnson, *J. American Ceramic Society* **36** (1953), 97.
5. D.C. Cronemeyer, *Phys. Rev.* **113** (1959), 1222.
6. F.A. Grant, *Reviews of Modern Physics* **31** (1959), 646.
7. H.P.R. Frederikse, *J. Appl. Phys. suppl.* **32** (1961), 2211.
8. V.I. Barbanel and V.N. Bogomolov, *Soviet Physics - Solid State* **11** (1970), 2160.
9. P. Kofstad, *Journal of Less-Common Metals* **13** (1967), 635.
10. M. Henzler and W. Göpel, *Oberflächenphysik des Festkörpers*. 2nd ed., B.G. Teubner, Stuttgart (1994).
11. H.K. Ardakani, *Thin Solid Films* **248** (1994), 234.
12. V.N. Bogomolov, E.K. Kudinov, D.N. Mirlin, and Y.A. Firsov, *Soviet Physics - Solid State* **9** (1968), 1630.
13. V.N. Bogomolov, Y.A. Firsov, E.K. Kudinov, and D.N. Mirlin, *Physica Status Solidi* **35** (1969), 555.
14. V.T. Agekyan and Y.A. Stepanov, *Sov. Phys. Solid State* **17** (1976), 2390.
15. M.I. Klinger, *Phys. stat. sol.* **27** (1968), 479.
16. H. Tang, *Electronic properties of anatase TiO₂ investigated by electrical and optical measurements on single crystals and thin films*. Département de physique, Ecole polytechnique fédérale de Lausanne EPFL, Lausanne (1994).
17. M. Grätzel and B. O'Regan, *Nature* **353** (1991), letters.
18. H. Berger, H. Tang, and F. Lévy, *J. Crystal Growth* **130** (1993), 108.
19. H. Tang, K. Prasad, R. Sanjinés, P.E. Schmid, and F. Lévy, *J. Appl. Phys.* **75** (1994), 2042.
20. R. Sanjinés, H. Tang, H. Berger, F. Gozzo, G. Margaritondo, and F. Lévy, *J. Appl. Phys.* **75** (1994), 2945.
21. H. Tang, F. Lévy, H. Berger, and P.E. Schmid, *Phys. Rev. B* **52** (1995), 7771.
22. N. Hosaka, T. Sekiya, C. Satoko, and S. Kurita, *Journal of the Physical Society of Japan* **66** (1997), 877.
23. T. Sekiya, M. Igarashi, S. Kurita, S. Takekawa, and M. Fujisawa, *Journal of Electron Spectroscopy and Related Phenomena* **92** (1998), 247.
24. T. Sekiya, K. Ichimura, M. Igarashi, and S. Kurita, *Journal of Physics and Chemistry of Solids* **61** (2000), 1237.
25. C.E. Sittig, *Charakterisierung der Oxidschichten auf Titan und Titanlegierungen sowie deren Reaktionen in Kontakt mit biologisch relevanten Modellösungen*, Eidgenössische Technische Hochschule ETHZ, Zürich (1998).
26. W. Clark and P. Broadhead, *Journal of Physics C* **3** (1969), 1047.
27. P. Layman, *Chem. and Eng. News* (1996), 13.
28. M. Radecka, K. Zahrzewska, H. Czternastek, and T. Stapinski, *Applied Surface Science* **65/66** (1993), 227.
29. S. Lee, B.H. Park, and S.-G. Oh, *Journal of the Korean Physical Society* **31** (1997), 352.
30. A.J. Thelen, *Design of Optical Interference Coatings*. McGraw Hill, New York (1989).
31. H.A. Macleod, *Thin-film optical filters*. Adam Hilger Ltd., Bristol (2001).
32. K.L. Siefert and G.L. Griffin, *J. Electrochem. Soc.* **137** (1990), 1206.
33. A.W. Harris, B.P. Ludden, and D.C.W. Blaikley, *Vacuum* **43** (1992), 143.
34. X. Orignac, H.C. Vasconcelos, X.M. Du, and R.M. Almeida, *Journal of Sol Gel Science and Technology* **8** (1997), 1.
35. K. Satake, A. Katayama, H. Ohkoshi, T. Nakahara, and T. Takeuchi, *Sensors and Actuators B* **20** (1994), 111.
36. H. Tang, K. Prasad, R. Sanjinés, and F. Lévy, *Sensors and Actuators B* **26-27** (1995), 71.
37. M.I. Baraton, L. Merhari, J. Wang, and K.E. Gonsalves, *Nanotechnology* **9** (1998), 356.
38. G. Dai, *Sensors and Actuators B* **53** (1998), 8.

39. L. Gao, Q. Li, Z. Song, and J. Wang, *Sensors and Actuators B* **71** (2000), 179.
40. S.N. Frank and A.J. Bard, *J. Am. Chem. Soc.* **99** (1977), 303.
41. T. Sakata and T. Kawai, *Chemical Physics Letters* **80** (1981), 341.
42. A.L. Linsebigler, G. Lu, and J.T. Yates, Jr., *Chem. Rev.* **95** (1995), 735.
43. J.Y. Ying and T. Sun, *Journal of Electroceramics* **1-3** (1997), 219.
44. D. Dumitriu, A.R. Bally, C. Ballif, P. Hones, P.E. Schmid, R. Sanjinés, F. Lévy, and V.I. Pârvulescu, *Applied Catalysis B: Environmental* **25** (2000), 83.
45. A. Fujishima and K. Honda, *Nature* **238** (1972), 37.
46. Y. Ohko, K. Hashimoto, and A. Fujishima, *J. Phys. Chem.* **101** (1997), 8057.
47. M. Grätzel and K. Kalyanasundaram, *Current Science* **66** (1994), 706.
48. P. Bonhôte, J.E. Moser, N. Vlachopoulos, L. Walder, S.M. Zakeeruddin, R. Humphry-Baker, P. Pechy, and M. Grätzel, *Journal of Chemical Society, Chemical Communication* (1996), 1163.
49. S. Siebentritt, K. Ernst, C.-H. Fischer, R. Könenkamp, and M.C. Lux-Steiner. *CdTe and CdS as extremely thin absorber materials in an eta solar cell (ETA)*. in *14th European Photovoltaic Solar Energy Conference*. Barcelona, Spain, (1997).
50. K. Tennakone, G.R.R.A. Kumara, I.R.M. Kottegoda, V.P.S. Perera, and G.M.L.P. Aponsu, *Journal of Physics D: Applied Physics* **31** (1998), 2326.
51. J. Möller, C.-H. Fischer, S. Siebentritt, R. Könenkamp, and M.C. Lux-Steiner. *CuInS₂ as an extremely thin absorber in an eta solar cell*. in *2nd World Conference and Exhibition on Photovoltaic Solar Energy Conversion*. Vienna, (1998).
52. T. Tatsuma, S. Saitoh, Y. Ohko, and A. Fujishima, *Chem. Mater.* **13** (2001), 2838.
53. R. Wang, K. Hashimoto, A. Fujishima, M. Chikuni, E. Kojima, A. Kitamura, M. Shimohigoshi, and T. Watanabe, *Nature* **388** (1977), 431.
54. A.R. Bally, K. Prasad, R. Sanjinés, P.E. Schmid, F. Lévy, J. Benoit, C. Barthou, and P. Benalloul, *Mat. Res. Soc. Symp.* **424** (1997), 471.
55. R.J.M. Vullers, M. Ahlskog, and C. van Haesendonck, *Applied Surface Science* **144-145** (1999), 584.
56. K. Matsumoto, S. Takahashi, M. Ishii, M. Hoshi, A. Kurokawa, S. Ichimura, and A. Ando, *Japanese Journal of Applied Physics* **34** (1995), 1387.
57. Y. Ohko, T. Tatsuma, T. Fuji, K. Naoi, C. Niwa, Y. Kubota, and A. Fujishima, submitted for publication (2003).
58. Y. Ohko, T. Tatsuma, T. Fuji, K. Naoi, C. Niwa, Y. Kubota, and A. Fujishima. *Multicolor photochromism of TiO₂ films loaded with Ag nanoparticles*. in *ECS, Electrochemical society, 203rd meeting*. Paris, (2003).
59. R.F. Bunshah, *Deposition technologies for films and coatings: developments and applications*. 1st ed., Noyes Publications, Park Ridge (1982).
60. R.A. Häfer, *Oberflächen- und Dünnschicht-Technologie*. 1st ed., Springer-Verlag, Berlin (1987).
61. D.L. Smith, *Thin-film deposition: principles and practice*. international ed., McGraw-Hill Inc., (1995).
62. T. Jung, T. Kälber, and V. von der Heide, *Surface and Coatings Technology* **86-87** (1996), 218.
63. A.T. Paxton and L. Thien-Nga, *Phys. Rev. B* **57** (1998), 1579.
64. A. Bally, *Electronic properties of nano-crystalline titanium dioxide thin films*. Département de physique, Ecole polytechnique fédérale de Lausanne EPFL, Lausanne (1999).

Chapter 2 Properties of TiO₂

In Table 2.1 a summary of the most important properties of TiO₂ is given. Reviews of the research on titanium oxides and their properties can be found in [1-4]. More focused on the surface science of metal oxides is the work of Henrich and Cox [5]. Tsuda et al. [6] mostly review the research on electronic properties of rutile. Tang [7] studied the electronic properties of the anatase phase.

2.1 Crystal structure

In nature titanium dioxide crystallizes in three common polymorphs: rutile, anatase and brookite [5, 8, 9]. Moreover, TiO₂ can be observed in additional crystal structures: TiO₂ II: columbite structure [10], TiO₂ III: baddeleyite structure [11, 12], TiO₂ (H): hollandite structure [13], TiO₂ (R): ramsdellite structure [14], and TiO₂ (B) [15]. Many of these phases occur only at very particular conditions, such as high pressure.

Besides an amorphous component, rutile and anatase were the only polymorphs synthesized in the sputtered thin films in this work. Hereafter the description of the properties of titanium dioxide will concentrate on these two phases. Rutile is the most stable phase [16]. Anatase is metastable at room temperature. It transforms irreversibly into rutile upon heating above a threshold temperature. At atmospheric pressure, the transition occurs usually at about 1'000 °C. The critical temperature can vary from 400 °C to 1'200 °C, depending on the grain size, atmosphere, as well as the nature and amount of impurities [17].

Natural rutile crystals exhibit predominantly (110) surfaces [5], and there is agreement on the fact that the (110) stoichiometric surface is the most stable surface for rutile [18, 19]. For anatase the (101) surface is the most stable [4]. The unit cells of the TiO₂ crystal structures are presented in Figure 2.1. In Table 2.1 the unit cell parameters at room temperature are given. The unit cell of rutile contains two Ti atoms situated at (0, 0, 0) and ($\frac{1}{2}$, $\frac{1}{2}$, $\frac{1}{2}$), and four oxygen atoms. The oxygen atoms form a distorted octahedron around every Ti cation. The unit cells of anatase contains four Ti atoms located at (0, 0, 0), ($\frac{1}{2}$, $\frac{1}{2}$, $\frac{1}{2}$), (0, $\frac{1}{2}$, $\frac{1}{4}$), and ($-\frac{1}{2}$, 0, $-\frac{1}{4}$), and eight oxygen atoms. In anatase, too, the Ti cation is surrounded by a distorted oxygen octahedron [20].

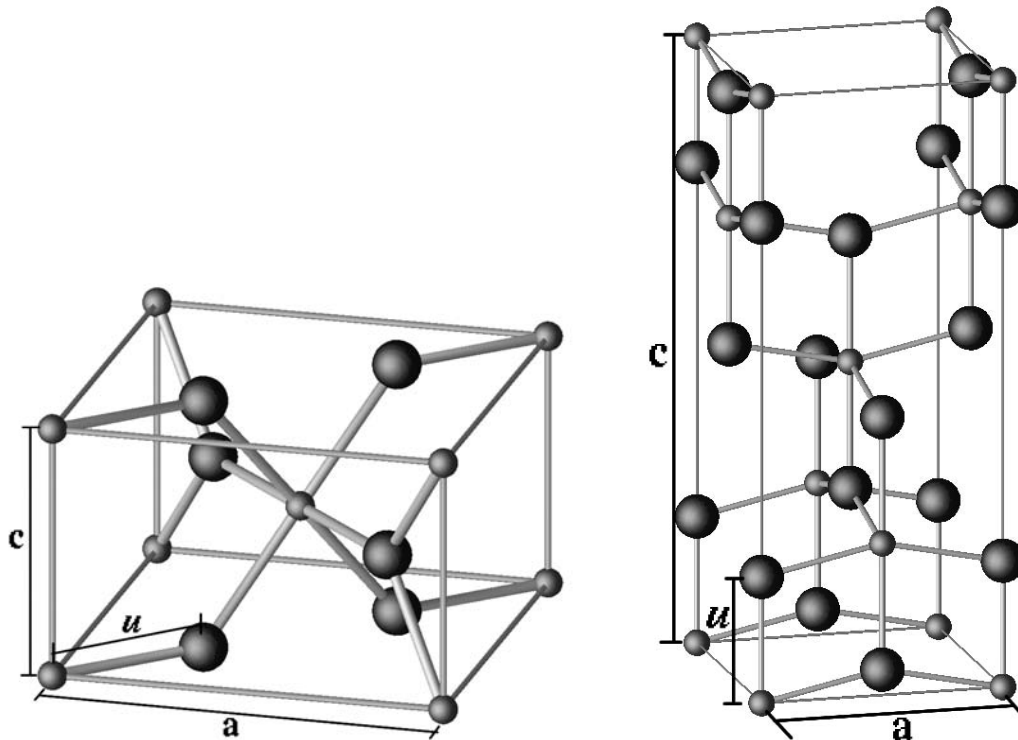


Figure 2.1: Rutile (left) and anatase (right) crystallographic unit cells. Small spheres represent Ti atoms, large spheres represent oxygen atoms (courtesy of G. Cangiani [21]).

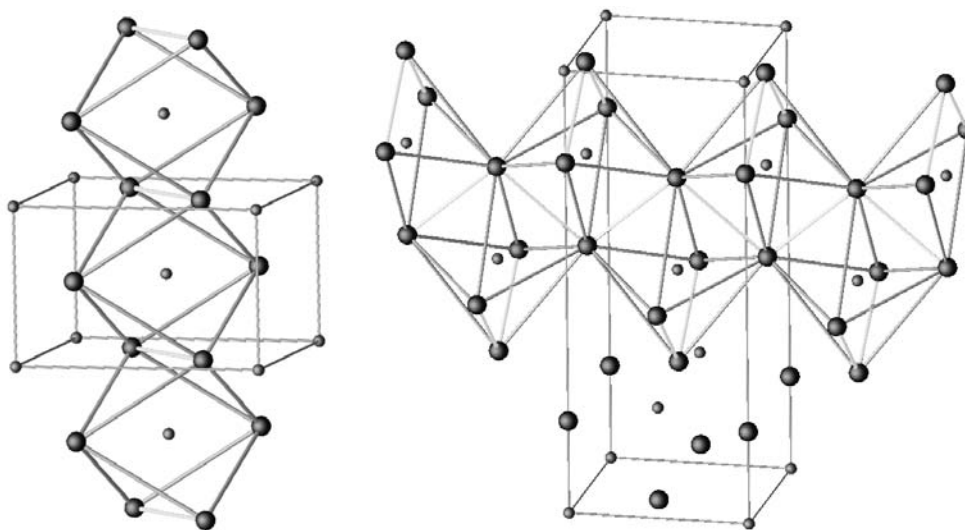


Figure 2.2: Arrangement of TiO₆ octahedra in relation to the unit cells in rutile (left) and anatase (right). Only one chain is shown for each structure. Highlighted bonds are the O-O bonds (courtesy of G. Cangiani [21]).

TiO₆ octahedra constitute the basic building units for the various polymorphic structures of TiO₂. The polymorphs differ from each other by the arrangement and the distortion of the octahedra, confer Figure 2.2. In the rutile crystal each octahedron is connected to 10 neighboring octahedra, among which 2 share an edge and 8 share a corner with it. The edge-shared octahedra are aligned along the [001] direction [22]. In the case of anatase, each octahedron shares 4 edges. The edge-shared octahedra are aligned along the [100] and [010] direction forming zigzag double chains perpendicular to the *c*-axis. These arrangements of

TiO_6 octahedra in rutile and anatase give rise to open channels parallel to the c-axis in rutile and perpendicular to the c-axis in anatase [18].

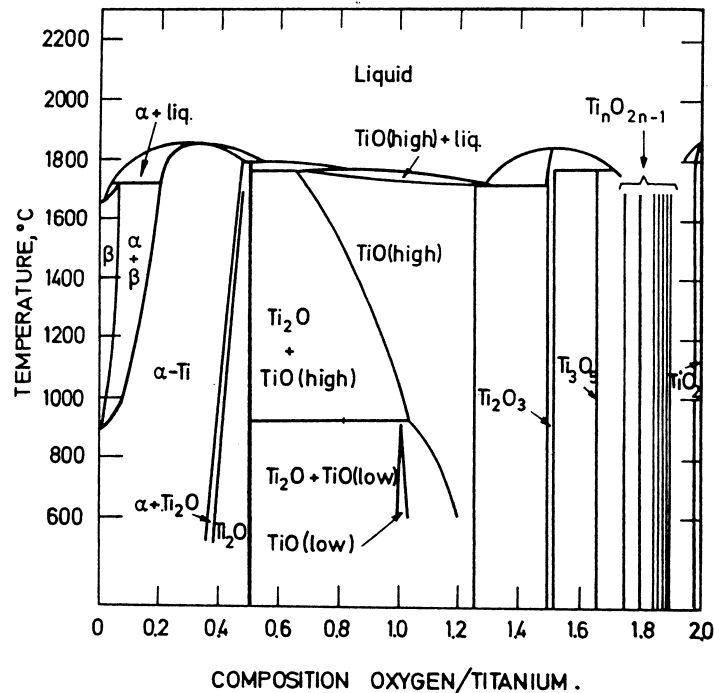


Figure 2.3: The phase diagram of titanium oxides [25].

Figure 2.3 shows the phase diagram of the oxides of titanium. Varying the oxygen content from 0 to 2 oxygen per titanium atom the main phases encountered at room temperature are Ti, Ti_2O , TiO, Ti_2O_3 , Ti_3O_5 and finally TiO_2 . In addition, in between Ti_3O_5 and TiO_2 a series of $\text{Ti}_n\text{O}_{2n-1}$ (with $n \geq 4$) phases can be found. This is the Magnéli series of homologous compounds [23, 24] where physical properties are changed dramatically, ranging from metallic to insulating depending on n . The formation of such reduced oxide phases can be described in terms of the elimination of a plane of oxygen atoms [24]. Magnéli phases with n up to about 38 ($\text{TiO}_{1.974}$) [2] and later up to 61 ($\text{TiO}_{1.984}$) [24] have been reported. This leaves a very narrow homogeneity range for TiO_2 before the lattice tends to break down and the first Magnéli phase appears [2]. To my knowledge, no titanium oxide structure with an oxygen content higher than 2 has been reported.

2.2 Electrical properties

Rutile and anatase are wide band-gap semiconductors with the valence band consisting of O $2p$ states and the conduction band formed of Ti $3d$ states [5, 26]. An overview of band structure calculations for TiO_2 is given in [7, 21]. Values of the band-gap depend on the crystallographic direction; they are given in Table 2.1. As a wide band-gap semiconductor

TiO₂ crystals have a high resistivity (in the order of $10^{15} \Omega\text{cm}$ [24]). When TiO₂ is reduced its n-type conductivity increases according to the extent of oxygen loss.

Kofstad [2, 27] has proposed that doubly-charged oxygen vacancies and interstitial titanium ions with three or four charges may occur as point defects in the rutile crystal. Depending on temperature, 0.007 - 0.08 eV have been reported for the ionization energies of titanium interstitials [28, 29]. Oxygen vacancies contribute to the electronic conduction as double donors with a shallow donor level (0 - 200 meV) and a deep donor level (600 - 750 meV) [24, 30, 31]. For anatase crystals the activation energy of carrier generation has been measured to be 4 meV [32].

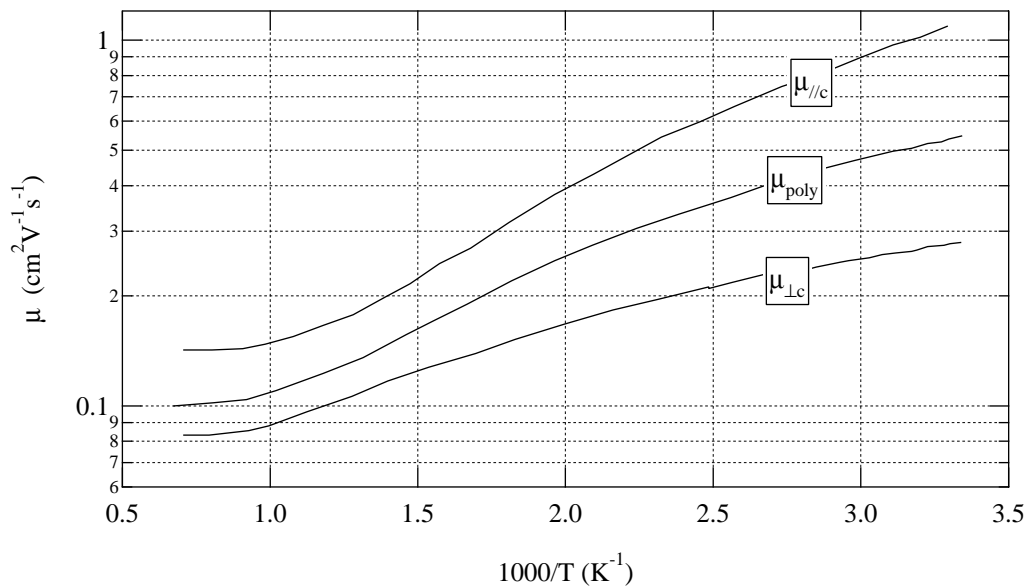


Figure 2.4: Mobility of rutile deduced from several publications by Poumellec et al. [42]. The mobility parallel ($\mu_{//c}$) and perpendicular ($\mu_{\perp c}$) to the c-axis as well as the mobility in polycrystalline rutile ($\mu_{poly} := \frac{2}{3}\mu_{\perp c} + \frac{1}{3}\mu_{//c}$, neglecting grain boundaries) are shown.

Whether titanium interstitials or oxygen vacancies are the dominant defects has not been definitively established [4, 24, 33]. Ardakani [24] gives many references showing experimental evidence for the existence of both phenomena. It is generally believed that, under weakly reducing conditions or low annealing temperatures (below 870 K in vacuum), oxygen vacancies are predominant. In the more reducing conditions and higher annealing temperatures (above 1'070 K in vacuum) titanium interstitials become more important [1, 24]. Blumenthal et al. [34] and Kofstad [2] calculated the enthalpy of formation of the oxygen vacancy (4.55 eV/vacancy) and of a triply charged interstitial titanium atom (9.11 - 9.24 eV per interstitial titanium). Since oxygen vacancies are more readily formed and the samples have never been heated to more than 250 °C¹ oxygen vacancies were probably the predominant point defects in the samples of the present study. However, in the sputtering process the incoming ions may have energies in excess of 10 eV [35] and the presence of frozen, high energy defects cannot completely be excluded. Complete analyses of defect concentrations in anatase have not been reported.

¹ Deposition at 250 °C, electrical measurements up to 250 °C.

The charge carrier mobility in rutile is low (see Figure 2.4 and Table 2.1), leading to a controversy over the nature of the carriers. Bogomolov et al. [36, 37] have proposed that charge carriers behave as small polarons, while Klinger disagreed [38]. A small polaron is an electron (or hole) self-trapped by the local lattice polarization which itself is generating [3]. As self-trapped localized states, small polarons proceed via hopping from site to site. In rutile a decreasing mobility for higher temperatures is attributed to phonon scattering. This suggests that the carriers are large polarons and not localized small polarons because the latter become more mobile at higher temperatures due to thermally activated hopping between the atoms [6]. However the mobility may decrease if the small polarons diffuse by tunneling [6]. Becker et al. have proposed a multiband conduction model for rutile [39]. In contrast to rutile, anatase shows a significantly higher Hall mobility, and a bandlike conduction behavior [7]. Therefore carriers are less likely to be small polarons in anatase than in rutile [7].

High concentrations of donors lead to the formation of impurity bands in anatase and rutile [7, 40]. When the impurity concentration exceeds a critical value, the impurity-band conduction can become metallic. The impurity-band conduction and the non-metal to metal transition have been experimentally observed and theoretically analyzed for oxide semiconductors [3]. A model of this transition has been developed by Mott [41]. A transition to metallic behavior has been observed in heavily reduced/doped anatase thin films [7], but not in similarly reduced rutile films [7, 28, 31, 40].

2.3 Optical properties

The dielectric functions of anatase and rutile single crystals have been extracted from literature (see below). In Figures 2.5 and 2.6 the dielectric functions are shown for the electric field parallel and perpendicular to the c-axis (marked with //c and \perp c, respectively). In the IR to VIS spectral range anatase is less anisotropic than rutile whereas in the band gap region anatase shows important anisotropy.

Depending on the degree of reduction of rutile TiO₂ the appearance of a blue color has been reported [31, 36, 43-45]. It has been found that this blue color arises from the visible tail of an infrared absorption band peaking at about 0.75 to 1.18 eV [36, 46]. In anatase the blue color has been observed, too [47, 48]. As in the case of rutile, it is caused by a wide absorption band with its maximum in the IR. In addition, a color center at 3 eV due to an oxygen vacancy has been identified giving rise to a yellow color [48].

The optical models in this study were based on literature data for crystalline TiO₂. For the energy range from 1.5 to 5 eV the anisotropic optical parameters of rutile have been taken from the work of Jellison et al. [49]. Values for the range below 1.5 eV can be found in Palik's handbook of optical constants [50]. The dielectric function for anatase has been published by Hosaka et al. [51] and for the spectral range below 2 eV by Washburn et al. [52]. Further information on the dielectric functions of anatase and rutile have been published by Jellison et al. [53 and references therein]. Jellison et al. also present the optical constants of a natural anatase crystal and of epitaxially stabilized anatase thin films. Differences in the absorption edge range between epitaxial and polycrystalline anatase and rutile thin films have been reported by Tanemura et al. [54].

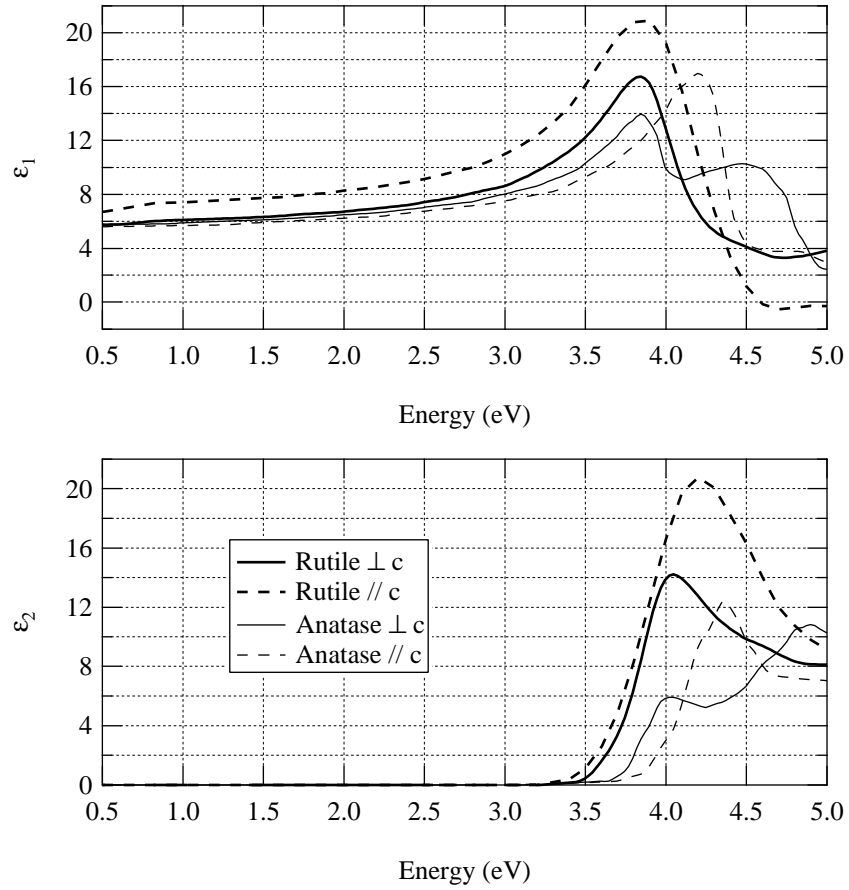


Figure 2.5: Real (ϵ_1) and imaginary parts (ϵ_2) of the dielectric function of rutile [49, 50] and anatase [51, 52]. For a detail of rutile at low energies see Figure 2.6.

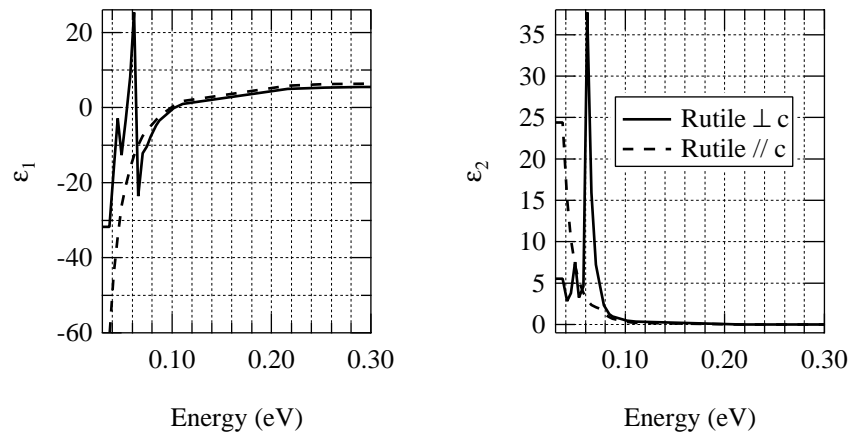


Figure 2.6: Real (ϵ_1) and imaginary parts (ϵ_2) of the dielectric function of rutile at low energies [50].

	Rutile		Anatase	
	// to c-axis	⊥ to c-axis	// to c-axis	⊥ to c-axis
Crystal structure	tetragonal		tetragonal	
Space group	P4 ₂ /mnm (136) [8] $c = 2.9587 \text{ \AA}$ [55] $a = 4.5937 \text{ \AA}$ [55]		I4 ₁ /amd (141) [8] $c = 9.5146 \text{ \AA}$ [17] $a = 3.7842 \text{ \AA}$ [17]	
Most stable surface	(110) [18]		(101) [47]	
Density	4.25 g/cm ³ [8]		3.89 g/cm ³ [8]	
Electrical properties at RT (undoped)	n-type semiconductor [22]		n-type semiconductor [32]	
Mott transition	not observed [40]		observed [7]	
Band gap at 10 K	3.051 eV [56, 57]	3.035 eV [56, 57]	3.46 eV [7]	3.42 eV [7]
Spectral dependence	E ^{1/2} [7]	E ^{3/2} [7]	Urbach [58]	Urbach [58]
Nature of gap	indirect [56, 57]	direct [56, 57]	indirect [7]	direct [7]
Mobility at RT in crystal	0.1 - 1 cm ² /Vs [1, 31] 0.01 cm ² /Vs (high impurity conc.) [1] $\mu_{//c} \approx (2 - 5) \cdot \mu_{\perp c}$ [31, 42] 0.6 - 1.5 cm ² /Vs [42]		15 cm ² /Vs [7, 32]	
Mobility at RT in polycrystalline thin film	0.1 cm ² /Vs [31, 59]		0.1 - 4 cm ² /Vs [7]	
Electron effective mass	9 - 13m _e [60] 10 - 30m _e [31] 12 - 32m _e [28]		~1m _e [7]	
Static dielectric const. ϵ_0 (MHz range)	173 [6, 61]	89 [6, 61]	48 [62]	31 [63]
High frequency limit dielectric constant ϵ_∞ ($\lambda = 600 \text{ nm}$)	8.35 [49]	6.76 [49]	6.25 [51]	6.50 [51]
Refractive index at ($\lambda = 600 \text{ nm}$)	2.89 [49]	2.60 [49]	2.50 [51]	2.55 [51]

Table 2.1: Comparison of the physical properties of rutile and anatase. For a list of further properties see [4].

References

1. Z.M. Jarzebski, *Oxide Semiconductors*. Permagon Press, (1973).
2. P. Kofstad, *Nonstoichiometry, diffusion, and electrical conductivity in binary metal oxides*. John Wiley & Sons, Inc., New York (1983).
3. P.A. Cox, *Transition Metal Oxides*. 1st ed., Clarendon press, Oxford (1992).
4. U. Diebold, *Surface Science Reports* **48** (2003), 53.
5. V.E. Henrich and P.A. Cox, *The surface science of metal oxides*. 1st ed., Cambridge University Press, Cambridge (1994).
6. N. Tsuda, K. Nasu, A. Fujimori, and K. Siratori, *Electronic conduction in oxides*. 2nd ed., Springer, Berlin, Heidelberg, New York (2001).
7. H. Tang, *Electronic properties of anatase TiO₂ investigated by electrical and optical measurements on single crystals and thin films*. Département de physique, Ecole polytechnique fédérale de Lausanne EPFL, Lausanne (1994).
8. *PDF-database*. JCPDS, International centre for diffraction data (ICDD), 1601 Park Lane, Swarthmore, PA 19081, USA.
9. J.F. Banfield, B.L. Bischoff, and M.A. Anderson, *Chemical Geology* **110** (1993), 211.
10. P.Y. Simons and F. Dacheville, *Acta Cryst.* **23** (1967), 334.
11. J. Tang and J. Endo, *J. Am. Ceram. Soc.* **76** (1993), 796.
12. J.S. Olsen, L. Gerward, and J.Z. Jiang, *Journal of Physics and Chemistry of Solids* **60** (1999), 229.
13. M. Lacroche, R. Brohan, R. Marchand, and M. Tournoux, *J. Solid State Chem.* **81** (1989), 78.
14. J. Akimoto, Y. Gotoh, Y. Oosawa, N. Nonose, T. Kumagai, and K. Aoki, *J. Solid State Chem.* **113** (1994), 27.
15. R. Marchand, R. Brohan, and M. Tournoux, *Mat. Res. Bull.* **15** (1980), 1129.
16. J. Haines and J.M. Leger, *Physica B* **192** (1993), 233.
17. M. Horn, C.F. Schwerdtfeger, and E.P. Meagher, *Zeitschrift für Kristallographie* **136** (1972), 273.
18. V.E. Henrich, *Rep. Prog. Phys.* **48** (1985), 1481.
19. L. Thien-Nga and A.T. Paxton, *Phys. Rev. B* **58** (1998), 13233.
20. R.W.G. Wyckoff, *Crystal Structures Handbook*. 2nd ed., Interscience Publishers, New York (1963).
21. G. Cangiani, *Ab-initio Study of the Properties of TiO₂ Rutile and Anatase Polytypes*. Faculté des sciences de base, Ecole polytechnique fédérale de Lausanne EPFL, Lausanne (2003).
22. D.C. Cronmeyer, *Phys. Rev.* **87** (1952), 876.
23. L. Kihlberg and I. Olovsson, *Acta Cryst. A* **53** (1997), 103.
24. H.K. Ardakani, *Thin Solid Films* **248** (1994), 234.
25. P.G. Wahlbeck and P.W. Gilles, *Journal of the American Ceramic Society* **49** (1966), 180.
26. M. Henzler and W. Göpel, *Oberflächenphysik des Festkörpers*. 2nd ed., B.G. Teubner, Stuttgart (1994).
27. P. Kofstad, *Journal of Less-Common Metals* **13** (1967), 635.
28. H.P.R. Frederikse, *J. Appl. Phys. suppl.* **32** (1961), 2211.
29. P. Knauth and H.L. Tuller, *J. Appl. Phys.* **85** (1999), 897.
30. K. Mizushima, M. Tanaka, A. Asai, S. Iida, and J.B. Goodenough, *J. Phys. Chem. Solids* **40** (1979), 1129.
31. R.G. Breckenridge and W.R. Hosler, *Phys. Rev.* **91** (1953), 793.
32. L. Forro, O. Chauvet, D. Emin, L. Zuppiroli, H. Berger, and F. Lévy, *J. Appl. Phys.* **75** (1994), 633.
33. N. Yu and J.W. Halley, *Phys. Rev. B* **51** (1995), 4768.
34. R.N. Blumenthal, J. Coburn, J. Baukus, and W.M. Hirthe, *Journal of Physics and Chemistry of Solids* **27** (1966), 643.
35. N. Martin, A.M.E. Santo, R. Sanjinés, and F. Lévy, *Surface and Coatings Technology* **138** (2001), 77.
36. V.N. Bogomolov, E.K. Kudinov, D.N. Mirlin, and Y.A. Firsov, *Soviet Physics -*

- Solid State **9** (1968), 1630.
37. V.N. Bogomolov, Y.A. Firsov, E.K. Kudinov, and D.N. Mirlin, *Physica Status Solidi* **35** (1969), 555.
 38. M.I. Klinger, *Phys. stat. sol.* **27** (1968), 479.
 39. J.H. Becker and W.R. Hosler, *Phys. Rev. A* **137** (1965), 1872.
 40. R.R. Hasiguti and E. Yagi, *Phys. Rev. B* **49** (1994), 7251.
 41. N.F. Mott, *Advan. Phys.* **16** (1967), 49.
 42. B. Pommellec, J.F. Marucco, and F. Lagnel, *Physica Status Solidi A* **89** (1985), 375.
 43. D.C. Cronemeyer, *Phys. Rev.* **113** (1959), 1222.
 44. M.E. Straumanis, T. Ejima, and W.J. James, *Acta Cryst.* **14** (1961), 493.
 45. R.D. Carnahan and J.O. Brittain, *Journal of the American Ceramic Society* **48** (1965), 365.
 46. D.C. Cronemeyer and M.A. Gilileo, *Phys. Rev.* **82** (1951), 975.
 47. N. Hosaka, T. Sekiya, M. Fujisawa, C. Satoko, and S. Kurita, *Journal of Electron Spectroscopy and Related Phenomena* **78** (1996), 75.
 48. T. Sekiya, K. Ichimura, M. Igarashi, and S. Kurita, *Journal of Physics and Chemistry of Solids* **61** (2000), 1237.
 49. G.E. Jellison, F.A. Modine, and L.A. Boatner, *Optics Letters* **22** (1997), 1808.
 50. E.D. Palik, *Handbook of Optical Constants of Solids*. Academic Press, Orlando (1985).
 51. N. Hosaka, T. Sekiya, C. Satoko, and S. Kurita, *Journal of the Physical Society of Japan* **66** (1997), 877.
 52. E.W. Washburn, *International Critical Tables of Numerical Data, Physics, Chemistry and Technology*. McGraw-Hill, (1930).
 53. G.E. Jellison, Jr., L.A. Boatner, J.D. Budai, B.S. Jeong, and D.P. Norton, *J. Appl. Phys.* **93** (2003), 9537.
 54. S. Tanemura, L. Miao, P. Jin, K. Kaneko, A. Terai, and N. Nabatova-Gabain, *Applied Surface Science* **212-213** (2003), 654.
 55. S.C. Abrahams and J.L. Bernstein, *J. Chem. Phys.* **55** (1971), 3206.
 56. J. Pascual, J. Camassel, and H. Mathieu, *Phys. Rev. B* **18** (1978), 5606.
 57. H. Mathieu, J. Pascual, and J. Camassel, *Phys. Rev. B* **18** (1978), 6920.
 58. H. Tang, F. Lévy, H. Berger, and P.E. Schmid, *Phys. Rev. B* **52** (1995), 7771.
 59. H. Tang, K. Prasad, R. Sanjinés, P.E. Schmid, and F. Lévy, *J. Appl. Phys.* **75** (1994), 2042.
 60. G.A. Acket and J. Volger, *Physica* **32** (1966), 1680.
 61. A. Eucken and W. Dannöhl, *Z. Elektrochem.* **40** (1934), 814.
 62. A. Eucken and A. Büchner, *Z. physikal. Chem. B* **27** (1935), 321.
 63. S. Roberts, *Phys. Rev.* **76** (1949), 1215.

Chapter 3 **Sample preparation**

In this chapter the techniques and basic parameters that have been used for the preparation of the samples are briefly discussed. Further details will be given at the beginning of the following chapters. The gas system and pumping unit, as well as the electrical circuit of the vacuum chamber that have been used for depositing the thin film samples are shown schematically in Figure 3.1 and Figure 3.2, respectively. Reviews of the sputtering technique can be found for instance in [1-3].

3.1 Reactive magnetron sputtering

Owing to its ability for the deposition of high quality films at high deposition rate and low process pressure, the magnetron sputtering technology has emerged as one of the most important deposition methods for thin film production [4]. In magnetron sputtering the atoms of a process gas are ionized to form a plasma between a target cathode (the magnetron) and a substrate electrode. The positively charged ions in the plasma are accelerated towards the target by the electric field between the electrodes. As a result, atoms are expelled from the target and deposited on the substrate. The magnetic field in front of the target causes an extended path length for plasma electrons, resulting in a higher collision rate and consequently in an increased density and confinement of the plasma in the vicinity of the target. The deposition process runs far from thermodynamic equilibrium and deposited films can be amorphous or polycrystalline [3]. With a metallic target the films deposited in this way will be purely metallic if only an inert gas as argon is used as process gas. In reactive sputtering adding gases as for instance nitrogen, oxygen, or water vapor will cause chemical reactions, and nitrides or oxides can be deposited. The chemical composition and the degree of crystallization in the films will depend on different deposition parameters. When the reactive gas flow is sufficient the target surface is 'poisoned' by nitrides or oxides resulting in a steep decrease of the deposition rate. This was the case when depositing titanium dioxide films close to stoichiometric composition (see Section 6.2).

3.1.1 Residual vacuum

The vacuum chamber had a volume of approximately 30 liters. A conventional pump unit consisting of a 500 ls^{-1} turbomolecular and a rotary vane primary pump established a base pressure of 10^{-7} mbar. During the deposition process the pumping rate was reduced by a throttle valve. The chamber walls were held at a constant temperature of $70 \text{ }^\circ\text{C}$. The quality of the residual vacuum was controlled by a mass spectrometer (Balzers QMG 125), and Pirani and Penning pressure gauges.

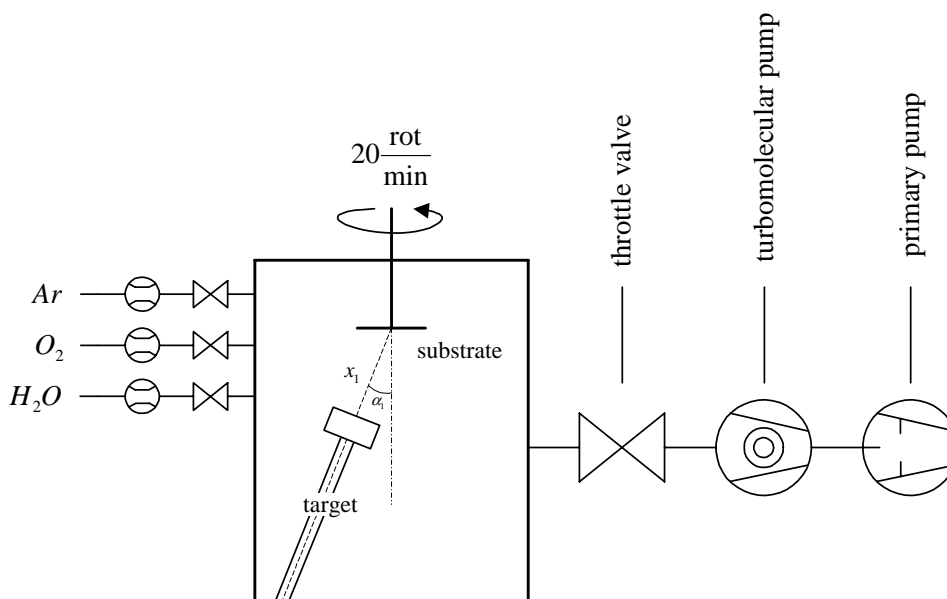


Figure 3.1: Schematic of the magnetron sputtering installation with the reactive gas inlet and pumping system. The target-substrate distance x_i was 9 cm, the deposition angle α_i was 21° .

3.1.2 Process gases

The gases used were Ar (99.999 %) as process gas, and either O_2 (99.998 %) or water vapor as reactive gas. Solubility of possible pollutants from ambient air in the distilled water was estimated according to Henry's law for ideal-dilute solutions [5]. For nitrogen as the most important pollutant it was $5 \cdot 10^{-4}$ mol/l, i.e. negligible. The process pressure was varied between 2 and $2.7 \cdot 10^{-3}$ mbar. The ratio of partial pressures between the reactive gas and argon was varied between 0 and 100 %. A hot cathode pressure gauge was used in this pressure range. Gas flow rates at the inlet were regulated by Brooks mass flow controllers. Due to oxidation of the target (poisoning effect), conventional reactive sputtering leads to an important drop of the deposition rate. Non-linear effects such as hysteresis loops of deposition parameters (e.g. target potential or reactive gas partial pressure) can occur. In order to prevent such instabilities, the process was run at a high pumping speed [6]. The pumping speed was adjusted to 160 ls^{-1} by the means of a throttle valve between the chamber and the pumping unit.

3.1.3 Magnetron targets

The magnetron consisted of a planar circular cathode backed by water-cooled permanent magnets and covered by disks of pure metal target material. The plates of target material had a diameter of 50 mm and a thickness of 3 mm. The target material used was titanium grade 2 (DIN 3.7035, less than 0.7 wt% impurities as N, C, H, Fe and O). The titanium plates were replaced after a lifetime of roughly 50 h. Before every deposition the target was conditioned at the wanted deposition parameters during at least 5 minutes. A shutter system in front of both target and substrate allowed protecting the substrates during the conditioning step.

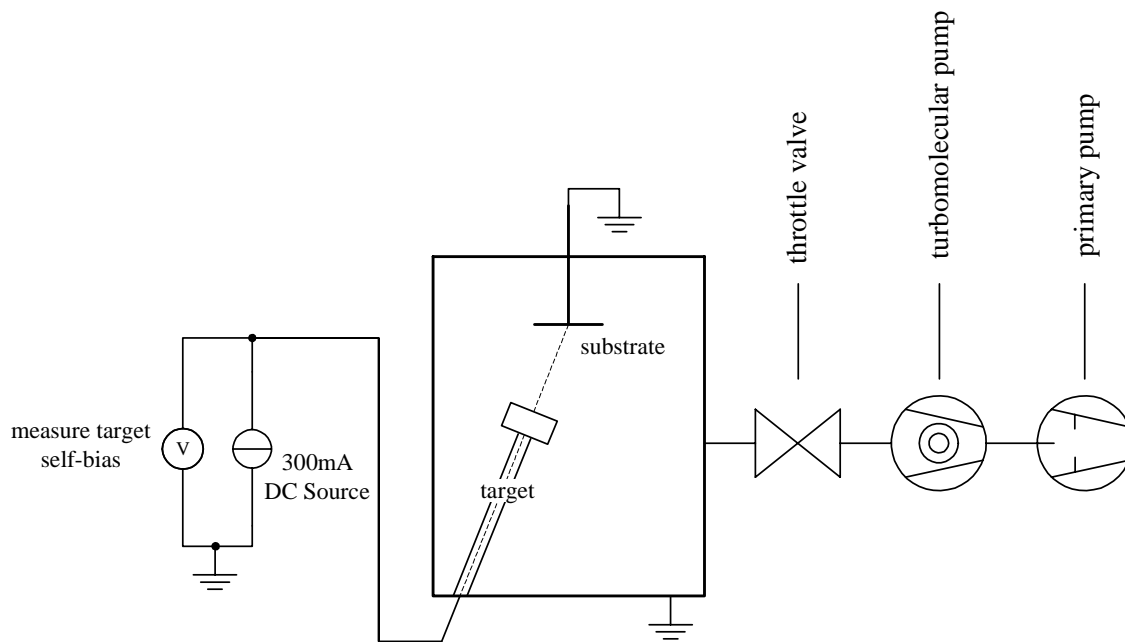


Figure 3.2: Schematic of the electronic circuit in the magnetron sputtering installation.

3.1.4 Power supply and electrical circuit

Undesirable arcing can occur during DC reactive sputtering of metal oxides from metallic targets. This is caused by charging of insulating, oxidized regions on the target surface, the so-called 'poisoned' areas. This was not the case for the TiO_2 deposited in the course of the present work. The oxidized, but substoichiometric, poisoned target surface was sufficiently electrically conducting. Accordingly, a DC power supply could be used (MDX-1K power source) providing a constant current of 300 mA. The target voltage varied around 400 V depending on the oxidation state of the target. The resulting power on the target ranged from 125 to 135 W corresponding to a power density of 6.4 to 6.9 Wcm^{-2} .

3.2 Substrate

The target-substrate distance was 9 cm and the deposition angle α_l was 21°. In order to improve the film homogeneity the substrate holder was rotated around its axis at a rate of 20 rotations per minute. Depositions were accomplished at a substrate temperature of 250 °C. The substrates were electrically grounded. Maximum substrate size was a disc of 50 mm diameter. Usually smaller substrate pieces of different materials were processed simultaneously. This allowed choosing a suitable substrate for every characterization technique. In an ideal case, all measurements should be made on the same kind of substrate to make sure that good correlations can be established between results. This is often not possible as will be discussed below.

	Silicon	Oxidized silicon	Glass
General properties		thermally oxidized in O ₂ atmosphere	microscope slide
Provider	ACM Applications Couches Minces	ACM Applications Couches Minces	Menzel-Gläser
Crystallinity	monocrystalline oriented (100)	amorphous SiO ₂ on Si monocrystalline oriented (111)	amorphous
Surface polishing	single or double-side polished	double-side polished	
Thickness	500 μm 2 nm native SiO ₂	500 μm Si with 100 nm SiO ₂	1 mm
Transparency	mid to near IR ²	mid to near IR ²	VIS and NIR ³
Conductivity	n-type 10 Sm ⁻¹	p-type 5 Sm ⁻¹	insulator < 10 ⁻¹¹ Sm ⁻¹

Table 3.1: Properties of the three types of substrates. The transmittance of the substrates is reported in Figure D.1.

Substrate materials included single- or double-side polished silicon (Si) wafers, thermally preoxidized silicon wafers, and glass microscope slides. The properties of these three kinds of substrates are summarized in Table 3.1. The respective cleaning and characterization techniques are presented in Table 3.2. The acronyms and corresponding techniques are explained in Chapter 4. The phase composition, grain size and preferential orientation were analyzed by x-ray diffraction measurements. These properties were found to be independent of the substrate. For optical transmission measurements silicon and glass substrates were complementary. 500 μm thick Si substrates are transparent in the infrared up to 1.1 eV, whereas glass is absorbing below 0.5 eV (Figure D.1 in the appendix). Electrical measurements were performed on insulating glass substrates. For chemical characterization techniques, in order to avoid an oxygen signal from the substrate, Si substrates were chosen. The silicon wafers were considered to be clean as provided and any further chemical treatment was avoided. Furthermore the number of necessary cleaving was reduced to the minimum. The microscope slides were cut to size and cleaned in an ultrasonic bath firstly for 10 minutes in acetone and then for 10 minutes in isopropanol.

3.3 Process monitoring

A first indication of the film thickness was given by a quartz crystal microbalance (QMB, Mextek thickness monitor) during deposition. Besides the gas flow controllers and pressure gauges a quadrupole mass spectrometer (Balzers QMG 422) was an important tool for monitoring the process. Instabilities during the deposition, impurities in the gas inlets and

² If double-side polished.

³ The glass substrate resembled borosilicate crown glass.

possibly leaks in the chamber could thus be detected. Monitoring the target voltage while the discharge was run at a constant current gave an indication of the oxidation state of the target [3, 7].

	Silicon	Oxidized silicon	Glass
Cleaning before deposition	none	none	ultrasonic bath: 10 min acetone, 10 min isopropanol
Structural	XRD, XRR SEM, TEM AFM, STM	XRD, XRR SEM, TEM AFM, STM	XRD
Chemical	EPMA, RBS, ERDA		
Electrical			van der Pauw
Optical spectroscopy	transm. in IR, reflection, ellipsometry	transm. in IR, reflection, ellipsometry	transm. NIR to VIS, reflection, ellipsometry

Table 3.2: Preparation and use of the different types of substrates. For explanations of the abbreviations see Chapter 4.

References

1. R.F. Bunshah, *Deposition technologies for films and coatings: developments and applications*. 1st ed., Noyes Publications, Park Ridge (1982).
2. D.L. Smith, *Thin-film deposition: principles and practice*. international ed., McGraw-Hill Inc., (1995).
3. M. Ohring, *Material science of thin films: Deposition and structure*. 2nd ed., Academic Press, San Diego (2002).
4. J.B. Webb, *Formation of thin semiconductor films by magnetron sputtering*, in *Thin films from free atoms and particles*, K.J. Klabunde (Editor). Academic Press, Orlando (1985).
5. P.W. Atkins, *Physical Chemistry*. 6th ed., Oxford University Press, Oxford (1998).
6. S. Kadlec, J. Musil, and J. Vyskocil, *Vacuum* **37** (1987), 729.
7. N. Martin, A.R. Bally, P. Hones, R. Sanjinés, and F. Lévy, *Thin Solid Films* **377-378** (2000), 550.

Chapter 4 **Characterization techniques**

In this section the basic principles of the characterization techniques used in the course of this work are briefly presented. Their resolution, detection limits and possible systematic and statistic errors are discussed. The techniques are grouped according to the sample properties they reveal: morphology, chemical composition, electrical and optical properties.

4.1 Morphology

4.1.1 Profilometry

During deposition the substrates were covered by a mask. With the profilometer the height of the step from the bare substrate to the top of the deposited film was scanned by a stylus. Two different profilometer instruments were used: the older alpha-step 500 and the more recent alpha-step P 15, both of KLA Tencor Corporation. 2 mm scans were performed with a force of 20 mN on the stylus. The former instrument did not do any averaging over a longer scan range. For better statistics at least 12 scans were performed on every sample. The latter instrument determined the step height from an average height calculated over a longer scan range, usually 200 μm . Therefore, with the model P15 only four scans were performed on every sample. Both approaches allowed thickness determination to about ± 5 nm. The film thickness measured by profilometry was used as a starting value in the fitting process during the analysis of the optical measurements (ellipsometry, reflectance and transmittance) as well as during the analysis of X-ray reflectivity. In addition, the thickness was directly related to the film density in the RBS and EPMA analyses.

4.1.2 X-ray diffraction

The crystalline phase composition, crystallite size and texture were analyzed by X-ray diffraction (XRD). Since the films were thin compared to the attenuation length of X-rays [1] a grazing incidence diffraction (GID) configuration was chosen.

4.1.2.1 Phase composition

Peak positions and intensities for many materials can be found in databases of powder diffraction files (PDF) such as that of the Joint Committee on Powder Diffraction Standards (JCPDS) [2, 3]. The most prominent peaks were the rutile (110) and the anatase (101) peaks

(at $d = 3.247 \text{ \AA}$ and 3.520 \AA , respectively). From the integrated peak surfaces I_R and I_A Spurr et al. [4] proposed

$$\text{Equation 4.1} \quad \frac{w_A}{w_R} = 0.79 \cdot \frac{I_A}{I_R}$$

to evaluate the ratio of the weight contents w_A of anatase and w_R of rutile. The value 0.79 has been determined experimentally. It corresponds to structure factor, multiplicity, polarization and Lorentz factor corrections [5, 6]. This approach is based on the assumption that texture effects are absent because it considers one peak only for each phase.

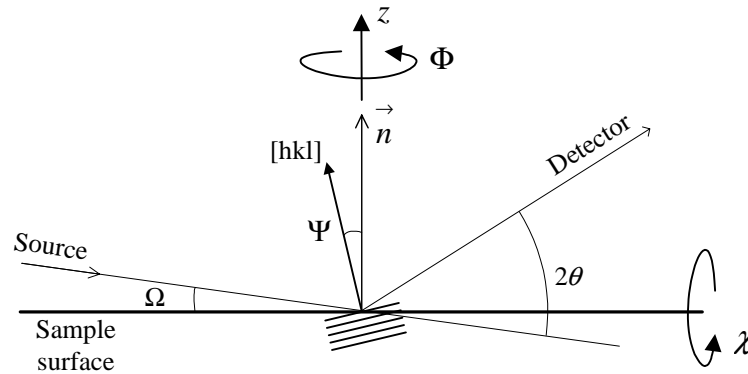


Figure 4.1: The sample surface with incident and diffracted/reflected X-ray beam. The incident and diffracted beams define the scattering plane. The vector $[hkl]$ lies in between the two and is perpendicular to the diffracting family of plane (hkl) . Ω is the incidence angle on the sample surface and 2θ marks the angle between incident and diffracted beams. Φ marks the rotation around the sample normal n , X is the rotation around the intersection between the scattering plane and the sample surface. The translation along n is called z -axis.

The crystallinity of the samples was obtained from the ratio of the total integrated intensities scattered by the crystalline and the amorphous fractions [7]. The incoherent background level was measured on a bare substrate. It was subtracted before the intensity due to the amorphous phase was determined.

4.1.2.2 Grain size

The shape of each Bragg peak results from the combined effects of the crystallite size, internal strain, point defects and of the instrumental broadening. Assuming that the influence due to strain and point defects is weak the grain size d_{grain} can be calculated according to the Scherrer formula (e.g. [5])

$$\text{Equation 4.2} \quad d_{grain} = \frac{0.9 \cdot \lambda}{B_{grain} \cdot \cos \Theta}$$

where B_{grain} is obtained from the measured peak width B_{meas} in the diffraction pattern:

$$\text{Equation 4.3} \quad B_{meas}^2 = B_{instr}^2 + B_{grain}^2$$

The instrumental broadening B_{instr} was determined by a measurement on Y_2O_3 powder with sufficiently large grains.

4.1.3 X-ray reflectivity

X-ray reflectivity (XRR) is based on the fact that the refractive index of a solid is slightly smaller than unity in the energy range of X-rays. At small enough incidence angles the X-rays are totally reflected from the sample surface. Above a critical angle α_c the X-ray beam can penetrate into the sample and undergo multiple reflections between the different interfaces present in the thin film. The amplitude and position of the interference fringes depend on the thickness and electron density of the thin film material. In addition, the surface and interface roughnesses also affect the shape of the reflectance curve. The basic principles of the XRR technique are explained in Appendix E.

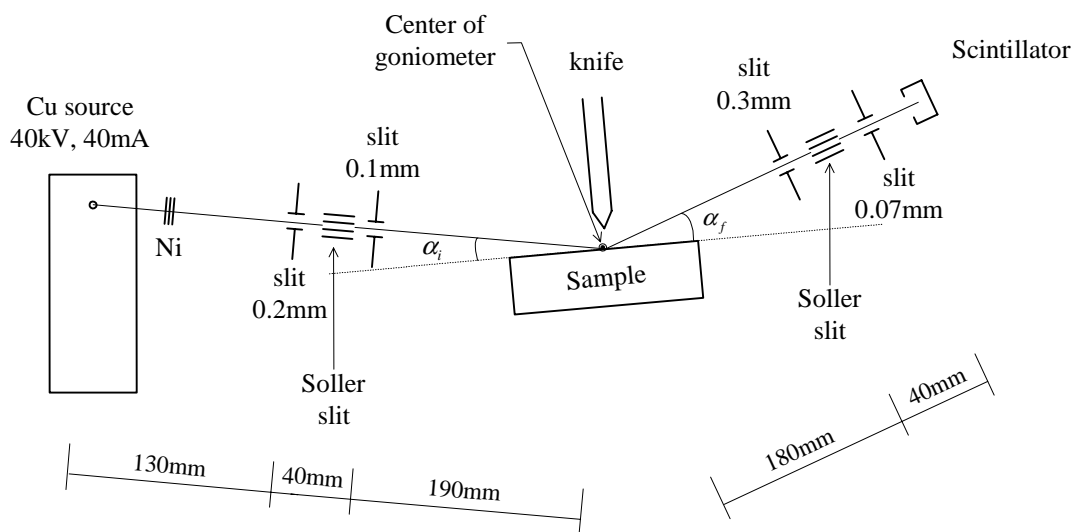


Figure 4.2: Schematic of the X-ray diffractometer for the X-ray reflectivity measurements.

For the XRR measurement a Seifert 3000, 4-axes goniometer was employed with a Cu X-ray source⁴. The source had a 0.4 mm × 12 mm line focus and was run at 40 kV and 40 mA. A combination of Ni-filter and slit system maintained adequate intensity. See Figure 4.2 for the details on the configuration. This configuration allowed for a high intensity and thus for a wide angular range in spite of a steep decrease in reflected intensity for larger angles (see for instance Figure 6.8 on p. 48). The beam divergence and the detector acceptance were of the order of 0.035°. A knife edge at typically 20 to 50 μm from the sample surface allowed reducing the irradiated sample surface and increasing the angular resolution. Automatically changing Cu lamellae acted as absorbers in front of the detector. They allowed measuring the whole intensity range from about 10⁶ down to 1 cps without interrupting the measurement. The integration time per step was adapted to the intensities in the different sections of the scan. Up to $2\theta = 1^\circ$ it was usually not more than one second, whereas for high angles it was increased up to 100 seconds. The step size was 0.0025° in Ω (see Figure 4.1). The upper limit for 2θ was about 5°. This resulted in a duration of typically 10 hours for one measurement.

⁴ Cu K_{α1}: 1.5406 Å, 8049 eV; Cu K_{α2}: 1.5443 Å, 8027 eV.

4.1.4 Atomic force microscopy

The atomic force microscopy (AFM) allows determining the surface topography of a sample with a resolution in the nanometer range. This is a scanning probe microscopy technique where a silicon cantilever with a tip acts as a probe [8]. A piezo crystal scanner supports the cantilever and allows the nanometric positioning of the tip. While scanning in the non-contact mode, the cantilever is oscillating close to its resonance frequency (in the order of 100 kHz). Van der Waals and Coulomb forces act on the cantilever when it gets in close vicinity of the surface. Any change in the force between the probe and the sample surface is observed as a change of the resonance frequency. This signal is fed into a feedback loop moving the tip closer or further away from the sample in order to maintain a constant detuning. The corresponding height information is registered as a function of the x - and y -coordinates of the scanner giving a topographical map [8].

For this study a Topo Metrix AFM with a silicon tip was used. The lateral resolution was limited to about 1 nm. The instrument was operated in air. A measure of the surface roughness was obtained from $500 \text{ nm} \times 500 \text{ nm}$ images with 300×300 pixel resolution. The surface roughness was evaluated according to

Equation 4.4

$$t_{RMS} = \sqrt{\frac{1}{N} \cdot \sum_{i=1}^N (z_i - \langle z \rangle)^2}$$

where t_{RMS} is the root-mean-square roughness, $\langle z \rangle$ the average height and z_i the height at point i . An estimate of the grain size was obtained from profiles selected across the AFM topography maps.

4.1.5 Scanning tunneling microscopy

In the case of the scanning tunneling microscope (STM) the scanning tip is electrically conducting. When a bias voltage is applied (typically between 1 mV and 4 V) to the tip and when the tip is moved close enough to the surface of a conducting sample a tunneling current of typically 0.1 to 10 nA can be observed. In the constant current mode the tunneling current acts as the input signal for the feedback loop. In order to obtain a constant current the tip to surface distance is changed. As for the AFM this gives the topography information as a function of position [8, 9]. An Omicron STM-1 microscope with a tungsten tip and a lateral resolution of about 1 Å in the constant current mode was used.

4.1.6 Scanning electron microscopy

For the measurements in this study a Philips XL 30 FEG was used with a resolution better than 4 nm. Because of charging effects in poorly conducting films the acceleration voltage was varied between 10 kV and 25 kV. Details on scanning electron microscopy are discussed in [10-12].

4.1.7 Transmission electron microscopy

Transmission electron microscopy (TEM) was used for local nanostructure investigation on the cross section of the films. An introduction and detailed descriptions of the electron microscopy techniques can be found in [12-14]. For this thesis TEM observations were done at the Centre Interdisciplinaire de Microscopie Electronique (CIME) at the EPFL on a Hitachi HF-2000 microscope. Specimens on Si (100) substrates were prepared by mechanical polishing down to a thickness of about 30 μm . Further reduction of the thickness of a small region to roughly 20 nm was achieved by ion milling during 90 min in a Gatan PIPS at 8° incidence angle with Ar^+ ions at 4 kV. Contamination by hydrocarbons was reduced by plasma-etch during 45 min at 100 W in O_2 plasma (0.2 mbar). The preparation procedure is very delicate. A problem was the different sputtering rates of TiO_2 , Ti and of the substrate. Furthermore, artifacts induced by ion bombardment could not be excluded. Therefore, electron microscopy in transmission on cleaved edges was a good alternative.

4.2 Chemical composition

4.2.1 Electron probe microanalysis

Electron probe microanalysis (EPMA) measurements were performed at the Institute of Mineralogy at the University of Lausanne on a CAMECA SX 50 equipment. In this technique the sample is bombarded with electrons of a specific energy (about 8 through 17 keV, 20 nA). In the film and substrate the electrons are scattered and finally absorbed. Excited atoms loose energy by emitting energy in form of X-ray radiation characteristic for every element (the K- and L-edges). In wavelength dispersive spectrometry (WDS) the wavelength and intensity distribution of the emitted X-rays is analyzed by a monochromator crystal at the respective Bragg diffraction angle [15].

The intensity ratio of the characteristic X-rays emitted from the sample is measured. For quantitative analysis the sample signal is compared to the signal of a standard of known chemical composition. Correction models take the scattering of the electrons, the absorption of the emitted X-ray on its way to the surface, and possible fluorescence of other elements into account. For measurements on bulk materials the error in chemical composition can be as low as 1 at%, depending on the quality of the standard [16].

The minimum penetration depth of the beam is about 500 nm. In the case of 100 to 500 nm thin films the observed volume contained a part of the substrate. This could be corrected for in the STRATAgem software [17] for thin film analysis. It is based on a model proposed by Pouchou et al. [16, 18]. With this software the chemical composition and the mass per unit surface (mg/cm^2) of a film on a substrate can simultaneously be determined by an iterative procedure. Knowing the film thickness the film density could be determined.

4.2.2 Rutherford backscattering analysis and Elastic recoil detection analysis

Rutherford backscattering analyses (RBS) were performed at the Centre d'Analyses par Faisceau Ionique (CAFI) at the École d'Ingénieurs (EICN) in Le Locle. In this technique the samples were bombarded with 2 MeV He⁺ ions at two different incidence angles. The ions have enough energy to penetrate the electron cloud of the target atoms and scatter elastically off the target nuclei (Rutherford scattering). The mass of the target atom can be determined by measuring the energy transfer. Furthermore, the scattering cross section enables a quantitative analysis of the atomic composition. The ions traveling through the sample lose energy mostly by Coulomb interaction with the electrons. This allows obtaining depth information in the form of a chemical depth profile. RBS cannot usefully detect atoms lighter than the projectile. In order to be more sensitive for light elements in this study a proton beam was used, too. A good overview and main properties of this technique are given in [19].

Elastic recoil detection analysis (ERDA) is complementary to RBS and was accomplished in parallel with the RBS measurements. Here the forward scattered target atom, rather than the scattered projectile, is detected. In contrast to RBS, atoms lighter than the projectile can be detected. For instance H or D depth profiling can be achieved with the help of He⁺ ions. The ion beam enters the sample at grazing angle and the target atoms are scattered preferentially in the forward direction. A thin filter foil can separate the scattered He⁺ ions from the lighter recoil atoms. This technique is explained in detail in e.g. [20].

One of the advantages of these techniques is that absolute chemical composition can be obtained without the need of standard samples. The chemical composition determined by RBS and ERDA is precise within 0.5 at%. This can be translated in $\Delta x = \pm 0.02$ with x close to 2 in TiO_x. The depth resolution was about 5 nm. RBS and ERDA measurements were performed on non-preoxidized Si substrates. Both techniques are non-destructive and the samples could be used for further investigation.

The thickness N_t in units of atoms per square centimeter was obtained from the analysis. Knowing the thickness t of the sample it was possible to determine the density ρ_{film} (or vice versa) [21].

Equation 4.5

$$\rho_{film} = \frac{N_t \cdot \langle M_Z \rangle}{t \cdot N_A}$$

where ρ_{film} is the mass density in g/cm³, N_t is the areal density in atoms/cm², $\langle M_Z \rangle = \sum f_Z M_Z$ the average atomic mass in g/mol (with f_Z and M_Z the atomic fraction and the atomic weight of element Z, respectively) and N_A is Avogadro's constant.

4.2.3 Electron energy loss spectrometry

Electron energy loss spectrometry (EELS) involves the analysis of the energy distribution of the inelastically scattered electrons in the transmitted electron beam in a TEM instrument. The energy loss spectrum reveals which ionization event occurred in the specimen and therefore which element is present in the specimen. Quantification of EELS spectra is challenging. It can be divided into three steps. Firstly the background is removed from beneath the ionization edge, secondly the area within the edge is integrated and finally the composition is determined from the ratio of the integrated intensities. A parallel electron energy loss spectrometer (666-PEELS) mounted on the Hitachi HF-2000 microscope was used with a lateral resolution

of about 1.5 nm and a resolution in energy of less than 1 eV. For quantification the K-edge of O and the L_{2,3}-edges of Ti were analyzed. Further information about this technique can be found in [12, 13, 22].

4.3 Electrical properties

Most samples discussed in this thesis were conducting enough (i.e. above about 10⁻¹ Sm⁻¹) to be measured in a coplanar geometry. In the 'van der Pauw' configuration [23-25] the contacts are located across the edges of the sample. The shape of the sample is nearly arbitrary, provided that it is a sheet of constant thickness. The material properties must be uniaxial, with the axis perpendicular to the sheet. Quadrangular samples with the contacts halfway in between the corners were used. This setup is shown in Figure 4.3. Contacts are numbered 1 through 4 sequentially along the edge of the sample. The current is applied on two contacts while the voltage is measured on the two others. The resistance $R_{i,i+1}$ is defined as

$$\text{Equation 4.6} \quad R_{i,i+1} := \frac{U_{i+2,i+3}}{I_{i,i+1}}$$

The electrical conductivity $\sigma_{DC} = 1/\rho_{DC}$ of a sample with thickness t is determined from

$$\text{Equation 4.7} \quad \rho_{DC} = \frac{\pi \cdot t}{2 \cdot \ln 2} \cdot (R_{12} + R_{23}) \cdot f \left(\frac{R_{12}}{R_{23}} \right)$$

where f represents a geometrical correction. The function f satisfies the relation [24]

$$\text{Equation 4.8} \quad \left(\frac{R_{12}}{R_{23}} - 1 \right) \cdot \left(\frac{R_{12}}{R_{23}} + 1 \right)^{-1} = \frac{f}{\ln 2} \cdot \operatorname{arcosh} \left(\frac{1}{2} \cdot \exp \left(\frac{\ln 2}{f} \right) \right)$$

For the present study the samples were nearly square shaped and thus R_{12} and R_{23} were almost equal and f was close unity.

The evolution of the conductivity with temperature depends on the conduction mechanism. With increasing temperature phonon scattering phenomena reduces the electrical conductivity as for instance in metals. Alternatively, the conductivity can be thermally activated as it usually occurs in semiconductors. Therefore, conductivity measurements at several temperatures can give insight into the properties of charge carriers. The measurements were performed between room temperature and 250 °C. The samples were heated at a rate of 5° per minute in ambient air. Several cycles were repeated in order to detect sample degradation. A thermocouple placed on a separate piece of substrate on the heating plate recorded the temperature (see Figure 4.3). The voltage was measured while using a constant current in the order of 10⁻² to 10⁻⁸ A.

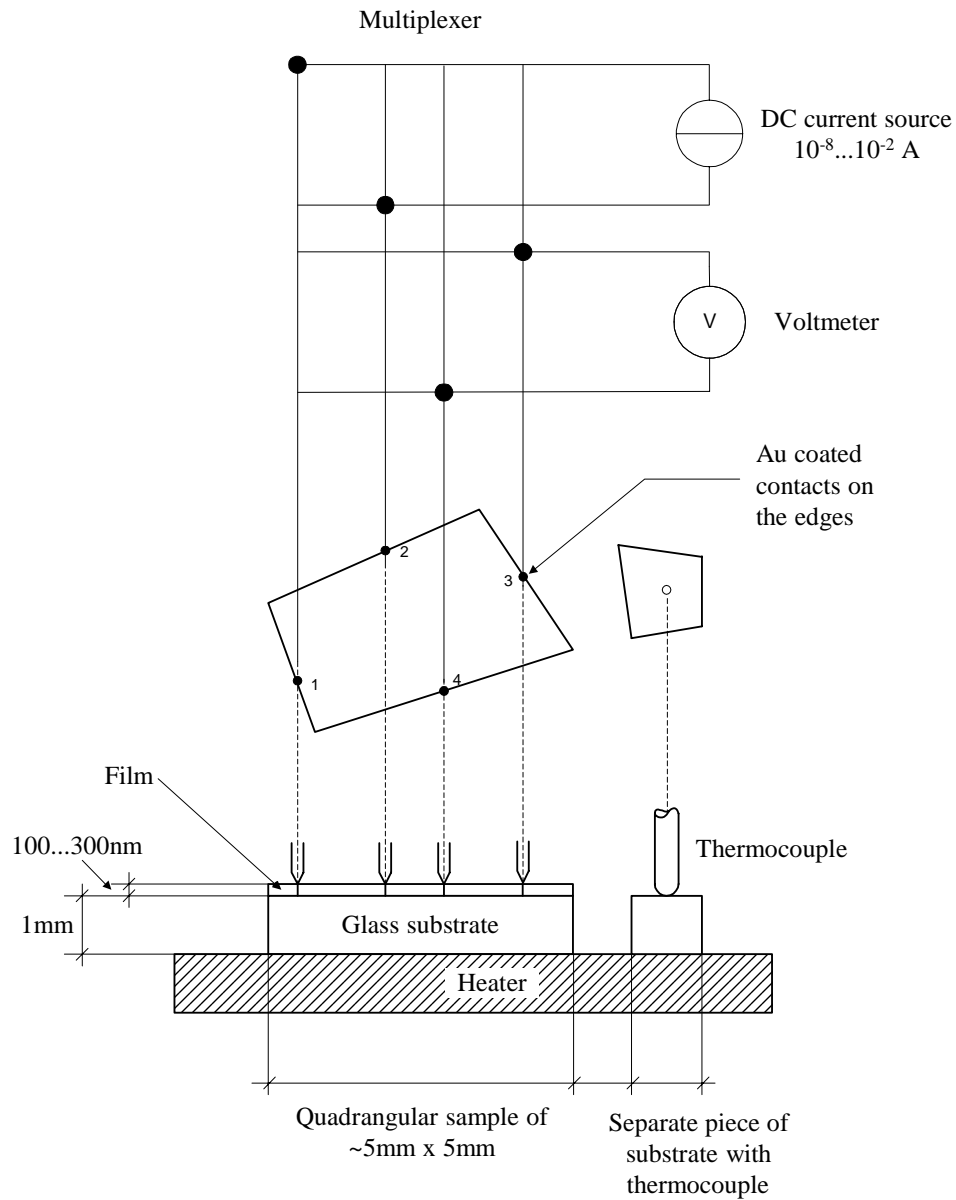


Figure 4.3: Setup for the electrical measurements in the van der Pauw configuration. As an example the multiplexer is shown in the configuration for the measurement of R_{12} .

4.4 Optical properties

With respect to the electronic properties of the film, the optical properties in the infrared, visible and ultra-violet ranges are a rich source of information. In the present section the measuring techniques are presented. The methods used for the analysis are discussed thoroughly in Chapter 5 and Appendices A to D. An overview of the experimental setups and corresponding spectral ranges is given in Table 4.1.

4.4.1 Ellipsometry

Reflection ellipsometry measures the ratio ρ of the complex Fresnel reflection coefficients r_p and r_s for the p- and s-polarizations (see Equation A.13), respectively,

$$\text{Equation 4.9} \quad \rho = \frac{r_p}{r_s}$$

This is often written as

$$\text{Equation 4.10} \quad \rho = \tan \Psi \cdot \exp(i\Delta)$$

where Ψ and Δ are the ellipsometric angles. Ψ represents the amplitude ratio and Δ the phase difference of the two eigenpolarizations after reflection:

$$\text{Equation 4.11} \quad \tan \Psi = \frac{|r_p|}{|r_s|}$$

$$\text{Equation 4.12} \quad \Delta = \delta_{rp} - \delta_{rs}$$

In Equations 4.14 and 4.15 the amplitude and the phase of the complex Fresnel reflection coefficients have been separated as

$$\text{Equation 4.13} \quad r_p = |r_p| \cdot \exp(i\delta_{rp}) \quad \text{and} \quad r_s = |r_s| \cdot \exp(i\delta_{rs})$$

Most of the measurements were accomplished on our ellipsometer (UVISEL, Jobin-Yvon) at EPFL. The accessible spectral range was from 1.5 through 5.0 eV. The measuring angle was chosen to be 70 degrees, because this is close to the Brewster angle of many materials, and therefore maximum sensitivity can be obtained [26]. The rest of the measurements were done on an ellipsometer (Jobin-Yvon) at the EICN with a larger spectral range from 0.75 to 5 eV. Both instruments were configured as phase-modulated ellipsometers with a Xenon lamp, a polarizer and phase modulator on the primary side and an analyzer and monochromator on the secondary side.

4.4.2 Transmission

Spectroscopic transmission measurements were carried out at normal incidence with a Cary 500 UV-VIS-NIR grating-spectrophotometer. The instrumental range was 175 nm to 3'300 nm (0.38 eV - 7 eV). As substrates double-side polished silicon and glass were used. The transmittance of the substrates is shown in Figure D.1. The transmission configuration is

the most sensitive to detect small absorption bands, such as those related to impurity levels and defects.

4.4.3 Reflection

Reflection measurements at an incidence angle of 30° were performed on the same Cary spectrophotometer. Glen-Taylor polarizing prisms (250 to 3'000 nm) in the incident beam allowed selecting either s- or p-polarization. On the secondary side a depolarizer (two crystalline quartz wedges with 45° between the two crystal axes) was inserted to avoid problems due to detector sensitivity on polarization. The reflectance R_{sample} was measured by comparison with reference gold or aluminum mirrors

Equation 4.14

$$R_{sample} = \frac{R_{sample-meas}}{R_{ref-meas}} \cdot R_{ref}$$

where $R_{sample-meas}$ and $R_{ref-meas}$ are the measured reflectances and R_{ref} is the reflectance of a perfect gold or aluminum mirror [27, 28] for the corresponding angle and polarization.

4.4.4 Infrared transmission

A Nexus Fourier-transform infrared spectrometer was used to measure the transmission at normal incidence in the range from 400 through 4'000 cm^{-1} (photon energies of 0.05 to 0.5 eV). The instrument casing was constantly flooded with dry N_2 gas. From roughly 0.2 to 1.1 eV double-side polished Si substrates are suitably transparent (about 60 % transmittance for 500 μm thick wafers, see Figure D.1).

Instrument	Configuration	Energy (eV)	Wavelength (nm)
Ellipsometer at EPFL at EICN	Reflection at 70°	1.5 - 5	250 - 830
	Reflection at 70°	0.75 - 5	250 - 1'650
Cary 500	Transmission at 0°	0.38 - 7	175 - 3'300
	Reflection at 7°	0.38 - 7	175 - 3'300
	Reflection at 30°	0.41 - 5	250 - 3'000
Nexus FTIR	Transmission at 0°	0.05 - 0.5	2'480 - 24'800

Table 4.1: Summary of the spectrophotometry and ellipsometry techniques and the spectral ranges of the instruments.

References

1. B.L. Henke, E.M. Gullikson, and J.C. Davis, *Atomic Data and Nuclear Data Tables* **54** (1993), 181.
2. *PDF-database*. JCPDS, International centre for diffraction data (ICDD), 1601 Park Lane, Swarthmore, PA 19081, USA.
3. D.K. Smith and R. Jenkins, *The Rigaku Journal* **6** (1989), 3.
4. R.A. Spurr and H. Myers, *Analytical Chemistry* **29** (1957), 760.
5. B.D. Cullity, *Elements of X-ray diffraction*. 2nd ed., Addison-Wesley Publishing Company, Inc., (1978).
6. L.S. Zevin and G. Kimmel, *Quantitative X-ray diffractometry*. 1st ed., Springer, Berlin (1995).
7. *Percent Crystallinity Determination by X-ray diffraction*, in *Kratos Analytical Applications Note*. Kratos Analytical, New York (September 1999).
8. R.J. Colton, A. Engel, J.E. Frommer, H.E. Gaub, A.A. Gewirth, R. Guckenberger, J. Rabe, W.M. Heckl, and B. Parkinson, *Procedures in Scanning Probe Microscopies*. 1st ed., John Wiley & Sons, Chichester (1998).
9. H.-J. Güntherodt and R. Wiesendanger, *Scanning Tunneling Microscopy I*. 2nd ed., Springer Verlag, Berlin (1994).
10. J.D. Verhoeven, *Scanning Electron Microscopy*, in *Materials Characterization*, R.E. Whan (Editor). America Society for Metals, (1986).
11. L. Reimer, *Scanning Electron Microscopy: Physics of Image Formation and Microanalysis*. 2nd ed., Springer-Verlag, Berlin (1998).
12. P.J. Goodhew, J. Humphreys, and R. Beanland, *Electron Microscopy and Analysis*. Taylor & Francis, London (2001).
13. A.D. Romig Jr., *Analytical Transmission Electron Microscopy*, in *Materials Characterization*, R.E. Whan (Editor). America Society for Metals, (1986).
14. L. Reimer, *Transmission Electron Microscopy: Physics of Image Formation and Microanalysis*. 2nd ed., Springer-Verlag, Berlin (1997).
15. K.F.J. Heinrich and D.E. Newbury, *Electron probe X-ray microanalysis*, in *Materials Characterization*, R.E. Whan (Editor). America Society for Metals, (1986).
16. J.L. Pouchou and F. Pichoir, *Electron Probe Quantitation*, in *Electron Probe Quantitation*, K.F.J. Heinrich and D.E. Newbury (Editors). Plenum Press, New York (1991).
17. J.L. Pouchou, *STRATAGEM*. 2002, SAMx, saint André de la Roche, France: Châtillon.
18. J.L. Pouchou, F. Pichoir, and D. Boivin, *Microbeam Analysis*. San Francisco Press, (1990).
19. W.-K. Chu, *Rutherford Backscattering Spectrometry*, in *Materials Characterization*, E.R. Whan (Editor). America Society for Metals, (1986).
20. W.A. Lanford, *Nuclear Instruments and Methods in Physics Research B* **66** (1992), 65.
21. M. Laube, F. Rauch, C. Ottermann, O. Anderson, and K. Bange, *Nuclear Instruments and Methods in Physics Research B* **113** (1996), 288.
22. D.B. Williams and C.B. Carter, *Spectrometry IV: The energy loss spectrum*, in *Transmission electron microscopy*. Plenum publishing corporation, (1996).
23. L.J. van der Pauw, *Philips Research Reports* **13** (1958), 1.
24. L.J. van der Pauw, *Philips Technical Review* **20** (1958/1959), 220.
25. W.R. Runyan, *Resistivity and carrier-concentration measurements*, in *Semiconductor measurements and instrumentation*, T.G. Hicks and L. Strong (Editors). Tosho Printing, Tokyo (1975).
26. H.G. Tompkins and W.A. McGahan, *Spectroscopic ellipsometry and reflectometry, A users guide*. 1st ed., John Wiley & Sons, Inc., New York (1999).
27. E.D. Palik, *Handbook of Optical Constants of Solids*. Academic Press, Orlando (1985).
28. E.D. Palik, *Handbook of Optical Constants of Solids II*. Academic Press, Orlando (1991).

Chapter 5 **Analyzing the optical properties of a thin film**

In the optical range the dielectric function $\varepsilon(\hbar\omega)$, where $\hbar\omega$ is the photon energy, of a solid reveals details about its low energy electronic excitations. In turn one obtains information on the occupied and empty electronic states and on the properties of charge carriers. Spectrophotometry and ellipsometry have been important tools in the present study. The different configurations and spectral ranges that have been used are presented in Section 4.4 and Table 4.1. In this chapter it is briefly explained how the dielectric function of a film under investigation is obtained from the measured spectra. Details on the calculations and formulae are given in the Appendices. The basic concepts required to describe the optical properties of solids are discussed for instance by Wooten [1] and Sadao [2]. Many experimental details are given in the book of Tompkins and McGahan [3]. The interaction of polarized light with stratified structures is described by Azzam and Bashara [4] and Jellison [5].

The solid material under study in the present work is a thin film deposited on a substrate. The dielectric function of the thin film material can be accessed through the analysis of the optical response (transmittance, reflectance, ellipsometry) of the sample, i.e. the thin film on top of its substrate. This corresponds to a stack of layers. Each layer is characterized by a dielectric function $\varepsilon(\hbar\omega)$, assuming isotropic properties.

The optical response of a sample can readily be calculated if the structure of the stack and the properties of all layers are known. The reverse problem in which spectrophotometrically measured spectra are to be used to determine unknown optical properties (including thicknesses) of a stratified structure is only possible in few particular cases, as for instance a semi-infinite sample. For more complicated structures, an optimization process is needed to find a model which reproduces the measured optical response.

Abelès [6], and Hayfield and White [7] proposed a matrix formalism (see Appendix A) which describes the optical properties of stacks of layers. The stack consists of homogeneous layers with parallel interfaces. Such a stack has an optical axis perpendicular to the plane and is isotropic in all directions within the sample plane. The matrix formalism must account for such uniaxial behavior (Appendix A).

The layer interfaces are not perfect planes in real samples. The effects of interface and surface roughness can be approximated by introducing interface roughness layers into the stack. The Bruggeman effective medium approximation (see Appendix B) has been found to be valuable to model such roughness [8, 9]. Furthermore, the thin film is often not homogeneous at a scale smaller than the wavelength. Common sources of inhomogeneity are porosity, and/or the coexistence of several phases. Such a phase mixture may present further difficulties if any of the phases present is not isotropic and if furthermore the orientation of its grains presents a texture. Such inhomogeneity effects can be approximated by effective medium models (see Appendix B).

In real samples, certain interface planes are not parallel enough to give rise to interference patterns. This can be intentional, for instance on glass substrates (microscope slides). Proper treatment of such slabs must be provided. The way how the different substrates have been accounted for is described in Appendix D.

The models used in the present study address all the requirements mentioned above. They have been implemented in Matlab routines. Restrictions on the large number of parameters were obtained from characterization techniques presented in Chapter 4. Estimates of the surface roughness t_{RMS} were obtained by atomic force microscopy. Maximum values of 6 nm for 400 nm thick films have been observed. The surface roughness was accounted for in the models by a roughness layer with thickness t_{RMS} . The effective dielectric function of the roughness layer was modelled by a Bruggeman effective medium approximation assuming a filling factor of 0.5 for both air and the film material (see Appendix B). X-ray diffraction measurements gave indications about preferential orientation of the anisotropic rutile and anatase crystallites. The volume fractions f_A of anatase and f_R of rutile were taken into account in the effective medium approximations. They were calculated from the corresponding weight fractions (determined by XRD) according to

$$\text{Equation 5.1} \quad \frac{f_A}{f_R} = \frac{\rho_R}{\rho_A} \cdot \frac{w_A}{w_R}$$

where ρ_A and ρ_R are the densities of anatase and rutile, respectively. In addition voids were included in the effective medium approximations. When the amorphous content was small, an estimate of the void content f_{vac} was obtained from

$$\text{Equation 5.2} \quad f_{vac} = 1 - \frac{\rho_{film}}{\langle \rho \rangle}$$

where ρ_{film} is the density of the film measured by RBS or XRR and $\langle \rho \rangle = f_A \cdot \rho_A + (1-f_A) \cdot \rho_R$ is the weighted mean of the crystalline densities of anatase and rutile.

Reference data for the dielectric functions of anatase and rutile have been extracted from the literature. They are presented in Chapter 2. The optical properties of amorphous TiO_2 are not known [10]. They can vary considerably with deposition conditions [5]. In recent publications it has sometimes been assumed that amorphous TiO_2 exhibits anatase properties. The refractive index of amorphous TiO_2 is lower than that of single crystals [10-12]. An apparently high concentration of voids as deduced from the index of refraction may actually indicate the presence of amorphous material.

To account for effects due to mobile charge carriers the dielectric functions for crystalline anatase and rutile will be modified in the subsequent chapters. This will be achieved by introducing additional Lorentzian and/or Drude terms (Appendix C). In Chapters 7 and 8 metallic inclusions of either titanium or titanium monoxide are considered. The dielectric function for titanium monoxide was obtained by ellipsometry in the spectral range from 1.5 to 5 eV. It was expanded down to 0.5 and up to 6 eV according to near-normal reflectance measurements [13]. The optical properties of titanium above and below 1 eV were taken from [14] and [15], respectively. Details on the optical properties of the substrates can be found in Appendix D.

References

1. F. Wooten, *Optical properties of solids*. 1st ed., Academic Press, New York, London (1972).
2. A. Sadao, *Optical properties of crystalline and amorphous semiconductors: materials and fundamental principles*. Kluwer Academic Publishers, Norwell (1999).
3. H.G. Tompkins and W.A. McGahan, *Spectroscopic ellipsometry and reflectometry, A users guide*. 1st ed., John Wiley & Sons, Inc., New York (1999).
4. R.M.A. Azzam and N.M. Bashara, *Ellipsometry and polarized light*. 1st ed., North-Holland publishing company, Amsterdam, New York, Oxford (1977).
5. G.E. Jellison, Jr., *Thin Solid Films* **234** (1993), 416.
6. F. Abelès, *Ann. de Physique* **5** (1950), 596.
7. P.C.S. Hayfield and G.W.T. White, in *Ellipsometry in the Measurement of Surfaces and Thin Films*, E. Passaglia, R.R. Stromberg, and J. Kruger (Editors). Natl. Bur. Std. Misc. Publ. 256, US Government Printing Office, Washington DC (1964).
8. D.E. Aspnes, J.B. Theeten, and F. Hottier, *Phys. Rev. B* **20** (1979), 3292.
9. F.K. Urban, P. Ruzakowski Athey, and M.S. Islam, *Thin Solid Film* **253** (1994), 326.
10. D. Mergel, *Thin Solid Films* **397** (2001), 216.
11. J. Aarik, A. Aidla, V. Sammelselg, and T. Uustare, *Journal of Crystal Growth* **181** (1997), 259.
12. G.A. Battiston, R. Gerbasi, A. Gregori, M. Porchia, S. Cattarin, and G.A. Rizzi, *Thin Solid Films* **371** (2000), 126.
13. O. Banakh and P.E. Schmid, private communication.
14. *CRC Handbook of chemistry and physics*. 67th ed., CRC Inc., Boca Raton (1986).
15. *American Institute of Physics handbook*. McGraw-Hill, Inc., (1982).

Chapter 6 Water vapor as reactive gas

6.1 Introduction

One of the most important parameters for the fabrication of oxide thin films by sputtering is the choice of the reactive gas in the sputtering process. An alternative to O_2 gas as an oxygen source is water vapor. The H_2O molecule can be decomposed in the plasma and/or on the sample surface during deposition and introduce its O-atom into the deposited film. Water vapor has been used for reactive magnetron sputtering of transparent conducting oxides (TCO), such as indium tin oxide [1, 2] and ZnO [3]. Recently researchers started to investigate its influence on film properties of sputtered titanium oxides [4-7] and oxinitrides [8].

Depositing anatase thin films with water vapor Jeong et al. [7] have obtained n-type semiconducting anatase thin films with conductivities in the order of 100 Sm^{-1} and carrier densities in the order of 10^{18} cm^{-3} . In contrast to this, films deposited with oxygen were either pure insulating anatase or anatase containing metallic Ti_nO_{2n-1} depending on the oxygen partial pressure.

A. Bally [5] has found important differences in the film properties depending on whether oxygen or water vapor was used as reactive gas. With water vapor he obtained slightly substoichiometric thin films of mostly rutile TiO_2 with a high electrical conductivity and a good transparency. For low water vapor partial pressure during deposition an absorption band below 1 eV appeared and a blue shift of the fundamental absorption edge was observed.

A. Bally has proposed a model explaining the features of his samples [5]. The presence of water during film deposition induces unsaturated titanium bonds at the grain surfaces. Partly reduced Ti atoms at the grain surfaces act as electron donors similar to oxygen defects in the TiO_2 bulk [9, 10]. The electrons are injected into the bulk of the TiO_2 grains and form a free electron gas. He has reported plasma energies $\hbar\omega_p$ in the order of 0.5 to 3.5 eV. For a $TiO_{1.93}$ thin film a free electron density of $4.5 \cdot 10^{21} \text{ cm}^{-3}$ and a corresponding effective mass m^* of $2.2 m_e$ have been estimated. From the damping term $\hbar\gamma_p$ in the order of 2 to 2.5 eV he has obtained a charge carrier mobility between 0.21 and $0.26 \text{ cm}^2\text{V}^{-1}\text{s}^{-1}$. His samples showed semiconducting properties with thermal activation energies of the DC conductivity in the range of 75 to 95 meV. This model was largely based on models of transmittance measurements at photon energies above 0.5 eV.

In the present chapter some of these results are revisited and new series of samples deposited with water vapor are presented and discussed. Furthermore, complementary measurements are presented in an attempt to further clarify what is happening when using water vapor as a reactive gas. Important results have been obtained from spectrophotometry measurements in the infrared spectral region down to 0.05 eV. At these low energies the proposed free electron gas should be observed most readily.

6.2 Reactive sputtering with water vapor

The samples discussed in the present chapter have been deposited with water vapor as reactive gas. Details on the sputtering installation are presented in Chapter 3. Table 6.1 lists the basic deposition parameters. The total pressure of the process gas was kept constant at $2.5 \cdot 10^{-3}$ mbar whereas the water vapor partial pressure was varied. The evolution of the deposition rate is presented in Figure 6.1. At high H_2O partial pressures the target was fully oxidized and the growth rate was low. The low rate was due to the high pumping speed of 160 ls^{-1} . In this pressure region, mainly rutile was deposited. With decreasing partial pressure, at roughly 20 to 16 %, the samples contained the anatase phase. In the discussion at the end of the present chapter it will be shown that anatase is likely to have an important influence on the electrical and optical properties of the films. When the partial pressure was decreased further no anatase was observed anymore and the samples became more amorphous. When the target surface became gradually more metallic the deposition rate increased and the samples turned dark blue. Due to the high pumping speed no instabilities in the plasma (hysteresis effect) occurred [11]. Below about 8 % H_2O partial pressure the films were metallic consisting of a mixture of amorphous, Ti_2O_3 and Ti_3O_5 phases as determined by XRD.

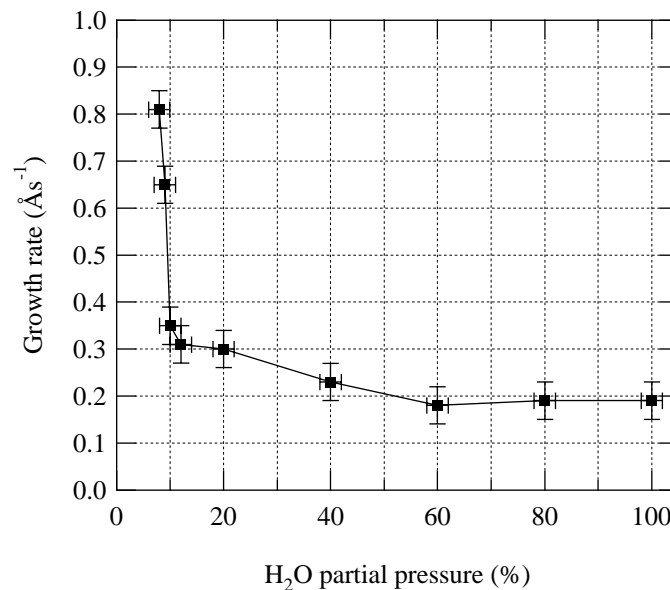


Figure 6.1: Growth rate of TiO_2 samples as a function of reactive gas partial pressure. The line is a guide to the eye.

Because of the low deposition rate, a good long time stability of the process was needed. During the deposition the plasma composition was monitored by a quadrupole mass spectrometer. The water vapor resulted in the presence of OH and H radicals in the plasma.

Total pressure	2.5·10 ⁻³ mbar
H₂O partial pressure	0 - 100 %
Sputtering current	300 mA (DC)
Substrate temperature	180 °C / 250 °C
Target to substrate distance	9 cm
Pumping speed	160 ls ⁻¹

Table 6.1: Deposition parameters for water-deposited films.

In total, four series of samples have been prepared. The differences between the series consisted mostly of minor modifications in the sputtering machine. The configuration used for Series (a) was a reconstruction of the older configuration used for Series (c). This configuration is the same as has been used in the work of A. Bally [5]. The two configurations differ in the deterioration of the magnets in the magnetron. Series (b) differs from the others in the presence of a chimney (ground shield) around the titanium target and a gas inlet in vicinity of the target. This configuration was mounted for the deposition of the multilayers discussed in Chapters 7 and 8. The chimney was added to confine the plasma and reduce diffusion of sputtered material around the closed shutter during target conditioning [12]. The configuration (d) corresponds to (a) and (c) but with a different magnetron. The changes in the configurations resulted in a slight shift in the reactive gas partial pressure necessary to obtain comparable film properties. The results obtained for samples of the different series were consistent.

	Series (a)	Series (b)	Series (c)	Series (d)
Chimney	none	steel	none	none
Gas inlet	chamber	vicinity of target	chamber	chamber
Magnets	SmCo (~4 kG)	SmCo (~3 kG)	SmCo (~3 kG)	SmCo (~3 kG)
Target Power	123 W	114 W	126 W	137 W
Target	A315 of AJA ⁵	A315 of AJA	A315 of AJA	MAK of Caburn

Table 6.2: Modifications in sputtering machine for the sample series shown in Figure 6.9. The target power is that required for a deposition at 300 mA, with 20 % H₂O partial pressure. The other parameters are listed in Table 6.1.

⁵ AJA international Inc.

6.3 Results

The subsequent discussion concentrates on titanium oxide films close to the stoichiometric composition. Substoichiometric films deposited with water vapor have been investigated by Bally et al. [4, 5] and Banakh et al. [6].

6.3.1 Chemical composition

The chemical composition of the samples was determined by a combination of Rutherford backscattering spectroscopy (RBS) and elastic recoil detection analysis (ERDA). These techniques are complementary and the measurements were performed in parallel (Section 4.2.2). As an example, Figure 6.2 shows the RBS spectra of two comparable dioxide films. One film was obtained with oxygen and the other one with water vapor as reactive gas. For every sample RBS measurements were performed at two different incidence angles with a 2 MeV He^+ ion beam. The spectra in the figures were collected at a grazing incidence angle of 76° . The scattering angle was 150° .

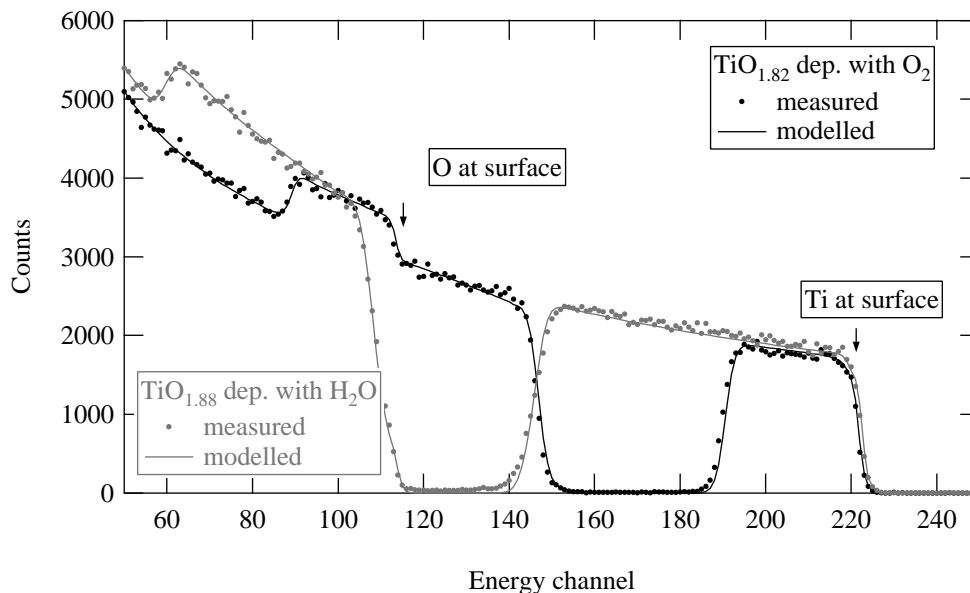


Figure 6.2: RBS spectra of comparable titanium dioxide films deposited in O_2 and H_2O ambient, respectively. 2 MeV He^+ ions at grazing incidence angle of 76° were used. The scattering angle was 150° . The width of the O and Ti signals are related to the different sample thicknesses (109 nm and 232 nm).

The corresponding ERDA spectra are depicted in Figure 6.3. For these measurements the scattering angle was 20° . The peaks correspond to hydrogen present at the surface of the samples. It was observed for samples deposited with oxygen as well as for water-deposited samples. The measurements were done ex-situ and the samples were not heated in vacuum. The observation of a hydrogen signal at the surface is quite common for thin film samples. It is typically related to water and hydrocarbon contamination. The hydrogen concentration was 6 to 9 at% in a layer of typically 7 to 12 nm thickness. One could try to relate these values to grain size, surface roughness, and typical dimensions of intergranular spacing, but the depth resolution for ERDA is lower than for RBS. Since the measured quantity is the areal density

N_t and not the thickness it is possible that the layer is thinner and the concentration of H is proportionally higher.

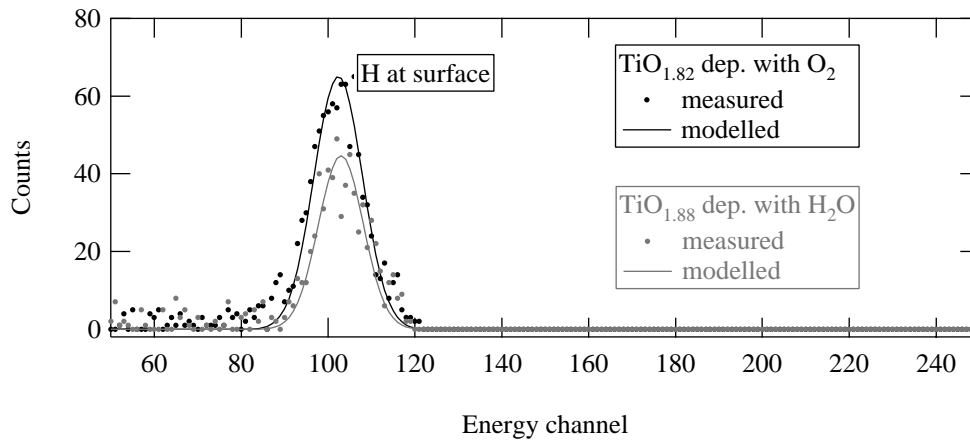


Figure 6.3: ERDA spectra of comparable titanium dioxide films deposited with O₂ and H₂O, respectively. 2 MeV He⁺ ions at grazing incidence angle of 76° were used. The scattering angle was 20°.

For both types of samples no hydrogen was found above the detection limit of 0.5 at% below this top layer containing hydrogen. It is worth noting, however, that the undetected presence of, say, 0.1 at% H in the oxide can have a dramatic effect on the electrical transport properties.

6.3.2 Morphology and crystalline structure

6.3.2.1 X-ray diffraction

Grazing incidence X-ray diffraction patterns obtained on Series (a) of samples deposited with water vapor are shown in Figure 6.4. From bottom to top they were deposited at increasing partial pressure of H₂O in the plasma. At the left of the figure the chemical composition obtained by RBS is indicated. At the bottom a pattern of a TiO_{1.99} film deposited with oxygen as reactive gas is displayed. For the sputtering conditions in this work a strong dominance of anatase was observed for all samples deposited with oxygen.

When enough reactive gas is present in the plasma the films start to crystallize in titanium dioxide phases. The pattern shown at the bottom had 8 % H₂O partial pressure, just sufficient to develop small crystallites (14 nm). The crystallinity was about 60 % for this example. With increasing partial pressure the anatase phase appears along with rutile. For 20 % H₂O partial pressure in the plasma the anatase content reaches a maximum and the sample is well oxidized. Very high partial pressure (60 %) of water vapor seems to be less favorable for oxidation of the film. No anatase was observed at such high H₂O partial pressures. For samples deposited above 20 % water partial pressure the crystallinity reached 80 % and more. Comparing with the diffraction pattern of isotropic powder [13] the rutile (110) peak was stronger than the other rutile peaks. This indicated a texture in the rutile phase. For anatase no such preferential orientation was distinguished.

The anatase content was much more important in the samples deposited with oxygen, whereas when using water little anatase was present. This indicates that the presence of H and/or OH radicals is somehow disturbing the crystalline growth of anatase. It has been reported that physical properties of TiO₂ thin films depend very sensitively on the deposition parameters, such as substrate temperature and reactive gas pressure [14].

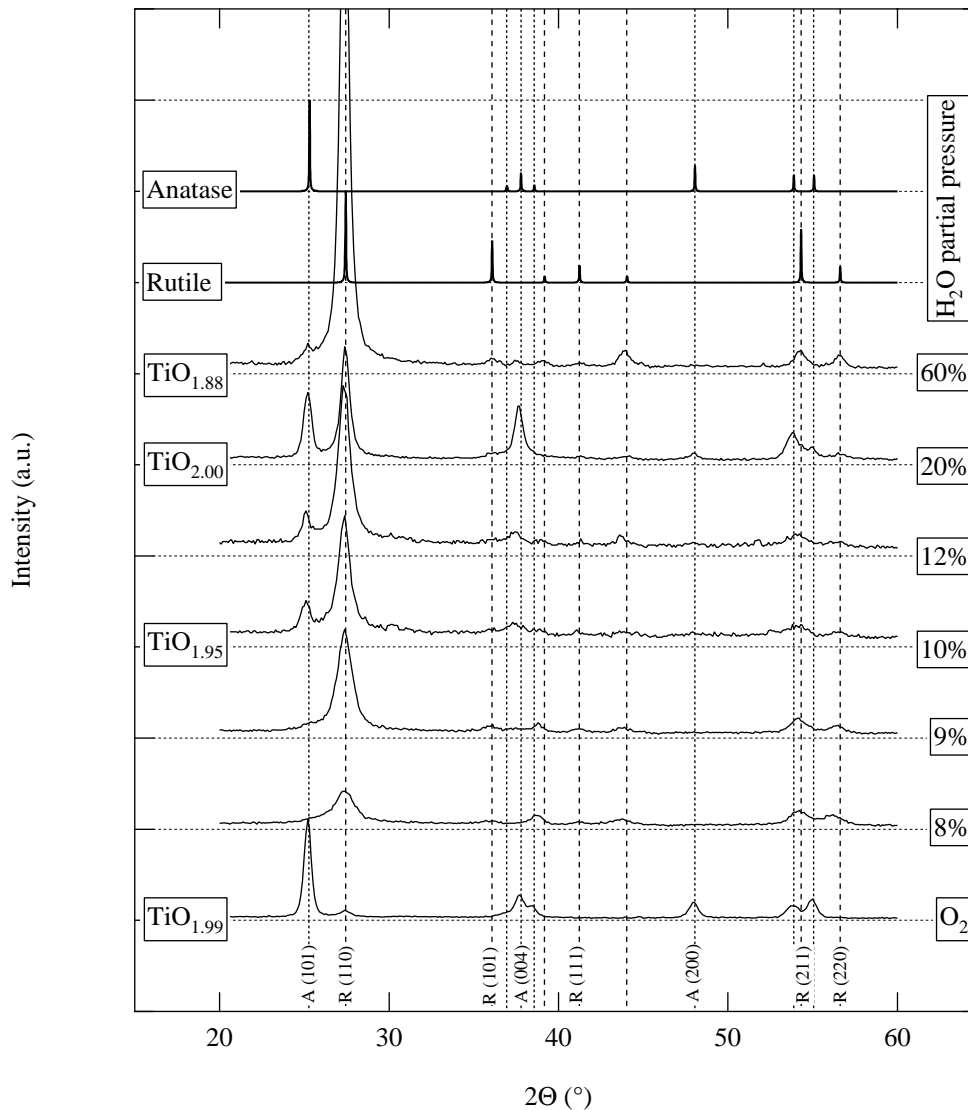


Figure 6.4: Grazing incidence XRD pattern of water-deposited samples measured on Si substrates. The intensity has been rescaled according to the film thickness. The vertical lines mark the peak positions of rutile (dashed, labeled R) and anatase (dotted, labeled A) as given in [13]. The reference powder diffraction patterns of anatase and rutile are plotted in the upper part. The most important peaks are the (101) peak for anatase at 25.281° ($d_{A(101)} = 3.520$) and (110) for rutile at 27.446° ($d_{R(110)} = 3.247$).

The grain size for anatase and rutile was determined from the XRD peak width. In Figure 6.6 it is reported for the samples deposited with water vapor. It varied between 10 and 50 nm with larger grains in stoichiometric films. Similar grain sizes and the same tendency towards larger grains closer to stoichiometric composition were observed in films deposited with O₂.

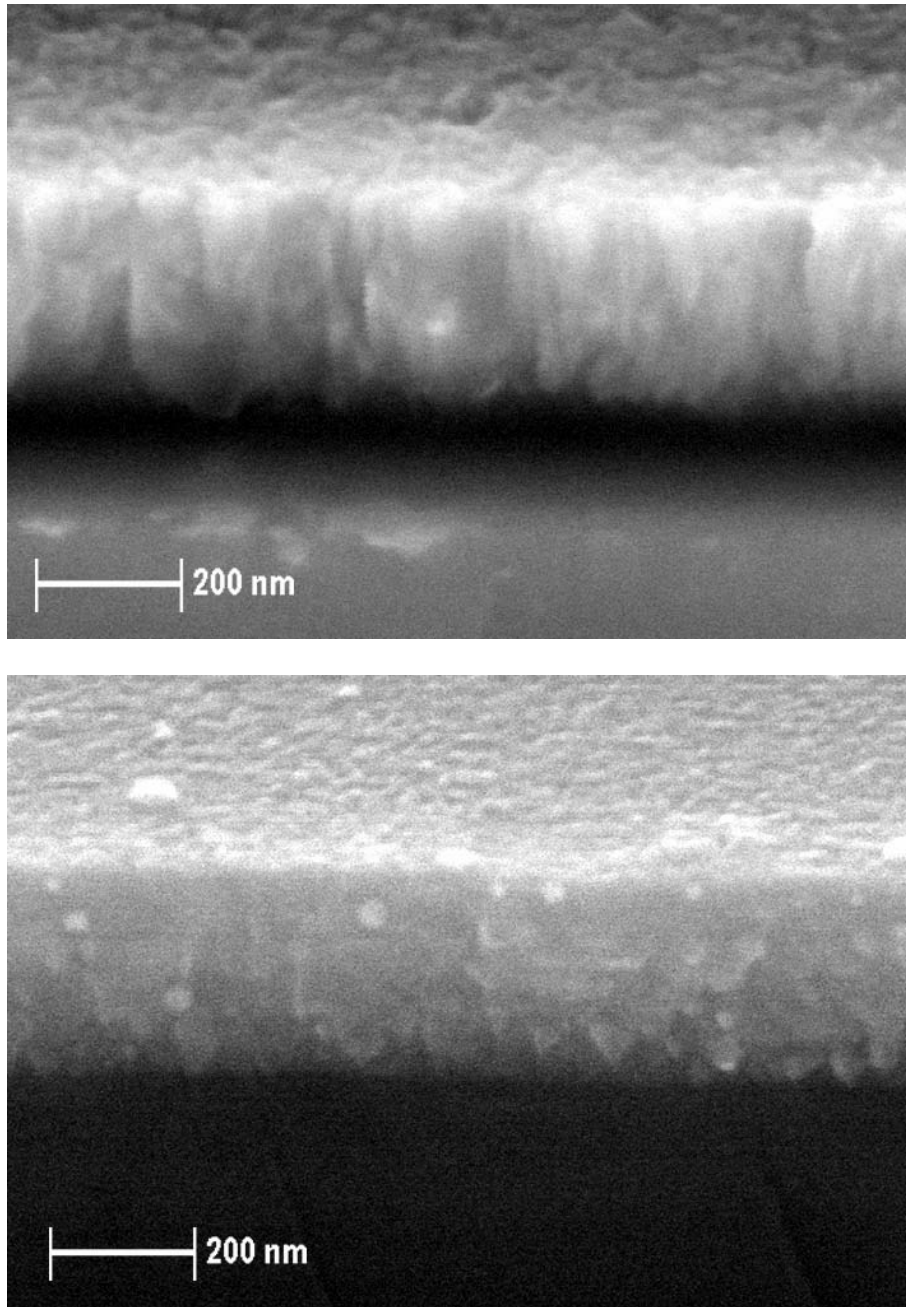


Figure 6.5: SEM images of $\text{TiO}_{1.85}$ deposited with oxygen (top) and of $\text{TiO}_{1.92}$ deposited with water vapor (bottom) as reactive gas.

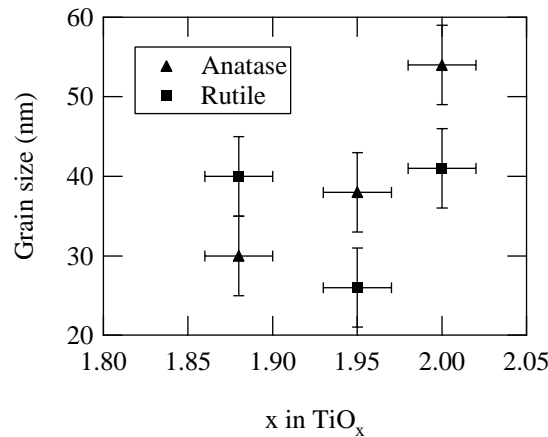


Figure 6.6: Grain size of water-deposited films as a function of chemical composition measured by RBS.

6.3.2.2 SEM observation of the film morphology

To get further insight into the difference in film morphology induced by the choice of the reactive gas, scanning electron microscopy (SEM) pictures were taken. In Figure 6.5 two images obtained on samples of both types are shown. The pictures show cleaved sections of the silicon substrates (bottom) and the films (middle). The upper part shows the view on the top surface. The sample deposited with oxygen was 240 nm thick. Its crystallinity was over 80 %. The grains and a columnar microstructure can clearly be distinguished. On the surface a kind of holes can be discerned. The second picture was taken on a 313 nm thick sample deposited with water vapor with a crystallinity of 70 %. The lighter and round grains could correspond to traces of anatase in the film. However, the anatase content was too small to yield an XRD signal. Therefore, the grains are likely to be debris from the cleaving of the sample. The surface looks smoother and no columnar contrasts are visible. This agrees with the assumption that grain surface modifications occur when water vapor is used [4-6].

6.3.2.3 Density determination from RBS and profilometry

From the RBS and ERDA spectra the areal atomic density N_t was obtained. From this and the thickness obtained from profilometry measurements the film density ρ_{film} was determined according to Equation 4.5. The results are plotted in Figure 6.7. Literature values for the bulk materials are indicated in the figure. Not shown is the density of TiO which is equal to 4.93 g/cm^3 . Films deposited with water vapor as oxidizing species have a higher density than the films deposited with oxygen. This can mostly be explained by the lower anatase content of water-deposited samples. Close to stoichiometry the density of these films is reduced compared to rutile due to an amorphous fraction of 20 to 35 %. The variation in the densities of the oxygen-deposited samples is in agreement with the difference in the amorphous content of 45 % for the $\text{TiO}_{1.82}$ and 20 % for the $\text{TiO}_{1.99}$ sample, respectively.

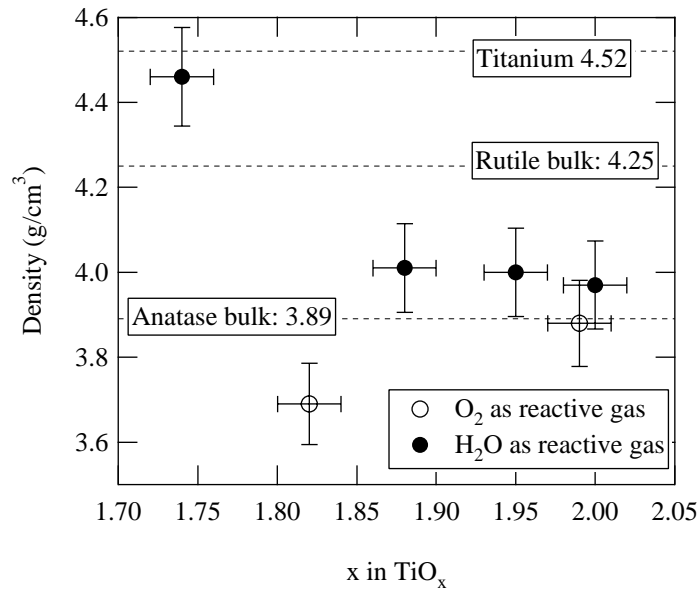


Figure 6.7: Density as a function of chemical composition for films deposited with O₂ and H₂O, respectively. Chemical composition and density were obtained from RBS measurements and the profilometer thickness. The density of titanium monoxide is 4.93 g/cm³. Literature values were taken from [13, 15].

6.3.2.4 Thickness and density determination from XRR

X-ray reflectivity (XRR) is used for obtaining information about the layer thicknesses, densities and interface roughnesses of thin films [16-18]. Experimental details are given in Section 4.1.3 and further details on the XRR technique can be found in the Appendix E.

In Figure 6.8 the X-ray intensity specularly reflected by a 109 nm thick TiO_{1.82} sample is presented. The plateau at low incidence angle α_i is due to total reflection of incident X-rays. At about $\alpha_i = 0.27^\circ$ the critical angle α_c is reached. Above this angle the X-rays enter the film and the reflected intensity decreases rapidly. The slope of the signal is influenced by the surface roughness [16, 17]. Multiple reflections in the titanium oxide layer cause the interference fringes (Kiessig fringes [16]). They can nicely be seen between about 0.3 and 1.2°. The fringes are damped towards higher angles due to the interface and surface roughness [16]. In addition, the intensity is modulated with a wide oscillation. This was attributed to the SiO₂ layer between the substrate and the film. The maxima at 1.0 and 1.5° correspond to a layer thickness of 7 nm. In the present case the intensity at high α_i is very sensitive on the interface roughness between the SiO₂ and the TiO₂ layers (2 Å of roughness correspond to a factor 2 in intensity).

Two different approaches were followed to analyze the reflectivity patterns. The position of the interference fringes depends on the thickness and the electron density of the investigated film. Rusli et al. [19] have proposed an algorithm to determine both the thickness and the density of a single layer from the Kiessig fringe positions. In a second approach a modelled curve was fitted to the reflectivity data. Details on both techniques are given in Appendix E.

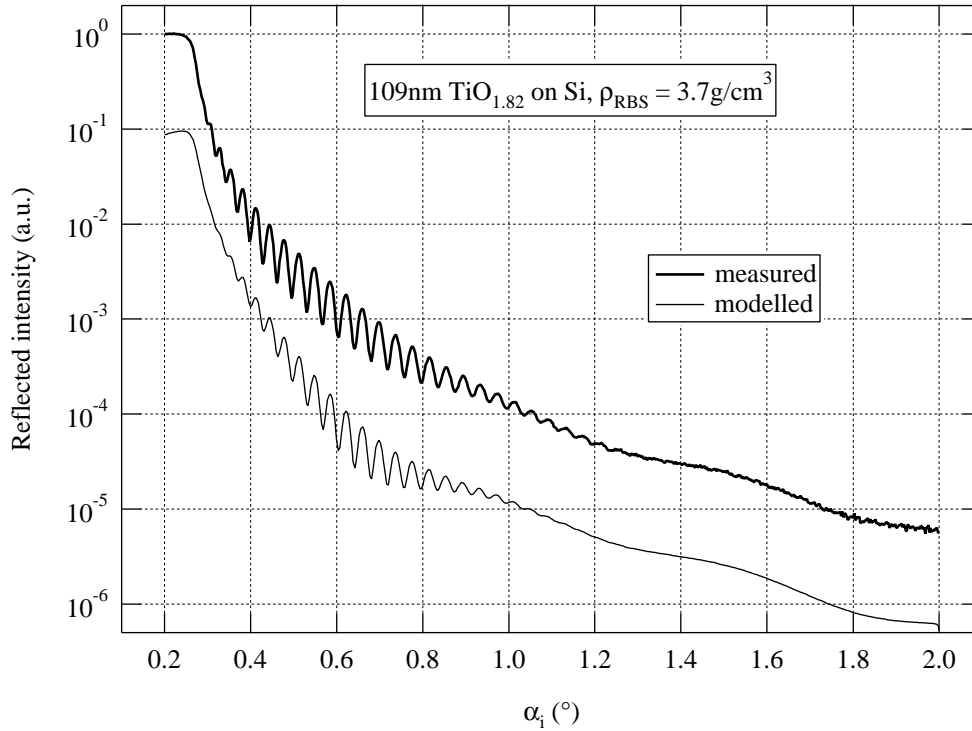


Figure 6.8: Reflected X-ray intensity as a function of angle of incidence. For clarity the modelled intensity has been divided by ten. The sample properties and model parameters are listed in Table 6.4.

A thermally oxidized Si wafer was chosen to test the method. The thickness of the silicon oxide layer was determined to be 114 nm by ellipsometry. The density of dry thermal SiO_2 is 2.24 g/cm^3 [20]. These values are listed in Table 6.3 together with the results obtained from XRR. The mass density was calculated from the electron density according to Equations E.14 and E.15. In this calculation the chemical composition was accounted for according to Equations E.18 and E.19.

Parameter	Reference values	XRR Kiessig fringes	XRR Modelling
t_{RMS} (nm)	---	---	1 ± 0.1
t (nm)	114 ± 1 (Ellips.)	113 ± 1	113 ± 0.5
ρ_{film} (g/cm^3)	2.24 [20]	2.26 ± 0.2	2.2 ± 0.1

Table 6.3: Test of the validity of the XRR model: The thickness t and density ρ_{film} of a thermally oxidized silicon wafer have been determined from the position of the maxima of Kiessig fringes in XRR measurements (Rusli's algorithm [19]) and from modelling the XRR data. They are compared to values obtained by other techniques.

Corresponding values for the example shown in Figure 6.8 are listed in Table 6.4. The evaluation of the film thickness and density from the Kiessig fringe position according to Rusli et al. [19] was found to be very valuable. Even neglecting the native SiO_2 layer on the substrate, good thickness and density values were obtained (compare columns 2 and 3 in Table 6.4). The SiO_2 layer thickness t_{SiO_2} was measured by TEM on the cross section of a sample deposited with the same parameters. The thickness of 106 ± 1 nm compared well to

what was found by profilometry (109 ± 5 nm). The density of 3.5 ± 0.2 g/cm³ corresponded within the experimental errors to what was determined from the RBS areal density N_t and the profilometry thickness (3.7 ± 0.1 g/cm³, Equation 4.5).

The information obtained from the Kiessig fringes by Rusli's procedure proved very useful as input parameters for the fitting process. Without this information it would have been difficult to identify the right order of the interference fringes. If the fringe order is shifted the thickness and density values will be significantly wrong. For the TiO_{1.82} sample the calculated intensity corresponding to a best fit based on a model structure of three distinct homogeneous layers is depicted in the figure. The corresponding parameters are listed in column 4 of Table 6.4. The structure consisted of a TiO₂ layer on a 7 nm thick SiO₂ intermediate layer and the Si substrate. The SiO₂-TiO₂ interface (0.3 nm) and the surface roughness (2 nm) were taken into account as a Gaussian distributed variation in the layer thicknesses. Note that the angular position of the fringes is modelled quite accurately. An error in amplitude around 0.4° could be due to a thin, supplementary layer not properly included in the model. The results obtained from the model calculation were in good agreement with the other techniques (Table 6.4).

Parameter	Measured	XRR Kiessig fringes	XRR Modelling	Optical Modelling
t_{RMS} (nm)	---	---	2 ± 0.2	4 ± 2
t (nm)	109 ± 5 (Profilo.)	106 ± 1	107 ± 0.5	104 ± 1
t_{SiO_2} (nm)	8 ± 1 (TEM)	---	7 ± 0.5	7 ± 1
ρ_{film} (g/cm ³)	3.7 ± 0.1 (RBS)	3.5 ± 0.2	3.5 ± 0.2	3.7 ± 0.4

Table 6.4: Properties a TiO_{1.82} sample determined from different techniques in comparison to the modelling of XRR data and the analysis of Kiessig fringe position according to Rusli's algorithm [19]. Properties listed are the surface roughness t_{RMS} , the film thickness t , the thickness t_{SiO_2} of the SiO₂ layer between the substrate and the film, and the density ρ_{film} . The density in the optical model corresponds to a void content of 8.5 ± 2 vol% in an anatase/rutile/amorphous matrix with a specific mass of 4.0 g/cm³.

6.3.3 Electrical conductivity

The electrical conductivity σ_{DC} of samples deposited with water vapor was measured in the van der Pauw configuration on glass substrates (Section 4.3). The results obtained on samples of Series (a), (b) and (c) (Table 6.2) are reported in the Arrhenius plots in Figure 6.9.

All samples showed a semiconductor behavior with thermally activated conductivity. According to the different electrical and optical properties three groups of samples can be distinguished. The groups will be called A, B and C as explained in Table 6.5. Type A samples had a high conductivity and a low activation energy. They were highly substoichiometric and metallicly reflecting in different colors: from golden over brown to gray. According to XRD measurements they did not consist of TiO₂ phases but rather of mixtures of amorphous, Ti₂O₃ and Ti₃O₅ phases. They will not be discussed any further in the present work.

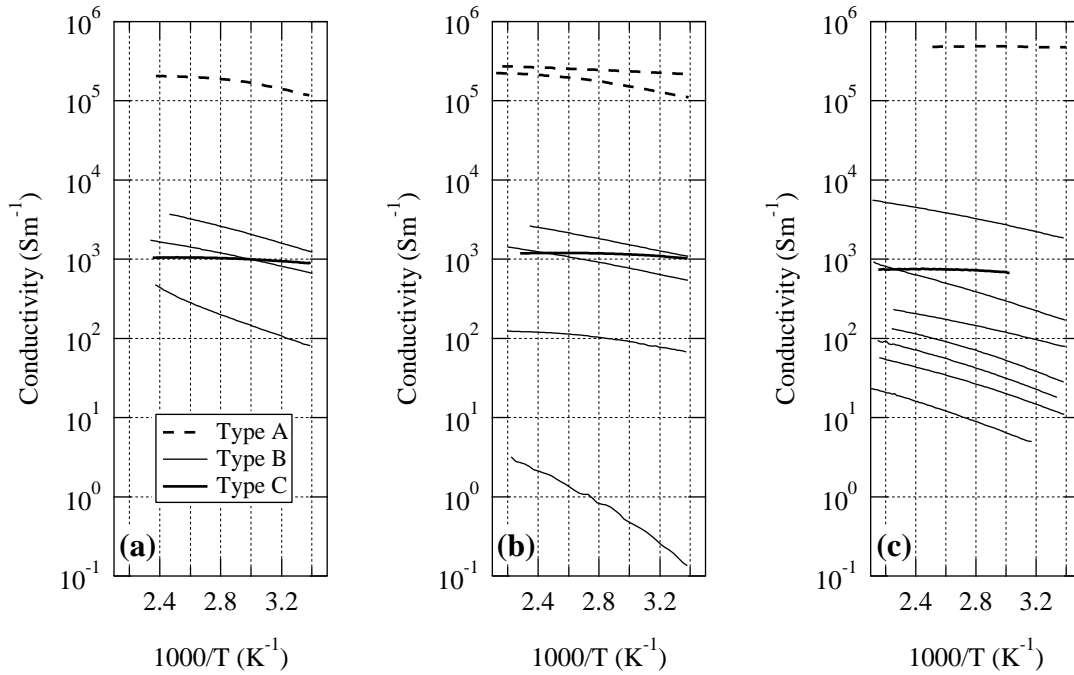


Figure 6.9: Behavior of electrical conductivity with temperature. The three figures show samples deposited with three slightly different machine configurations. For the definition of Types A, B and C see Table 6.5.

The samples of Type B consisted of the rutile phase. Their activation energy E_A at room temperature varied around 80 meV and increased to the order of 130 meV for samples with a conductivity below 100 Sm^{-1} (details see Table 6.8 and Figure 6.23). The behavior of σ_{DC} with increasing temperature corresponds to that of a doped semiconductor with partial compensation [21]. This is often observed in oxide semiconductors [22]. These samples were increasingly transparent with decreasing conductivity. Down to 100 Sm^{-1} they displayed a gray-bluish color. The blue color in transmission can be explained by the presence of an absorption band in the IR [23, 24].

Type	$\sigma_{DC} (\text{Sm}^{-1})$	E_A (meV)	XRD phases	Transparency
A	$> 10^4$	7 - 70	amorphous, Ti_2O_3 , Ti_3O_5	opaque
B	10 - 1'000	70 - 130	rutile	absorption band
C	500 - 2'000	18 - 38 (57)	rutile + anatase	little absorption

Table 6.5: Three groups of samples can be distinguished according to their electrical and optical properties. The detailed values for every sample are listed in Table 6.8 on page 63.

The samples of Type C had a conductivity around $1'000 \text{ Sm}^{-1}$. They struck attention by their low activation energies of 20 to 38 meV. In comparison with other samples with similar σ_{DC} they displayed a higher IR transparency. Their exceptional optical behavior will be presented later. Unlike the other samples the samples of Type C contained anatase. The chemical composition x in TiO_x for Series (a) has been determined to 2.00 ± 0.02 by RBS. For Series (b) and (c) the less sensitive EPMA technique has been used: x was 1.99 ± 0.1 for (b) and 2.02 ± 0.1 for (c). Assuming oxygen vacancies to act as single donor sites the charge

carrier density of $7 \cdot 10^{19} \text{ cm}^{-3}$ (see Section 6.4.1) translates to $\text{TiO}_{1.998}$. This explains why an electrical conducting sample can show stoichiometric composition in the RBS measurements.

6.3.4 Optical properties

Transmittance measurements at normal incidence on glass substrates complemented reflectance and ellipsometry measurements on silicon substrates. In the transmission configuration the observed spectral range was expanded to 0.05 eV by measurements on Si substrates. The optical models presented in the subsequent paragraphs are based on a Bruggeman effective medium approximation combining literature data for the dielectric function of anatase, rutile and voids. As starting parameters for the optimization process the knowledge of film properties discussed so far was very valuable. Further explanations on the optical models can be found in Chapter 5 and Appendices A to D.

6.3.4.1 Optical model for stoichiometric and insulating TiO_2

The approach for the optical analyses was firstly tested on spectrophotometry and ellipsometry measurements performed on stoichiometric samples deposited with oxygen. These films were insulating and did not show any absorption in the infrared. An example is discussed hereafter. In Figure 6.10 the transmittance and reflectance spectra measured on a 585 nm thick, $\text{TiO}_{1.99}$ (RBS), sample are presented. The crosses represent the measured data, whereas lines have been obtained by modelling. The titanium dioxide films deposited with oxygen were transparent up to the absorption edge. The corresponding ellipsometry spectra are shown in Figure 6.11.

From profilometry measurements the sample thickness t was known. The chemical composition was obtained from RBS measurements. The film density $\rho_{\text{film}} = 3.9 \text{ g/cm}^3$ was calculated from the thickness t and the areal density N_t measured by RBS (see Section 4.2.2). From XRD measurements the crystallinity was determined to 80 %. The crystalline part consisted of 80 % anatase. According to Equation 5.2 the void fraction f_{vac} was estimated to be 0.02. These input values and the results of the optimization process are summarized in Table 6.6. Every parameter was optimized on the respective configuration and energy range that reacts the most sensitively. In a first step the film thickness t was optimized on the transmittance and reflectance spectra. The absorption edges of anatase and rutile are located at not exactly the same energy (see Chapter 2). The anatase content in the samples was determined by optimizing the onset of the absorption in the transmittance spectra. The void content was found from the contrast of the fringes (the oscillation amplitude) in transmittance. The intensity of the fringe minima in transmittance depends on the contrast of the effective dielectric functions of the substrate and the TiO_2 film. Both the void content f_{vac} and anatase content f_A influence the interference fringe spacing. Ellipsometry and reflectance spectra are most sensitive to the surface roughness t_{RMS} at energies above the absorption edge. From the contrasts of the fringes in reflectance and ellipsometry the thickness t_{SiO_2} of the amorphous SiO_2 layer between the Si substrate and the film was found.

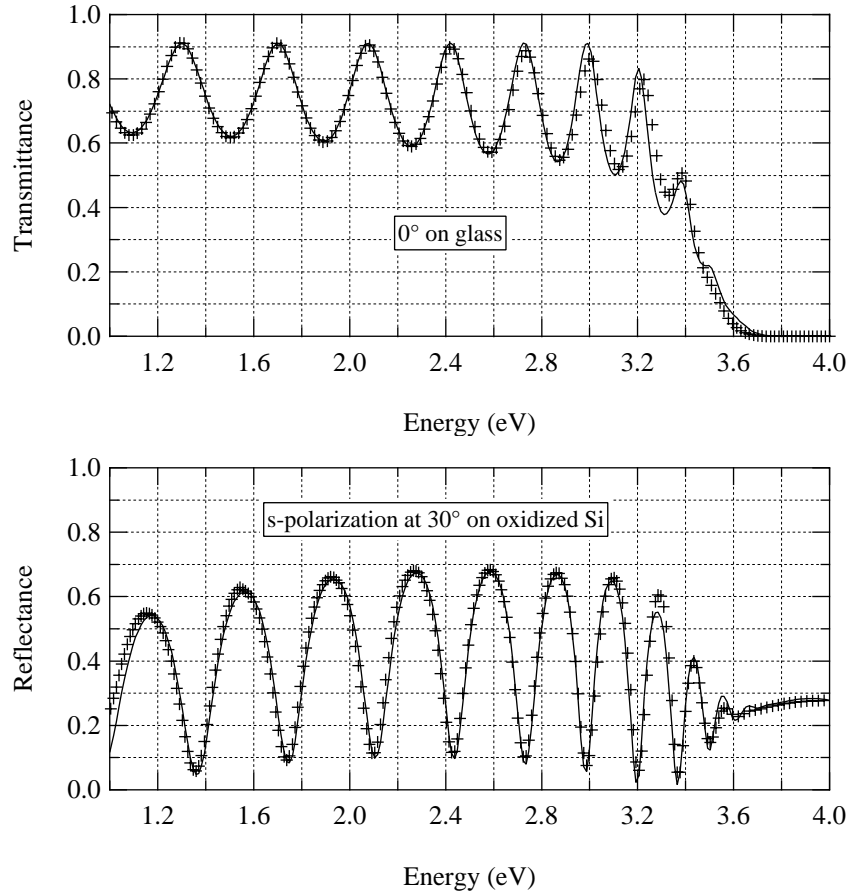


Figure 6.10: Measured (crosses) and modelled (lines) spectrophotometry of a 585 nm thick $\text{TiO}_{1.99}$ film. The model corresponds to a best fit obtained from an effective medium approximation (EMA) with anatase and rutile crystalline phases and voids. Model parameters are listed in Table 6.6.

Parameter	Measured	Optical model
t_{RMS} (nm)	---	7 ± 2
t (nm)	585 ± 15 (Profilo.)	575 ± 1
t_{SiO_2} (nm)	8 ± 1 (TEM)	7 ± 1
f_A (%)	80 ± 10 (XRD)	70 ± 10
f_{vac} (%)	2 ± 1 (Eqn. 5.2)	2 ± 2
x in TiO_x	1.99 (RBS)	2.0

Table 6.6: Measured film properties and parameters in the optical model. The sample had a density of $3.9 \pm 0.1 \text{ g/cm}^3$ (RBS) and a crystallinity of 80 % (XRD). Further details and definitions of the parameters are given in the text.

The fits for transmittance, reflectance and ellipsometry spectra indicate that the model dielectric function describes well the thin film material. The model parameters were very close to measured quantities. A good sample characterization proved useful for reducing the fitting parameter space. The model consisted of a mixture of anatase, rutile and voids. Accordingly, it can deal with TiO_x , $x = 2$. It should be noted, however that the optical properties of amorphous TiO_2 are badly defined [25] and have sometimes been assumed to be similar to anatase with a lower density [26]. In Figure 6.10 the absorption edge energy is smaller than the fitted value. This must be caused by the presence of 20 % amorphous TiO_2 which is not included in the model. Further, minor disagreements can be observed in Figure 6.11 for the same reasons.

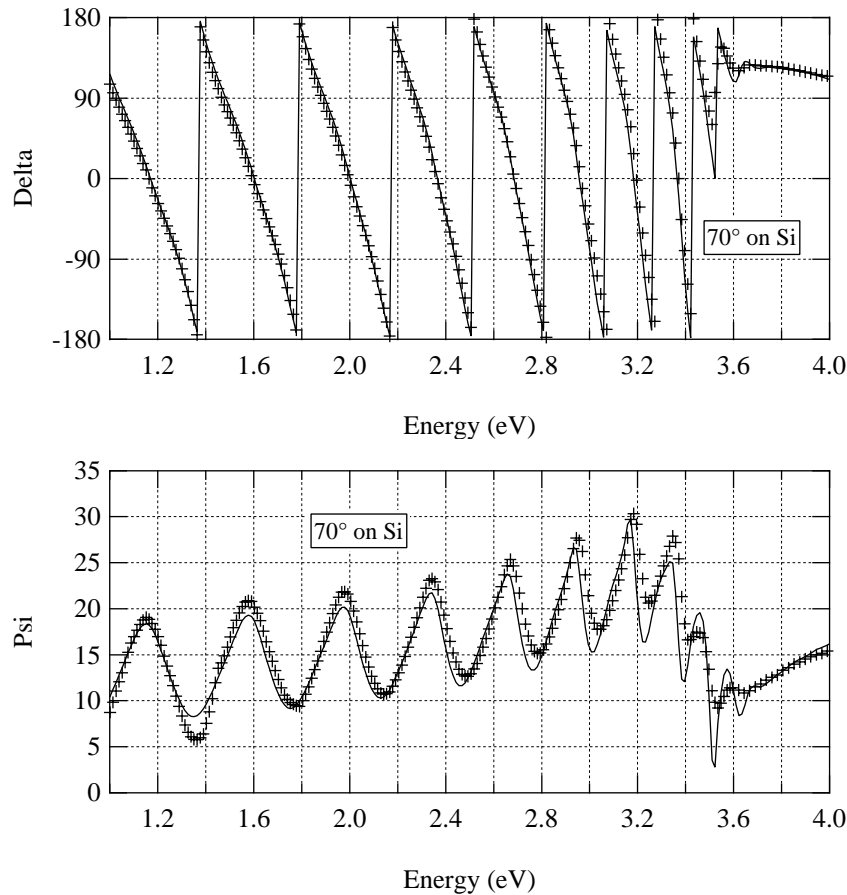


Figure 6.11: Ellipsometry spectra of a $\text{TiO}_{1.99}$ sample deposited with O_2 as reactive gas. Crosses represent the measured and lines represent the modelled values. The model is the same as in Figure 6.10.

6.3.4.2 Absorption in films deposited with H_2O vapor

The transmittance spectra measured on the samples of Series (a) deposited with water vapor are presented in Figure 6.12. The upper part of the figure shows the transmittance spectra measured at normal incidence on glass substrates. For a high water vapor partial pressure in the plasma (more than 10 %) the samples were transparent up to the fundamental absorption edge above 3 eV. In the transparent spectral region they showed the typical interference fringes between roughly 0.6 and 0.8 transmittance. For samples deposited at lower water partial pressures the transmittance was reduced around 1 eV. The range around the absorption edge is shown in Figure 6.13. The apparent absorption coefficient α' was determined from the transmittance T and the film thickness t according to the approximate expression of Lambert and Beer

$$\text{Equation 6.1} \quad \alpha' = -t^{-1} \cdot \ln(T)$$

The oscillations in the spectra at small α' -values are due to optical interference effects that are not accounted for by Equation 6.1. For comparison the absorption coefficient for isotropically oriented polycrystalline rutile and anatase are plotted in the figure. It has been calculated from the reference data (Section 2.3). The progressive absorption onset above roughly 3.3 eV in the thin film samples is due to the amorphous phase. In the amorphous phase, structural disorder causes band tails to develop below the absorption edge [27].

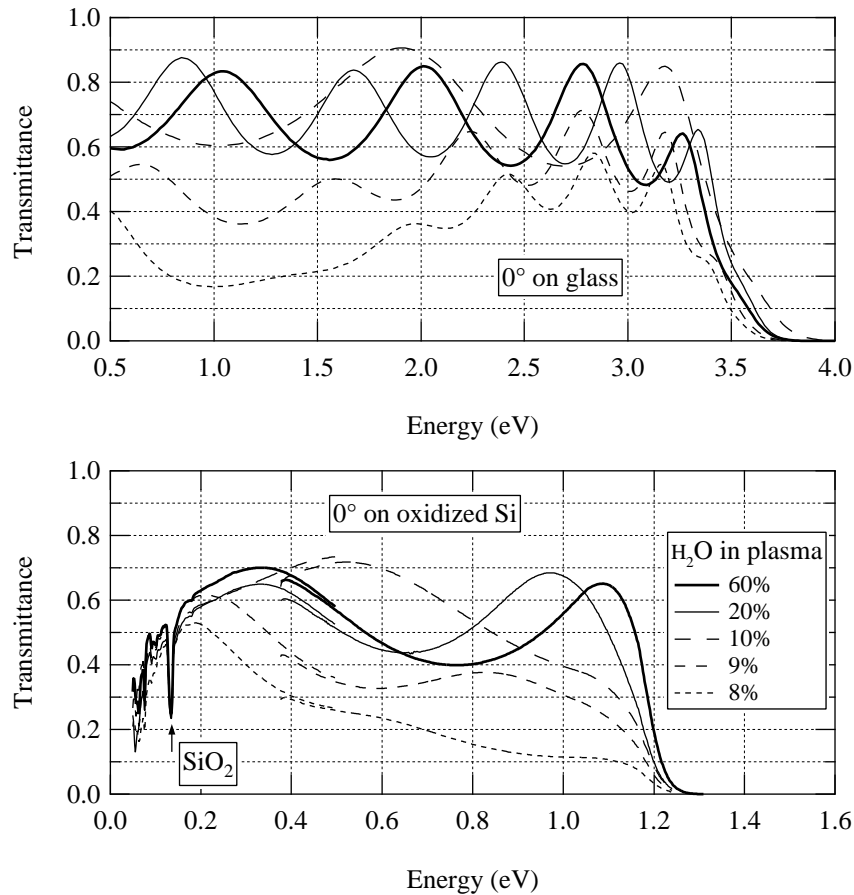


Figure 6.12: Transmittance spectra of a series of samples with different water partial pressure in the deposition process. Top: Spectra measured on glass substrates. Bottom: Combined Nexus FTIR and Cary spectrophotometer measurements on oxidized silicon substrates.

The transmittance measured on oxidized silicon substrates polished on both sides is shown in the lower part of Figure 6.12. Measurements taken on a Nexus FTIR and a Cary spectrophotometers have been combined (cf. Table 4.1). The spectral region where both measurements overlap can be seen around 0.4 eV. There is a slight discrepancy in the transmittance spectra. The difference was never larger than 0.02 in transmittance. The important absorption peak visible at 0.134 eV is due to phonon absorption in the SiO₂ layers on the surfaces of the preoxidized substrate. For samples deposited at lower water partial pressures the transmittance is reduced around 1 eV.

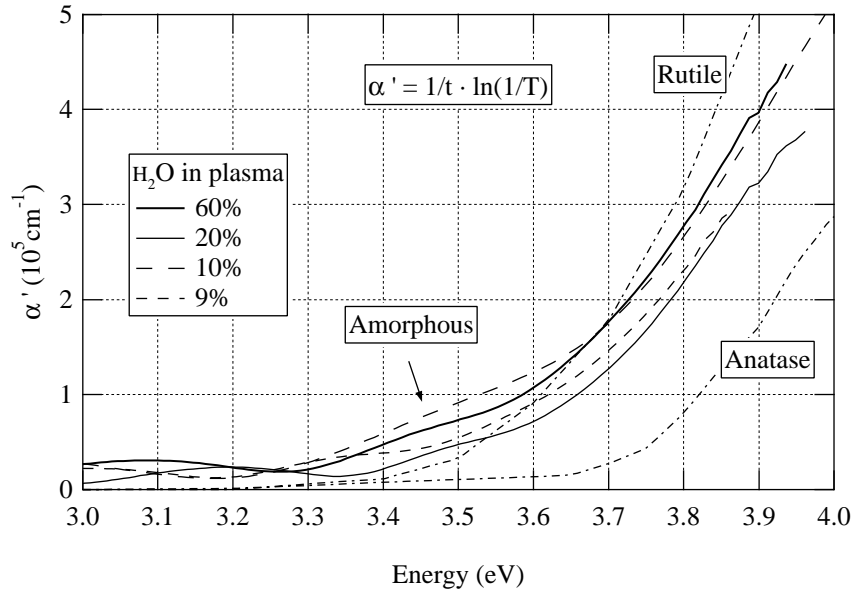


Figure 6.13: Absorption edge of the spectra shown in Figure 6.12. Absorption coefficients for polycrystalline rutile and anatase are shown for comparison. Amorphous TiO_2 displays a progressive absorption onset and a gap feature which is softer than the absorption edge of rutile and anatase.

Optical models have been developed taking advantage of the known film properties presented above. The occurrence of absorption at low energies in substoichiometric titanium dioxide films sputtered with water vapor has been reported by A. Bally [5]. He proposed free charge carriers and introduced a Drude term in the optical model in order to account for the additional absorption (see Appendix C, Equation C.3). Following the same approach Drude parameters ($\hbar\omega_p = 1.6$ eV and $\hbar\gamma_p = 1.5$ eV) were introduced in the rutile fraction of the material. Better results were obtained when the Drude term was replaced by a Lorentzian (Equation C.2). A Lorentzian has been chosen for commodity as it is successful in representing the IR absorption band observed in the oxide films. The corresponding parameters ω_l , f_l and γ_l were found by iteration. For one of the samples presented in Figure 6.12 (9 % H_2O partial pressure, $\text{TiO}_{2\pm 0.1}$ (EPMA), rutile, 30 % amorphous) the spectrophotometric and ellipsometric results are reported in Figure 6.14 and Figure 6.15. The transmittance spectra obtained on glass substrate (black) and on oxidized silicon substrate (gray) are plotted in the same figure. The crosses represent measured data, the dashed line the best fit that has been obtained with a Drude term and the solid line the best fit obtained with a model including a Lorentzian.

At energies above about 1 eV both models are optically nearly equivalent. At lower energies the Drude model displays a higher absorption. This can be seen mainly in transmittance in the infrared region. The model including a Lorentzian represents nicely the spectra in the IR region as well as over most of the observed spectral range.

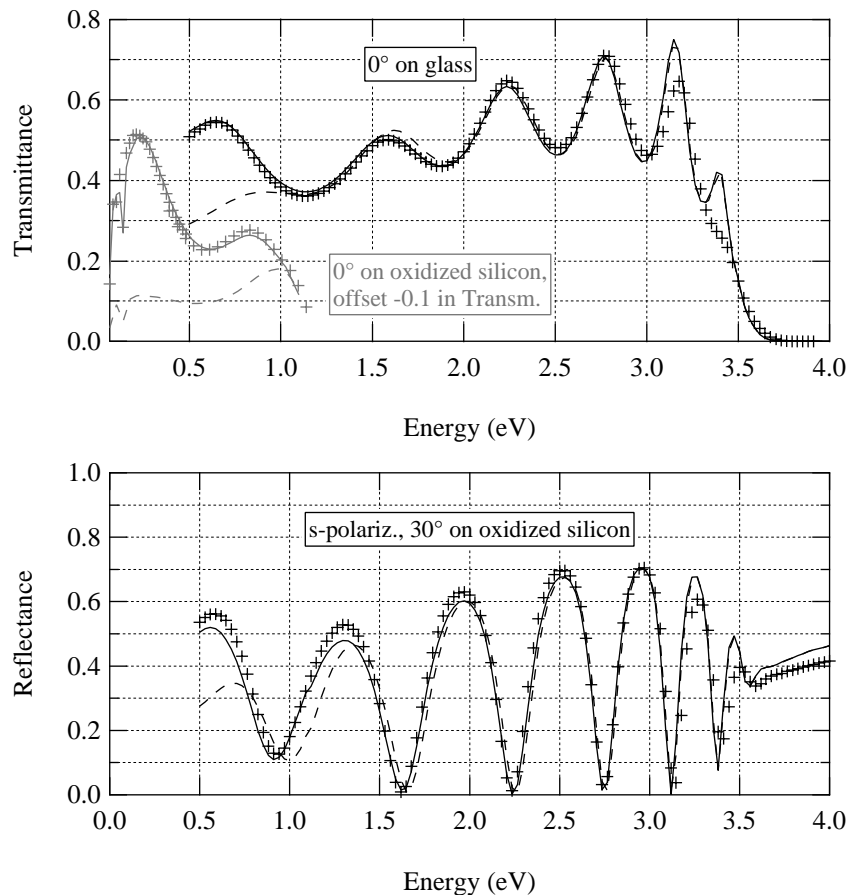


Figure 6.14: Transmittance on glass and on oxidized silicon substrates (top) and reflectance on oxidized silicon of a water-deposited film (9 % partial pressure, $\text{TiO}_{2\pm 0.1}$ (EPMA), rutile, 30 % amorphous). Measured (crosses) and modelled (lines) spectra are shown. Models consist of EMA of anatase and rutile with an additional Drude (dashed line) or Lorentzian term (solid line), respectively.

Discrepancies between the models and the measurement occur mainly around the absorption edge. The measured interference fringes in transmittance have lower contrast than the modelled ones. This is due to the fact that some extra absorption is not taken into account in the model. The difference between modelled and experimental data was more important for films with higher anatase content. It occurred in films deposited with both oxygen and water vapor. Optical properties in the region around the absorption edge depend critically on small features in ϵ_2 . For anatase the occurrence of Urbach tails⁶ has been reported [29, 30]. Furthermore, absorption bands just below the absorption edge have been observed for reduced anatase single crystals [31]. Finally, amorphous TiO_2 displays a progressive absorption onset below 3 eV, followed by a gap feature which is softer than the absorption edge of rutile (Figure 6.13).

⁶ A simple exponential energy dependence of the absorption coefficient near the fundamental absorption edge is denoted Urbach tail [27, 28].

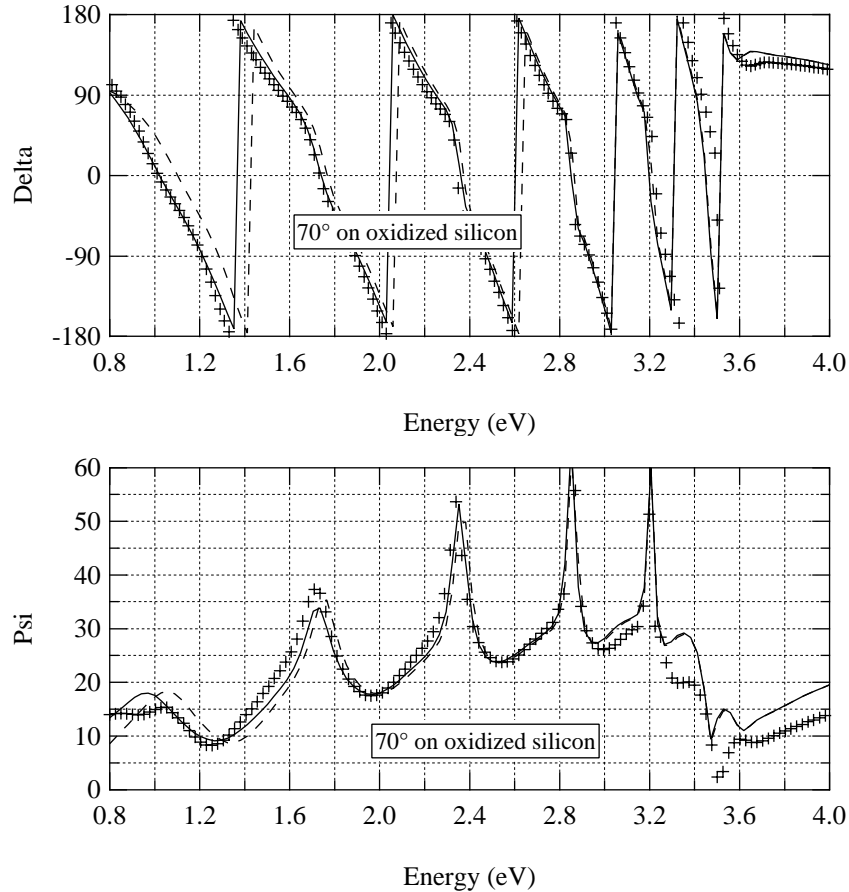


Figure 6.15: Measured and modelled ellipsometry spectra corresponding to Figure 6.14.

For the model spectra shown in Figure 6.14 and Figure 6.15 Drude parameters were $\hbar\omega_p = 1.6$ eV and $\hbar\gamma_p = 1.5$ eV. The sample presented here had a conductivity σ_{DC} of 740 Sm^{-1} . The optical conductivity calculated from the Drude parameters would yield $23'000 \text{ Sm}^{-1}$, which is 31 times σ_{DC} . This could be explained with conducting grains separated by insulating grain boundaries. The Parameters for the corresponding Lorentzian were: $\hbar\omega_l = 1.1$ eV, $f_l = 1.5$ and $\hbar\gamma_l = 1.8$ eV. The carrier density n and mobility μ_{DC} that are found from the two models are compared in Table 6.7.

	$n \text{ (cm}^{-3}\text{)}$	$\mu_{DC} \text{ (cm}^2\text{V}^{-1}\text{s}^{-1}\text{)}$
Drude ($m^* = 10 m_e$)	$1.9 \cdot 10^{22}$	$2.5 \cdot 10^{-3}$
Drude ($m^* = 2.2 m_e$)	$4.1 \cdot 10^{21}$	$1.1 \cdot 10^{-2}$
Lorentzian	$2 \cdot 10^{20}$	$2.2 \cdot 10^{-1}$

Table 6.7: Comparison of charge carrier density n and mobility μ_{DC} as they were found from a Drude and a Lorentzian term, respectively. For literature values for rutile see Table 2.1. For the determination of n from the Lorentzian absorption band see Section 6.4.1. From the Drude term n was calculated according to Equation C.4 assuming an effective mass of $2.2 m_e$ [5] and $10 m_e$ [32], respectively. μ_{DC} was calculated from n and $\sigma_{DC} = 740 \text{ Sm}^{-1}$.

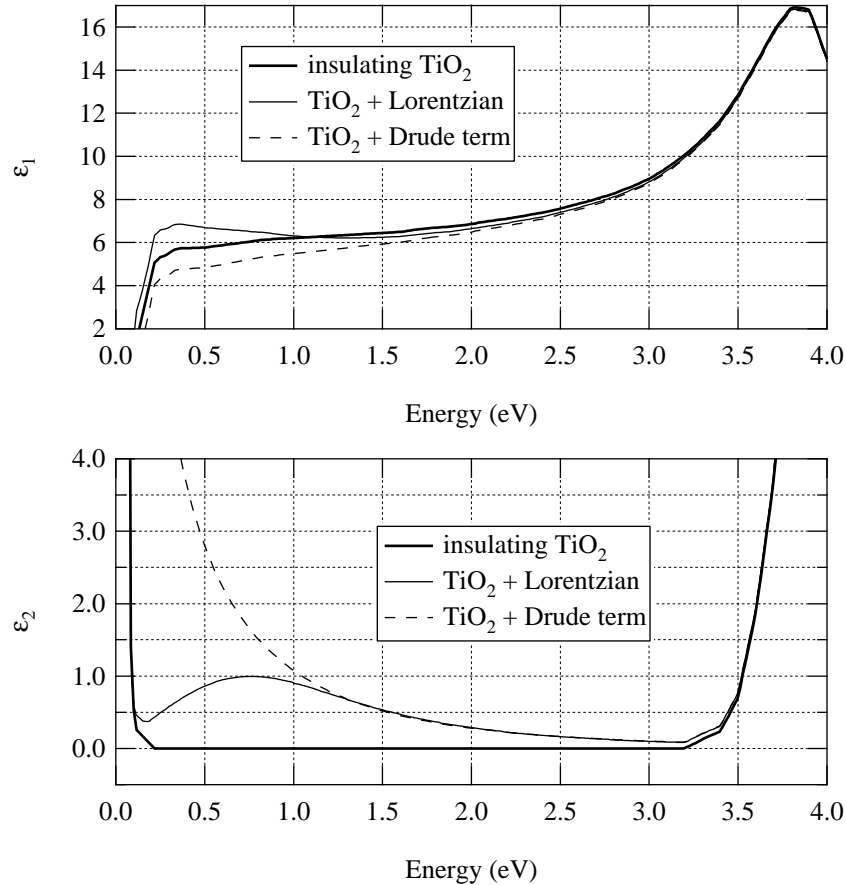


Figure 6.16: Dielectric function corresponding to the modelled spectra presented in Figure 6.14 and Figure 6.15. Only the dielectric function in the sample plane is shown.

The dielectric functions including Drude and Lorentzian terms, respectively, are shown in Figure 6.16. Around 0.1 eV ϵ_2 increases rapidly due to lattice absorption in TiO₂, at high energy it increases due to the absorption edge. In between ϵ_2 of TiO₂ is essentially zero (Figure 2.5). Here the Lorentzian appears as a wide hump. The Lorentzian contribution to ϵ_2 decreases towards lower energies whereas ϵ_2 of the Drude term continues to increase. Above 1 eV ϵ_2 of both models are very similar. The changes in ϵ_1 cause shifts of the interference fringes and influence the contrasts of the minima in transmittance.

In conclusion, effective medium approximations for polycrystalline rutile with an additional Lorentzian resulted in models that accounted well for the optical behavior of samples of Type B deposited with water vapor. In particular, the absorption in the IR region could be accounted for in this way. I shall comment on possible origins of the absorption band in the discussion at the end of the present chapter.

6.3.4.3 Optical model for samples containing anatase

As discussed in Section 6.3.3 the samples containing anatase (Type C) had different electrical properties from those devoid of anatase (Type B). Besides their high conductivity and low activation energy (Figure 6.9) a high transmittance in the infrared attracted attention (see Figure 6.17 and discussion hereafter). After having modelled the spectra with a Lorentzian in

the rutile fraction in the NIR region, a further improvement in the fit could be attained by introducing an additional, small, Drude term in the anatase component. The reason why the Drude term was restricted to the anatase phase will be given in the discussion. The values for $\hbar\omega_p$ and $\hbar\gamma_p$ were of the order of 0.3 eV. As an example the results obtained on the sample of Series (a) deposited at 20 % H₂O partial pressure are displayed in Figure 6.17. The model containing only a Lorentzian is drawn in dashed lines whereas the model with Lorentzian and Drude terms is drawn in solid lines. In the transmittance spectrum above 0.5 eV no difference can be discerned. But in the IR an improvement of the fit by introducing a Drude term in the anatase fraction ($f_A/f_R = 0.6$) with $\hbar\omega_p = 0.3$ eV and $\hbar\gamma_p = 0.4$ eV could be observed. This shows the presence of free charge carriers in the samples. For comparison the transmittance spectra in the same energy range of two samples of Type B of the same Series (a) are shown in Figure 6.18. No additional Drude term is needed in these samples to account for the absorption at low energies. The dielectric functions of the samples of Series (a) are reported in Figure 6.19.

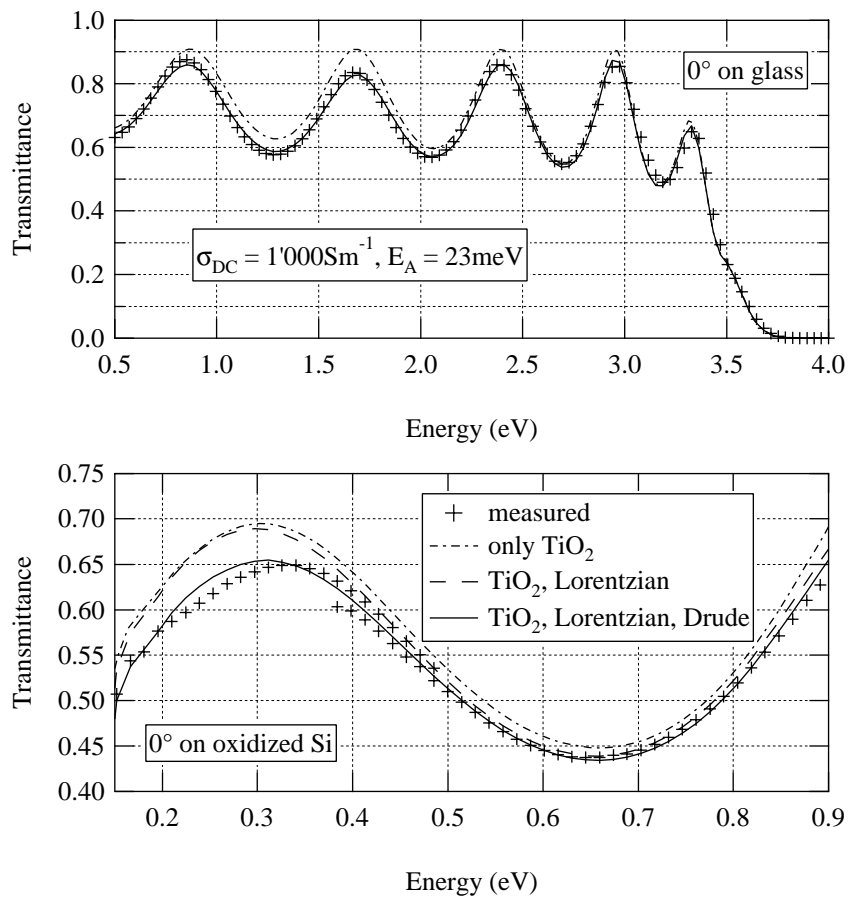


Figure 6.17: Transmittance spectra on glass (top) and on oxidized silicon substrate (bottom) of a Type C sample with stoichiometric composition TiO₂. Crosses represent measured data, lines represent modelled data with only a Lorentzian (dashed line) and an additional Drude term (solid line).

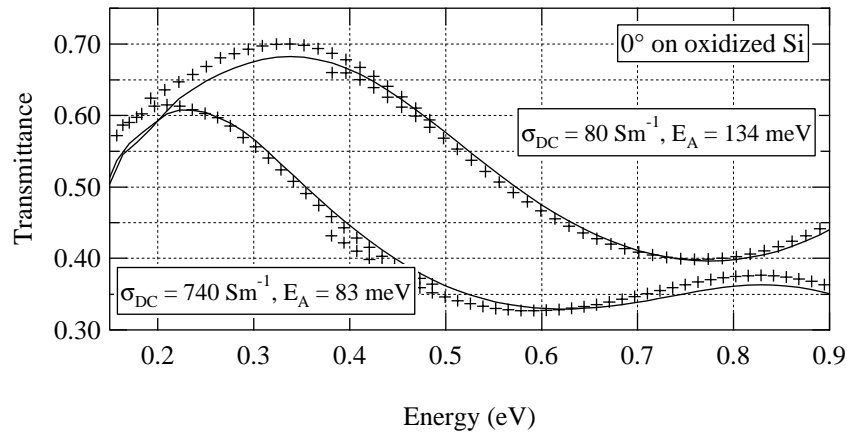


Figure 6.18: Transmittance spectra on oxidized silicon substrate of two Type B samples. Crosses represent measured data, lines represent modelled data with a Lorentzian term. No Drude term is needed to account for the absorption at low energies.

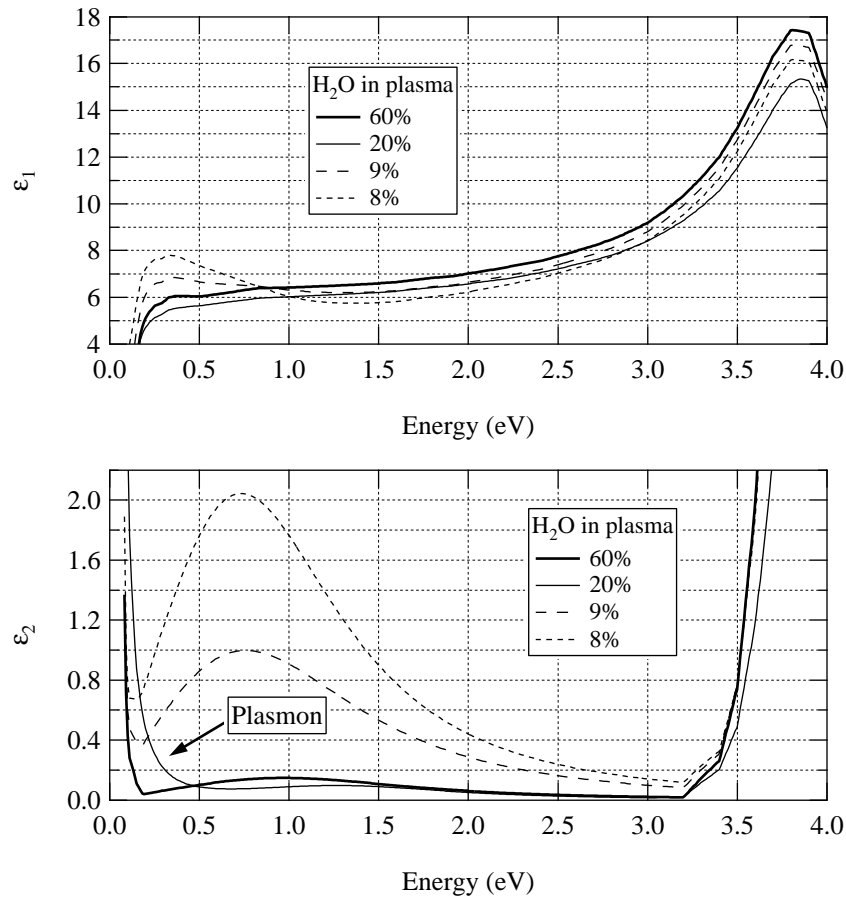


Figure 6.19: Dielectric functions corresponding to the spectra shown in Figure 6.12. The samples deposited at 8, 9 and 60 % water partial pressure were of Type B. Note the plasmon contribution in the Type C sample deposited at 20 % water partial pressure.

6.3.5 Absorption and conductivity

The transmittance spectra for the samples of Series (a) are shown in Figure 6.12. The absorption coefficient α is plotted versus photon energy in Figure 6.20. It has been calculated from the modelled extinction coefficient according to

$$\text{Equation 6.2} \quad \alpha(\omega) = \frac{2k(\omega)\omega}{c}$$

where $k(\omega)$ is the extinction coefficient as a function of the photon energy $\hbar\omega$ and c is the velocity of light in vacuum. The absorption band around 1 eV shows up clearly between the lattice absorption at low energy and the absorption edge above 3 eV. The absorption coefficient of the latter varied only slightly due to differences in anatase and void fraction in the samples. The shape of the IR absorption bands resembles the shape that has been reported by Cronemeyer et al. [33] and Bogomolov et al. [23] for reduced, gray-bluish, rutile single crystals. The observed absorption band had a width of 1 to 1.5 eV in good agreement with these publications. The maxima for the absorption coefficient were located at energies between 1 and 1.3 eV for Type B samples. This compares to what has been reported in the literature for rutile. For the Type C samples the maxima were slightly higher, at 1.5 eV. This higher value could be due to the presence of anatase in these samples. For reduced anatase single crystals broad absorption bands below 2 eV have been reported [31].

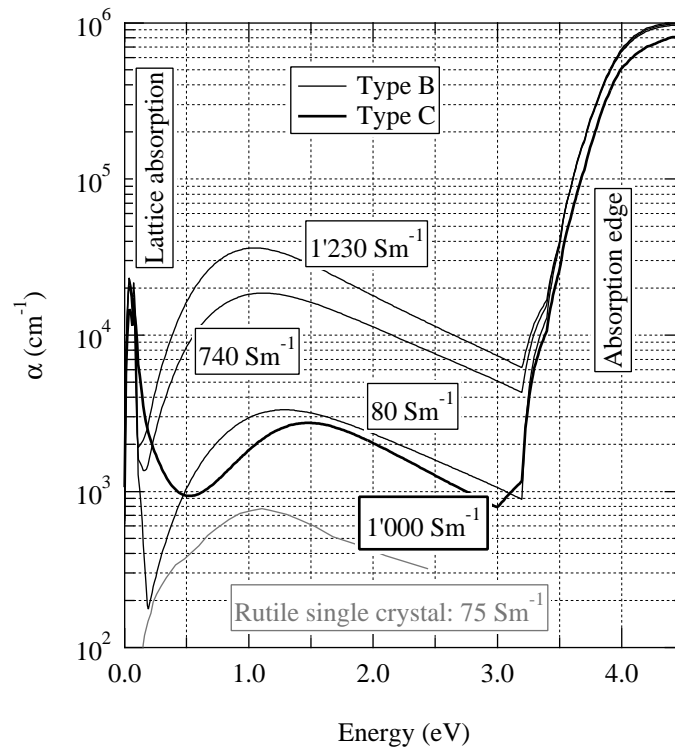


Figure 6.20: Absorption coefficient α versus photon energy for a series of films deposited with water vapor. Corresponding electrical properties are shown in Figure 6.9(a). For comparison the absorption coefficient of a reduced rutile crystal with $\sigma_{DC} = 75 \text{ Sm}^{-1}$ is shown in gray [33].

As expected for the samples of Type B the absorption increases with increasing conductivity. A Type C sample strikes by its high conductivity and low absorption (bold lines). In Figure 6.21 the maxima of the absorption bands α_{max} are put in relation to the DC conductivity at room temperature. Clearly two groups can be distinguished. They correspond to Type B (squares) and Type C (circles) samples. The former were aligned with a slope of $\alpha_{max}/\sigma_{DC} = 2'700 \Omega$, and the Type C samples were aligned with $\alpha_{max}/\sigma_{DC} = 300 \Omega$. For rutile single crystals Cronemeyer has reported $1'140 \Omega$ for α_{max}/σ_{DC} at room temperature [33]. To my knowledge, no corresponding data for anatase has been published so far.

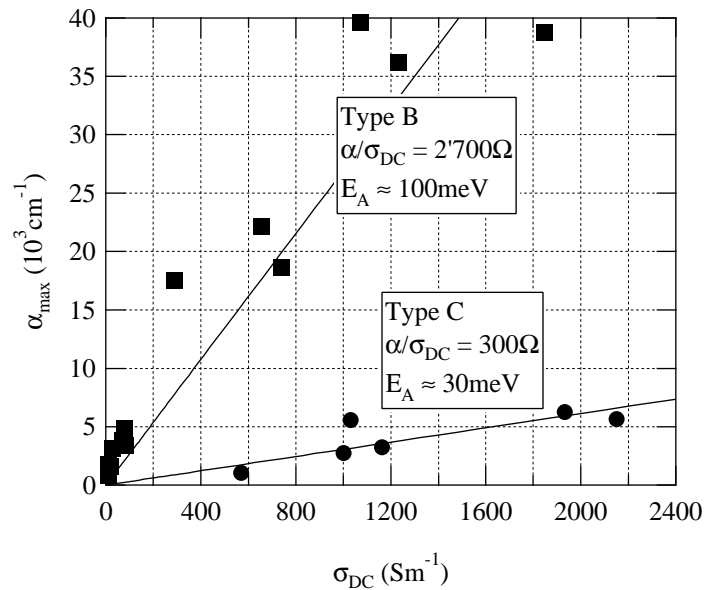


Figure 6.21: Maxima of absorption coefficient versus DC conductivity for films deposited with water vapor as reactive gas.

For the Type B samples the α_{max}/σ_{DC} ratio is roughly two times higher than the $1'140 \Omega$ reported for rutile [33]. Taking into account the polycrystalline nature of our films a lower charge carrier mobility and therefore a lower conductivity, too, would be expected. In Table 2.1 literature values for the mobility of TiO_2 are summarized. Depending on impurity concentration and crystalline structure, values between less than 0.1 and $1 \text{ cm}^2\text{V}^{-1}\text{s}^{-1}$ have been reported for rutile. This explains the higher α_{max}/σ_{DC} ratio for the Type B samples. The α_{max}/σ_{DC} ratio for the samples of Type C was significantly lower than in rutile single crystals. It is due to a different absorption process and/or the presence of charge carriers with higher mobility.

In Table 6.8 the electrical and optical properties of the samples discussed in the present chapter are put in relation with the sputtering parameters. Type B samples display a semiconducting conductivity whereas Type C samples exhibited a low activation energy for σ_{DC} , together with a metal-like Drude term in its optical properties. They are of particular interest because of the relatively low absorption in the mid-infrared in parallel with high conductivity. In contrast with samples of Type B the samples of Type C contained anatase.

H. Tang sputter-deposited anatase and rutile thin films with oxygen and reduced them by annealing in vacuum [34]. After annealing the anatase thin films showed a very flat temperature dependence and high conductivity of the order of 10^3 Sm^{-1} . The conductivity of the rutile film increased by six orders of magnitude, but it still exhibited an activation energy of 76 meV. Such electrical properties of the anatase and rutile thin films after annealing correspond to those of the as-deposited Type C and Type B films, respectively, of the present study.

Series	$\vartheta_{\text{substrate}}$ (°C)	$p(\text{H}_2\text{O})$ (%)	f_A/f_R	σ_{DC} (Sm^{-1})	E_A (meV)	α_{max} (cm^{-1})	$\hbar\omega(\alpha_{\text{max}})$ (eV)	Type
(a)	250	8	0	1'230	108	36'200	1.0	B
(a)	250	9	0	740	83	18'600	1.1	B
(a)	250	20	0.61	1'000	23	2'740	1.5	C
(a)	250	60	0	80	134	3'250	1.3	B
(b)	250	14	0	540	76	17'500	1.05	B
(b)	250	16	0.67	1'030	23	5'580	1.45	C
(b)	250	18	3.0	68	57	≈ 200	---	C
(b)	250	20	0	1'000	75	22'100	1.05	B
(c)	180	12	0	1'850	78	39'000	1	B
(c)	180	20	0.05	570	18	1'043	1.5	C
(c)	180	80	0	10	136	806	1.1	B
(c)	180	100	0	20	130	1'612	1.1	B
(c)	250	20	0	30	136	3'130	1.3	B
(c)	250	40	0	10	129	1'740	1.3	B
(c)	250	60	0	70	77	3'800	1.3	B
(c)	250	80	0	80	90	4'830	1.1	B
(d)	250	20	1.5	2'150	23	5'650	1.5	C
(d)	250	40	1.2	1'930	27	6'255	1.5	C
(d)	250	60	1.0	1'160	38	3'210	1.5	C

Table 6.8: List of samples arranged according to the deposition parameters: substrate temperature $\vartheta_{\text{substrate}}$, and water vapor partial pressure $p(\text{H}_2\text{O})$. The other parameters were constant (Table 6.1, p. 41). According to their crystalline phase composition f_A/f_R , the DC conductivity σ_{DC} , the activation energy E_A , the absorption in the IR α_{max} , and its peak position $\hbar\omega(\alpha_{\text{max}})$ the samples can be grouped in categories B and C (see text and Table 6.5).

6.4 Discussion

Extension of the investigated spectral range to lower energies demonstrated that the absorption band in the IR is a wide absorption band with a maximum near 1 eV. The immediate question which arises is the origin of this absorption. It is difficult to assign it to a clearly defined process. The samples consisted of phase mixtures of anatase, rutile and amorphous constituents. In such nanocrystalline thin films effects due to grain boundaries can occur in addition to the bulk effects known from single crystals. For instance an important substoichiometry is possible due to reduced grain boundaries whereas rutile and anatase crystalline phases are restricted to small homogeneity ranges (see Chapter 2). Such reduced grain boundaries have been proposed to provide electron donors [5].

Little has been published on the optical and electrical properties of reduced amorphous and nanocrystalline anatase and rutile thin films [35-38]. Most data have been obtained on well oxidized TiO₂ and are restricted to spectral ranges above 1.5 eV. Even for single crystalline rutile there is a controversy about the origin of the absorption in the IR [22, 39]. For anatase very little has been published on this subject [31].

The IR absorption in rutile could be due to self trapped carriers (small polarons), or to carriers bound to defects (O vacancies or Ti interstitials) and to impurities (e.g. H interstitials). Broad absorption bands in reduced rutile crystals have been reported to peak at energies between 0.75 eV [33], 0.82 eV [23], 1 eV [40], and 1.18 eV [33]. They were reported for room temperature and they all had very similar shape and width. Some authors assigned them to the ionization of donors, in particular of singly (0.75 eV) and doubly ionized (1.18 eV) oxygen vacancies [33]. In contradiction with these relatively high binding energies Breckenridge and Hosler have reported respectively 10 meV and 200 meV for the first and second ionization energies of oxygen vacancies [24]. Becker and Hosler [41] proposed the occurrence of multiband conduction in rutile with an energy gap of 50 meV between the lowest and the next higher conduction band. Bogomolov et al. assigned a broad absorption band at 0.82 eV to the hopping motion of small polarons [23, 42]. Gómez et al. [43] attributed an absorption band at 1.3 eV in a sputtered rutile thin film to polaron absorption. An absorption band in the infrared similar to the one observed in rutile has been measured in blue anatase single crystals [31]. But since the published data were restricted to photon energies above 1.5 eV one cannot say if the absorption was plasmonic or not. In anatase the carriers are less likely to be small polarons than in rutile [34] and the absorption bands have been attributed to free electrons [31]. The interpretation of the observed activation energies of σ_{DC} in terms of the nature of donor states is difficult. The concentration of charge carriers and the mobility can both be thermally activated and influence the DC conductivity dependence on temperature. Since the samples in this work have a polycrystalline structure, grain boundaries are expected to act as potential barriers and therefore reduce the effective DC mobility. Because of this the activation energy necessary for donor state ionization is probably smaller than the measured activation energy.

6.4.1 Charge carrier density

If we suppose that a single absorption mechanism is responsible for the absorption band in the IR, the absorption per charge carrier $\alpha(\hbar\omega)/n$ must be constant [40]. Cronemeyer [33] has reported $\alpha_{max}/\sigma_{DC} = 1'140 \Omega$ for rutile single crystals reduced in a H atmosphere to conductivities σ_{DC} of more than 30 Sm^{-1} . For similar samples Breckenridge and Hosler [24] have reported $\mu_{DC} = 0.5 \text{ cm}^2\text{V}^{-1}\text{s}^{-1}$ for the mobility (also see Figure 2.4). From these values and $\sigma_{DC} = n \cdot e \cdot \mu_{DC}$ the absorption per charge carrier has been determined to be $\alpha_{max}/n = 9.1 \cdot 10^{-17} \text{ cm}^2$ at room temperature. For a sputtered rutile film Gómez et al. [43] have reported an absorption band peaking at 1.3 eV with $\alpha_{max} = 6'200 \text{ cm}^{-1}$. The sample had a carrier density of $n = 7.6 \cdot 10^{18} \text{ cm}^{-3}$. This yields $\alpha_{max}/n = 8.2 \cdot 10^{-17} \text{ cm}^2$ in very good agreement with the value for crystalline rutile.

The average ratio $\alpha_{max}/\sigma_{DC} = 2'700 \Omega$ of my samples of Type B yields a mobility $\mu_{DC} \approx 0.24 \text{ cm}^2\text{V}^{-1}\text{s}^{-1}$. This is roughly half of what has been reported for rutile single crystals and corresponds well to what has been reported for polycrystalline films (Table 2.1). From the absorption per charge carrier and the electrical conductivity the charge carrier density of Type B samples was determined. It varied between 10^{19} cm^{-3} and $4 \cdot 10^{20} \text{ cm}^{-3}$.

Plasmon parameters obtained by fitting the model presented in Figure 6.17 were $\hbar\omega_p = 0.3 \pm 0.1$ eV and $\hbar\gamma_p = 0.4 \pm 0.2$ eV, corresponding to a scattering time $\tau = 1.6 \cdot 10^{-15}$ s. According to Equation C.7 the optical conductivity was $3 \cdot 10^3$ Sm⁻¹ which is close to the DC conductivity of 10^3 Sm⁻¹ measured on this sample. Assuming an effective mass equal to the mass of the electron the charge carrier density in anatase was estimated to $n = 7 \cdot 10^{19}$ cm⁻³ (Equation C.4) and the mobility to $\mu_{opt} = 3 \pm 1.5$ cm²V⁻¹s⁻¹ (Equation C.8). These values of effective mass and mobility correspond to those reported for anatase polycrystalline thin films (Table 2.1). For rutile an effective mass roughly ten times higher is often considered. Repeating the calculations leads to $\mu_{opt} \approx 30$ cm²V⁻¹s⁻¹. This mobility would be far too high for rutile (Table 2.1). The free electrons are therefore related to anatase. This is the reason why for Type C samples the Drude term was added to the anatase dielectric function only (Paragraph 6.3.4.3). Recently Jeong et al. [7] have described transparent, n-type conducting anatase thin films that were deposited by reactive sputtering with water vapor. The authors have reported a carrier density of the order of 10^{18} cm⁻³ and a mobility of 10 to 15 cm²V⁻¹s⁻¹. These values compare well with my findings for the samples containing anatase (see above). Note that their films were epitaxially stabilized. Consequently the smaller value for the mobility in my samples could be due to the polycrystalline character of the samples. Unfortunately Jeong et al. have given no detailed information about the optical properties of their samples.

6.4.2 Possible models for the IR absorption

The free carrier absorption and the very low activation energies for the anatase containing samples (Type C) can be explained by either degenerated semiconductor conductivity or by impurity band conductivity. The high mobility and low effective mass of electrons in anatase makes polaronic absorption unlikely [34]. The activation energy in the range of 30 meV observed in Type C samples could be due to scattering at grain boundaries in the polycrystalline material.

Impurity states may have been introduced during film deposition. They could include oxygen vacancies, interstitial titanium or possibly residual H atoms. With increasing impurity concentration the overlap of donor orbitals leads to the formation of a continuous impurity band [22]. The critical donor concentration n_c for the transition in anatase has been estimated to $5 \cdot 10^{18}$ cm⁻³ [34]. The carrier density in anatase of $n = 7 \cdot 10^{19}$ cm⁻³ obtained from the plasma absorption lies above this value and a metallic impurity band conduction in anatase is possible.

A similar insulator-metal transition in rutile has never been observed (see also Section 2.2). Conduction in the impurity band would only be possible by variable range hopping between localized impurity states. The width of the corresponding absorption peak might be associated with disorder in the defect centers. As an alternative the absorption band could be attributed to polaronic conduction in the rutile conduction band. Photons in the MIR range excite small polarons from self-localized states to localized states at neighboring atoms. The absorption is peaked at an energy four times the thermal activation energy E_μ for the hopping motion $E(\alpha_{max}) = 4E_\mu$ [23, 44]. Polaronic excitations will have a large vibrational component. This will broaden the absorption band [22, 45]. However, when the impurity concentration is high the simple picture of a self-trapped electron on a lattice site far from any perturbation by defect centers is not really applicable [22]. One serious objection to the polaron model is that the activation energy of σ_{DC} (~ 100 meV) is much smaller than predicted ($E_\mu \approx 250$ meV).

According to these models the optical absorption in the 1 eV range would be due to hopping conduction in rutile. In the absence of anatase the α_{max}/σ_{DC} ratio would be ideally constant. Due to the lower mobility in polycrystalline films α_{max}/σ_{DC} should be higher than the ratio observed in rutile single crystals.

6.4.3 The anatase content

The assumption that the presence of anatase played an important role in the Type C samples was confirmed by XRD measurements. In contrast to the samples of Type B, samples of Type C contained anatase and exhibited a low activation energy. In Figure 6.22 the activation energy of σ_{DC} is reported as a function of the anatase content. There was one sample with low anatase content and low E_A of 18 meV. This sample was the only Type C sample of its series and the only sample containing anatase (also see Table 6.8). Note the sample with a high anatase content but an activation energy as high as 57 meV. In spite of the large activation energy it was a Type C sample with $\alpha_{max}/\sigma_{DC} \approx 300 \Omega$. In terms of the impurity band model for anatase the relative high activation energy of 57 meV can be explained by the fact that this sample (with a $\sigma_{DC} = 68 \text{ Sm}^{-1}$) is close to the metal-insulator transition. The transition in doped compounds takes place gradually [22]. If a mobility of $\mu_{DC} = 1 \text{ cm}^2\text{V}^{-1}\text{s}^{-1}$ for anatase (see Table 2.1) is assumed, the carrier density for this sample is $4 \cdot 10^{18} \text{ cm}^{-3}$. This value corresponds to the defect concentration of $5 \cdot 10^{18} \text{ cm}^{-3}$ which is needed for the insulator-metal transition [34]. The increased activation energy could also be explained by an increased barrier at the grain boundaries corresponding to a low carrier concentration.

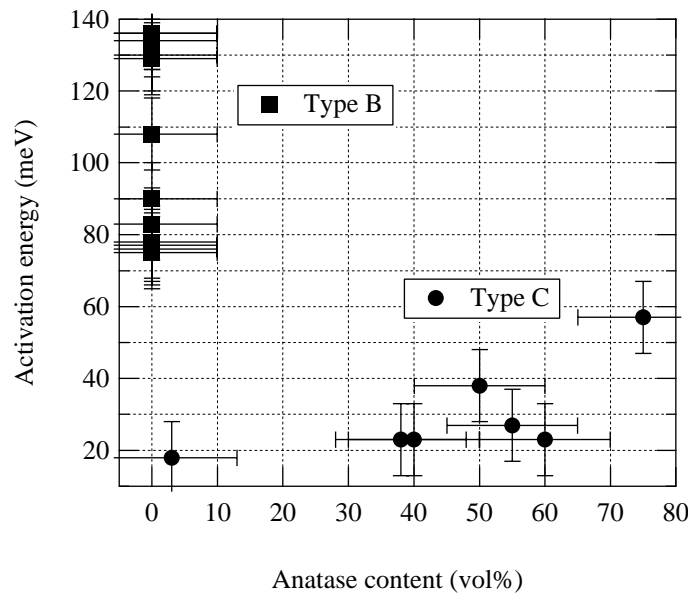


Figure 6.22: Relation between the thermal activation energy of σ_{DC} and the anatase content. Samples of Type C contained anatase and had a low activation energy. Samples of Type B did not contain any anatase and had activation energies above 70 meV.

The conditions needed to favor the formation of anatase are poorly understood [46]. The properties of reactively sputtered oxide films might depend very sensitively on minor changes in chamber geometry and process parameters, e.g. [47]. The anatase to rutile ratio in oxygen-sputtered TiO_2 thin films has been reported to depend on the substrate temperature and the reactive gas partial pressure [48, 49]. Schiller et al. have reported that for low and high oxygen partial pressures sputtered films exhibited only the rutile phase, whereas in the intermediate regime a mixture of anatase and rutile was present (Figure 6.23) [49]. In the configurations used in this work, a chemical composition close to stoichiometry seemed to be favorable for the formation of anatase (Figures 6.4 and 6.6). Anatase occurred for water vapor partial pressures in the range of 16 to 20 %, whereas at lower and higher partial pressures no anatase was detected. An exception to this finding were the films of Series (d) (Table 6.2 and Table 6.8). With the corresponding chamber configuration anatase was deposited over a wider range of parameters.

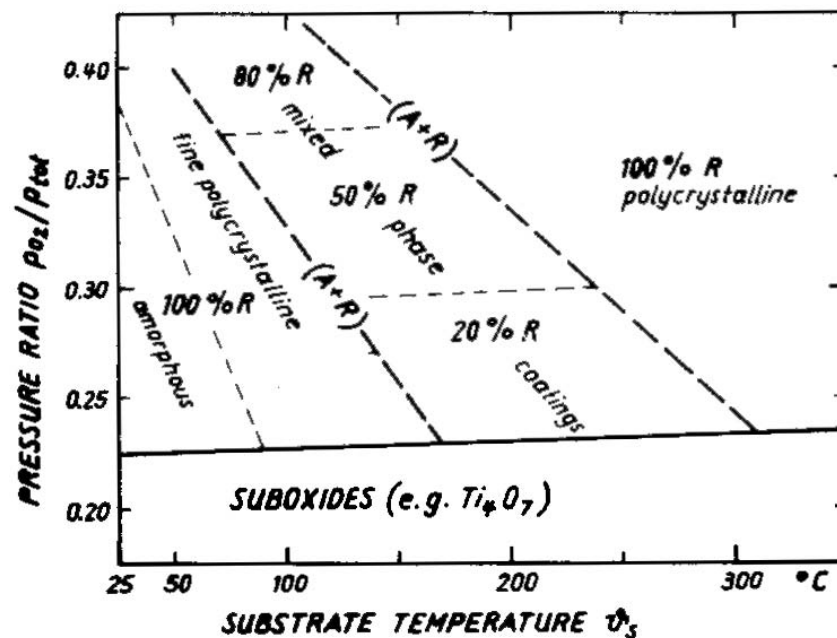


Figure 6.23: Phase composition of TiO_2 films prepared by DC reactive sputtering as a function of oxygen partial pressure in the plasma and substrate temperature [49] (see also [50]).

6.4.4 Influence of the reactive gas

To our knowledge, no as-deposited conducting and transparent rutile thin films have been reported using oxygen as reactive gas for magnetron sputtering. When the oxygen partial pressure was reduced either black conductive thin films or transparent insulating thin films were produced by Bally et al. [4, 5]. In the present study and in the work of Bally et al. [4, 5] where water vapor was used, films were transparent and conducting. An IR absorption band increased in parallel with the conductivity as $\alpha_{max}/\sigma_{DC} = 2700 \Omega$. Dissolved H has been reported to greatly affect the properties of rutile. Protons act as donors and can associate with substitutionally dissolved cations with a valence lower than 4. Therefore, H is claimed to enhance the electrical conductivity of rutile [51 and references therein].

How does hydrogen influence the properties of TiO_2 ? Two processes can be imagined, in rutile as well as in anatase. One process can be of catalytic nature and favor the formation of unsaturated titanium bonds at the grain boundaries [4-6]. As a second process, residual H in the crystal lattice could act as donors. In both cases the number of free carriers in the material is increased. Assuming interstitial hydrogen atoms as donors, the free carrier density found in the Type C samples from the Drude parameters would correspond to 10^{19} H atoms per cm^3 . This low concentration was below the detection limit of ERDA. This means that doping effects due to residual hydrogen cannot be excluded completely.

6.5 Conclusions

Thin films of slightly reduced titanium dioxide were deposited by DC reactive magnetron sputtering using oxygen or water vapor as reactive gas. The films were polycrystalline mixtures of rutile, anatase and amorphous phases with grain sizes of the order of 10 to 50 nm. The oxygen-deposited films showed a preference for the anatase phase. They were transparent and had a conductivity below 0.1 Sm^{-1} . The optical properties were modelled over a wide spectral range from the mid-IR to the UV by an anisotropic Bruggeman effective medium approximation taking voids, rutile and anatase properties into account. The values of the model parameters were close to the values determined by other characterization techniques.

The films deposited with water vapor as reactive gas consisted mostly of rutile. They showed high DC conductivity (10 to 2'000 Sm^{-1} at room temperature). With increasing temperature their conductivity increased with an activation energy between 70 and 130 meV. The charge carrier density was of the order of 10^{19} cm^{-3} and the carrier mobility was about $0.2 \text{ cm}^2 \text{ V}^{-1} \text{ s}^{-1}$. With increasing conductivity an increasingly important absorption band appeared around 1 eV. This behavior was modelled by introducing a Lorentzian term in the optical model. Models accounting for the electrical and optical properties have been proposed. The absorption band could be due to variable range hopping or to polaronic absorption in rutile.

In the water-deposited films also containing anatase a metallic conduction behavior with low activation energies (30 meV) was observed. The films showed an electrical conductivity of the order of $1'000 \text{ Sm}^{-1}$, a charge carrier density in the range of 10^{19} cm^{-3} and a carrier mobility corresponding to that of polycrystalline anatase. The films were well transparent. The IR absorption to conductivity ratio was lower than the value reported for rutile. A plasmon contribution was included in the optical model with $\hbar\omega_p$ and $\hbar\gamma_p$ of the order of 0.3 eV. Conduction band electrons in anatase were proposed as charge carriers in these samples.

Due to the lack of experimental evidence and unresolved contradictions with the theoretical models presently available the origin of the IR absorption band observed in water-deposited films remains unclear. The most important result of the present study is the demonstration of anatase-containing thin films with a high, metal-like conductivity. The high DC conductivity indicates percolation of the charge carriers.

References

1. K.-I. Onisawa, E. Nishimura, M. Ando, T. Satou, M. Takabatake, and T. Minemura, MRS 1996 Spring Meeting, Material Research Society Symposium Proceeding **424** (1997), 341.
2. E. Nishimura, M. Ando, K.-I. Onisawa, M. Takabatake, and T. Minemura, Japanese Journal of Applied Physics **35** (1996), 2788.
3. T. Nakada, Y. Ohkubo, and A. Kunioka, Japanese Journal of Applied Physics **30** (1991), 3344.
4. A.R. Bally, P. Hones, R. Sanjinés, P.E. Schmid, and F. Lévy, Surface and Coatings Technology **108-109** (1998), 166.
5. A. Bally, *Electronic properties of nano-crystalline titanium dioxide thin films*. Département de physique, Ecole polytechnique fédérale de Lausanne EPFL, Lausanne (1999).
6. O. Banakh, P.E. Schmid, R. Sanjinés, and F. Lévy, Surface and Coatings Technology **151-152** (2002), 272.
7. B.-S. Jeong, D.P. Norton, and J.D. Budai, Solid-State Electronics **47** (2003), 2275.
8. J.-M. Chappé, N. Martin, G. Terwagne, J. Lintymer, J. Gavaille, and J. Takadoum, Thin Solid Films **440** (2003), 66.
9. U. Diebold, Surface Science Reports **48** (2003), 53.
10. A.T. Paxton and L. Thien-Nga, Phys. Rev. B **57** (1998), 1579.
11. S. Kadlec, J. Musil, and J. Vyskocil, Vacuum **37** (1987), 729.
12. B. Chapman, *Glow discharge processes: Sputtering and plasma etching*. John Wiley & Sons, New York (1980).
13. *PDF-database*. JCPDS, International centre for diffraction data (ICDD), 1601 Park Lane, Swarthmore, PA 19081, USA.
14. J.P. Borgogno, B. Lazarides, and E. Pelletier, Applied Optics **21** (1982), 4020.
15. *CRC Handbook of chemistry and physics*. 67th ed., CRC Inc., Boca Raton (1986).
16. V. Holý, U. Pietsch, and T. Baumbach, *High-Resolution X-Ray Scattering from Thin Films and Multilayers*. Springer, Berlin (1999).
17. J. Dailant and A. Gibaud, *X-ray and neutron reflectivity: principles and applications*. 1st ed., Springer, Berlin (1999).
18. M. Laube, F. Rauch, C. Ottermann, O. Anderson, and K. Bange, Nuclear Instruments and Methods in Physics Research B **113** (1996), 288.
19. Rusli, K. Chew, S.F. Yoon, H.K. Chan, C.F. Ng, Q. Zhang, and J. Ahn, International Journal of Modern Physics B **16** (2002), 1072.
20. M.J. Madou, *Fundamentals of Microfabrication*. 1st ed., CRC Press, Boca Raton (1997).
21. S.M. Sze, *Physics of semiconductor devices*. John Wiley & Sons, New York (1981).
22. P.A. Cox, *Transition Metal Oxides*. 1st ed., Clarendon press, Oxford (1992).
23. V.N. Bogomolov, E.K. Kudinov, D.N. Mirlin, and Y.A. Firsov, Soviet Physics - Solid State **9** (1968), 1630.
24. R.G. Breckenridge and W.R. Hosler, Phys. Rev. **91** (1953), 793.
25. G.E. Jellison, Jr., Thin Solid Films **234** (1993), 416.
26. D. Mergel, Thin Solid Films **397** (2001), 216.
27. S. Adachi, *Optical properties of crystalline and amorphous semiconductors: Materials and fundamental principles*. Kluwer Academic Publishers, Boston (1999).
28. F. Urbach, Phys. Rev. **92** (1953), 1324.
29. H. Tang, F. Lévy, H. Berger, and P.E. Schmid, Phys. Rev. B **52** (1995), 7771.
30. N. Hosaka, T. Sekiya, and S. Kurita, Journal of Luminescence **72-74** (1997), 874.
31. T. Sekiya, K. Ichimura, M. Igarashi, and S. Kurita, Journal of Physics and Chemistry of Solids **61** (2000), 1237.
32. G.A. Acket and J. Volger, Physica **32** (1966), 1680.
33. D.C. Cronemeyer, Phys. Rev. **113** (1959), 1222.
34. H. Tang, *Electronic properties of anatase TiO₂ investigated by electrical and optical measurements on single crystals and thin films*. Département de physique, Ecole polytechnique fédérale de Lausanne EPFL, Lausanne (1994).

35. K. Postava, M. Aoyama, T. Yamaguchi, and H. Oda, *Applied Surface Science* **175-176** (2001), 276.
36. T.M.R. Viseu and M.I.C. Ferreira, *Vacuum* **52** (1999), 115.
37. T.M.R. Viseu, B. Almeida, M. Stchakovsky, B. Drevillon, M.I.C. Ferreira, and J.B. Sousa, *Thin Solid Films* **401** (2001), 216.
38. S. Tanemura, L. Miao, P. Jin, K. Kaneko, A. Terai, and N. Nabatova-Gabain, *Applied Surface Science* **212-213** (2003), 654.
39. N. Tsuda, K. Nasu, A. Fujimori, and K. Siratori, *Electronic conduction in oxides*. 2nd ed., Springer, Berlin, Heidelberg, New York (2001).
40. R.D. Carnahan and J.O. Brittain, *Journal of the American Ceramic Society* **48** (1965), 365.
41. J.H. Becker and W.R. Hosler, *Phys. Rev. A* **137** (1965), 1872.
42. V.N. Bogomolov, Y.A. Firsov, E.K. Kudinov, and D.N. Mirlin, *Physica Status Solidi* **35** (1969), 555.
43. M.M. Gómez, N. Beermann, J. Lu, E. Olsson, A. Hagfeldt, G.A. Niklasson, and C.G. Granqvist, *Solar Energy Materials and Solar Cells* **76** (2003), 37.
44. C.A. Kuntscher, D. van der Marel, M. Dressel, F. Lichtenberg, and J. Mannhart, *Phys. Rev. B* **67** (2003), 35105.
45. D. Emin, *Phys. Rev. B* **48** (1993), 13691.
46. F. Bregani, C. Casale, L.E. Depero, I. Natali-Sora, D. Robba, L. Sangaletti, and G.P. Toledo, *Sensors and Actuators B* **31** (1996), 25.
47. J. Geng, *Spectral selective coatings based on aluminum oxide and related materials*. Philosophisch-Naturwissenschaftliche Fakultät, Universität Basel, Basel (2000).
48. M.H. Suhail, G.M. Rao, and S. Mohan, *J. Appl. Phys.* **71** (1992), 1421.
49. S. Schiller, G. Beister, W. Sieber, G. Schirmer, and E. Hacker, *Thin Solid Films* **83** (1981), 239.
50. P. Löbl, M. Huppertz, and D. Mergel, *Thin Solid Films* **251** (1994), 72.
51. P. Kofstad, *Nonstoichiometry, diffusion, and electrical conductivity in binary metal oxides*. John Wiley & Sons, Inc., New York (1983).

Chapter 7 Triple layer structures of TiO₂

Important modifications of the film properties of titanium oxide thin films have been reported when oxygen was replaced by water vapor as reactive gas in the sputtering process [1-4]. The role of the water vapor is not well understood yet. Water results in the presence of OH and H radicals in the discharge. These radicals seem to play a catalytic role during the deposition by preventing the full oxidation of Ti. They favor the presence of unsaturated titanium bonds at the grain boundaries. To have a simple representation of the processes that take place at the reduced grain surfaces of TiO₂ the Ti/TiO₂ interface was investigated by using a triple layer structure of a titanium layer in between two dioxide layers.

7.1 Preparation of TiO₂ films with Ti-rich interlayers using O₂ as reactive gas

Films were deposited with titanium layers intercalated in between two titanium dioxide layers. The bottom and top oxide layers were deposited as to have the same thickness (50 nm to 210 nm). The nominal thicknesses of titanium interlayers varied between 1 and 17 nm. Oxygen was used as reactive gas in all cases. The deposition parameters, such as substrate temperature (250 °C), target to substrate distance (9 cm) and power supply (300 mA DC) were the same as in Chapter 6. They are given in more detail in Chapter 3. Substrates were halves of 2 inch single-side polished Si wafers and 21 mm × 25 mm microscope glass slides. The substrate properties are listed in Table 3.1.

The growth rate for TiO₂ (0.36 Ås⁻¹) and Ti (1.43 Ås⁻¹) was determined by a quartz crystal microbalance (QMB) and profilometry on reference samples deposited in the same conditions. Usually the metals have a higher sputtering yield and therefore exhibit a higher deposition rate [5]. Sputtering times varied between 25 and 100 minutes for the oxide and 7 to 120 seconds for the titanium layers, respectively. A single Ti target was used. For depositing the Ti layer the O₂ gas supply was turned off. To allow the target changing its surface oxidation state and stabilize in the new situation shutters in front of the target and the substrate were kept closed during 5 minutes after turning on or off the oxygen gas supply.

7.2 Results

The structural, chemical, electrical and optical properties of the samples were characterized by the methods described in Chapter 4. In the figures and in the discussion the samples are referred to by their structure. The notation e.g. 53nm/9nm/53nm lists the layer thicknesses from the bottom to the top of the sample.

7.2.1 Morphology and crystalline structure

7.2.1.1 Stratified sample structure

If it is not indicated differently, in this chapter layer thicknesses are given according to the deposition parameters. The total film thicknesses of the triple-layered stacks were controlled by profilometry. It corresponded within 10 % to the sum of the nominal thicknesses of the sublayers. The thicknesses of the individual layers will appear as fitting parameters in optical and XRR analyses. Therefore, TEM analyses on the cross section of the samples have been performed (see below).

7.2.1.2 Crystallinity dependence on interlayer thickness

Grazing incidence X-ray diffraction patterns were measured on silicon substrates. In Figure 7.1 measurements on samples with increasing interlayer thickness are presented. The peak positions and relative intensities are marked according to the JCPDS powder diffraction pattern database [6] by dashed and dotted lines. Rutile, anatase and amorphous phases were present in all samples. No metallic titanium or titanium monoxide peaks could be distinguished even for the thickest intermediate titanium layers. This indicates that the Ti-rich layers were amorphous or consisted of very small crystallites. Correspondingly for samples with a thicker metal layer the amorphous volume fraction f_{am} increased (Figure 7.2).

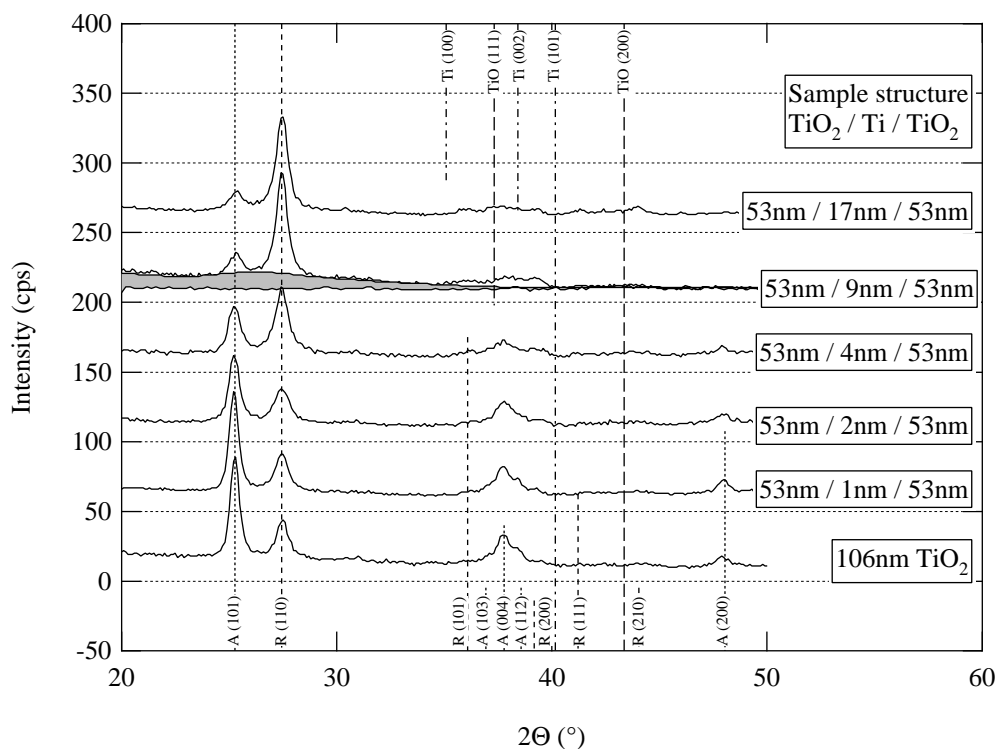


Figure 7.1: Grazing incidence X-ray diffraction pattern of triple layered samples with different metal layer thicknesses measured on Si substrates. The vertical lines mark the peak positions and intensities⁷ of rutile (dashed, labeled R), anatase (dotted, labeled A), titanium (dash-dot), and TiO (long dashes) as given in [6]. Patterns were offset vertically by multiples of 50 cps for clarity. The contribution of the amorphous fraction is shown in gray, as an example.

⁷ PDF files: Rutile: 21-1276, Anatase: 21-1272, TiO: 08-0117, Ti: 44-1294 [6].

With increasing metal layer thickness the rutile to anatase ratio changed. The anatase content f_A is shown in Figure 7.2. A maximum of 30 % of anatase was observed in samples without interlayer. It decreased with increasing interlayer thickness and saturated at a low value for thicker titanium layers. The presence of the metallic layer hindered the formation of anatase. This can also be seen in the rapid decrease of the anatase crystallite size (Figure 7.3). The maximum crystallite size was found in the reference samples without interlayer. It was 18 nm for rutile and 32 nm for anatase. The crystallite size of anatase decreased over the whole range of samples, whereas for rutile the crystallite size attained a minimum value of 14 nm for an interlayer of 4 nm thickness.

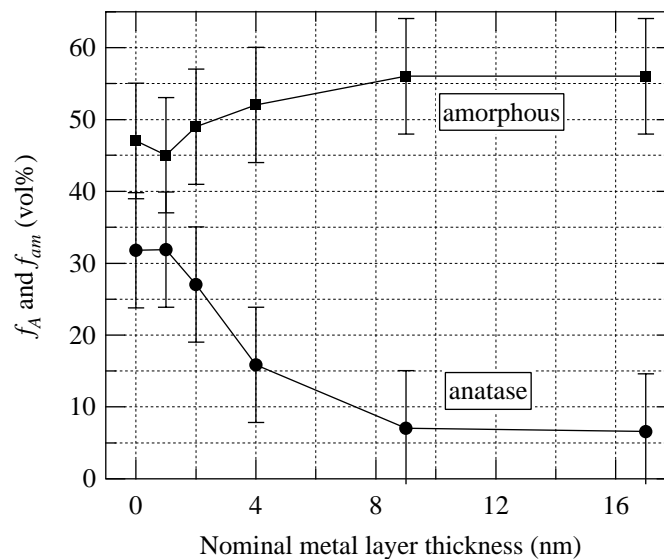


Figure 7.2: Anatase and amorphous fractions (f_A and f_{am}) determined from the XRD patterns (Paragraph 4.1.2.1). The lines are a guide to the eye.

There was a correlation between the thickness of the titanium-rich layer and the crystalline properties of the oxide layers. The observed behavior in XRD corresponds to a combination of the properties of both oxide and the Ti-rich layers in the stack. Changes in crystallinity in the upper oxide layer can be attributed to a changing substrate (the Ti-rich layer) on which it is grown. Changes in the lower oxide layer can be the result of diffusion of titanium into the intercolumnar voids or the bulk of the crystallites (see below). Changes in phase composition and crystallite size were rapid for interlayer thicknesses up to 4 nm and tended to saturate for thicker titanium-rich layers. This indicates that from an equivalent of 9 nm of titanium the titanium-rich layer was continuous and covered the lower oxide layer. Ti would no longer diffuse into the underlying oxide.

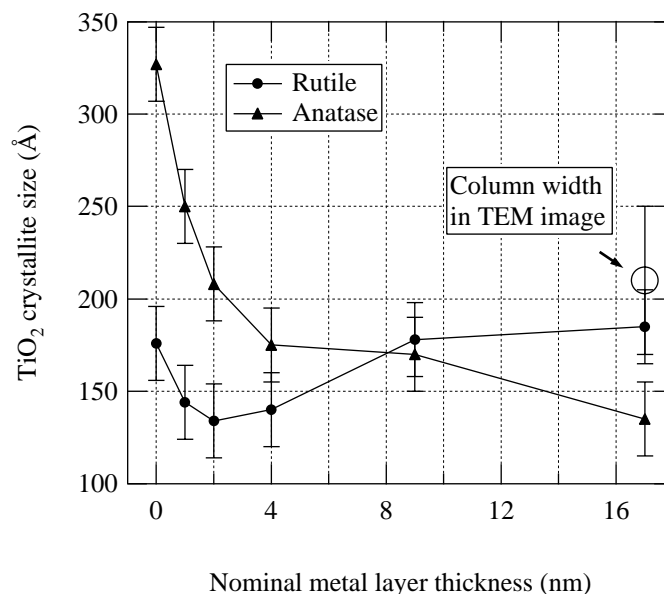


Figure 7.3: Crystallite size of anatase and rutile phases as determined from the XRD peak widths in function of the metal interlayer thickness. The column width estimated from TEM pictures is reported, too. The lines are a guide to the eye.

7.2.1.3 TEM cross section of a triple layer structure

Cross section observations by TEM and EELS yield important information about the morphology and chemical composition of every layer in a stratified sample. Corresponding results are discussed in the present paragraph and in Paragraph 7.2.2.2. Two cross section specimens suitable for transmission electron microscopy were prepared from a 53nm/17nm/53nm sample. One of the specimens was mechanically polished into the shape of a wedge. This had the advantage that modifications by ion bombardment were avoided but it had the inconvenience that the area thin enough for electron transmission was limited. The second specimen was mechanically polished and ion milled (Section 4.1.7). Bright field, dark field (DF) and high resolution (HR) pictures were taken at magnifications between 80'000 and 335'000. The observations on the two specimens compared well.

The left part of Figure 7.4 shows an overview image of the cross section. The stratified structure can clearly be distinguished. The layer thicknesses have been measured and are reported in Table 7.1. The total film thickness compared well to the one expected from the sputtering parameters and the thickness determined by profilometry. The titanium-rich interlayer (11 nm) was thinner than the nominal thickness (17 nm). The lower and upper oxide layers did not have the same thickness (50 and 63 nm). They should both have been 53 nm according to the deposition parameters. The amorphous SiO₂ layer between the substrate and the titanium oxide was 8 nm thick. This was thicker than the 1.8 nm obtained by ellipsometry on a bare substrate. The surface roughness was estimated to 4 nm. The interface roughness between the oxide layers and the metallic interlayer was 3 nm. Interfaces between the bulk silicon and the silicon oxide layer as well between the silicon oxide and the lower TiO₂ had a roughness of less than 1 nm⁸. Grain boundaries were clearly visible in the oxide

⁸ The roughness between SiO₂ and TiO₂ was 0.3 nm by XRR (see Paragraph 6.3.2.4).

layers. Both bottom and top layers exhibited columnar growth. The width of the columns in the oxide layers was estimated to 21 ± 4 nm.

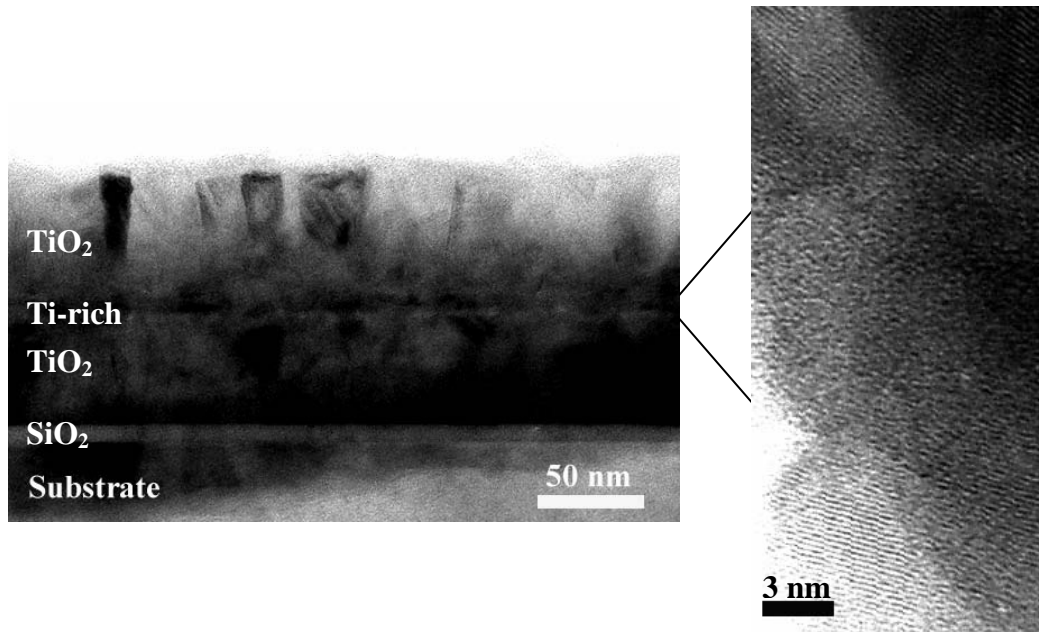


Figure 7.4: TEM observation on the cross section of a 53nm/17nm/53nm triple layered sample. The apparent surface roughness is due to the preparation of specimen. Some glue can be seen on top of the upper oxide layer. The right side shows a HR image of the amorphous, titanium-rich layer with crystallized titanium dioxide below and above.

The high resolution (HR) image on the right of Figure 7.4 shows details of the interlayer and parts of the oxide layers. In the Ti-rich layer no crystalline structure was observed in high resolution. This confirms the XRD results that the interlayer was amorphous or consisted of very small crystallites (smaller than about 3 nm). As could be observed in HR pictures crystalline growth in the lower oxide layer started immediately on the silicon oxide layer. No amorphous TiO₂ layer at the beginning of the film growth was discerned. The beginning of crystallization of the upper oxide layer was less clear, since the contrast towards the amorphous interlayer was bad in HR.

Layer	Nominal t (nm)	TEM t (nm)	RBS/ERDA		Opt. model t (nm)
			ρ (g/cm ³)	x in TiO _x	
Surface roughness	---	3 - 4	---	---	3
Upper dioxide layer	53	63 ± 2	3.2	1.98	62
Interface roughness	---	~3	---	---	2
Ti-rich interlayer	17	11 ± 2	$4.7^{(i)}$	1.26	10
Interface roughness	---	~3	---	---	2
Lower dioxide layer	53	50 ± 1	3.5	1.89	49
SiO ₂	$1.8^{(ii)}$	8 ± 1	2.2	---	8
Total film	123 $126^{(iii)}$	124 ± 2	---	---	125

Table 7.1: Summary of properties of a 53nm/17nm/53nm sample obtained by profilometry, electron microscopy and RBS/ERDA. The last column contains the values used in the optical model (Figure 7.13). Parameters are thickness t (nm), density ρ (g/cm³). (i) Calculated assuming 14 nm for the layer thickness. (ii) Measured by ellipsometry on the bare substrate. (iii) Measured by profilometry.

7.2.1.4 X-ray reflectivity of a triple layer structure

X-ray reflectivity allows non-destructive measurements of the layer thicknesses and interface roughnesses of stratified samples. An X-ray reflection pattern obtained on a 53nm/17nm/53nm sample is reported in Figure 7.5. The complex interference fringe structure is due to multiple reflections in the different layers contributing to the signal. The different frequencies correspond to the layer thicknesses. Below the triple layered film the silicon substrate and its native oxide layer contributed to the general shape of the signal. The nice fringes between 0.4 and 0.6 and between 0.8 and 1.0 degrees have a spacing corresponding to the oxide layers. The thickness of the titanium-rich layer corresponds to roughly 0.4 degrees between two interference fringes. It causes a damping around 0.7 and 1.1 degrees. In addition, the fringes were damped quickly, due to important interface roughness (see Table 7.1 and Appendix E.2.3).

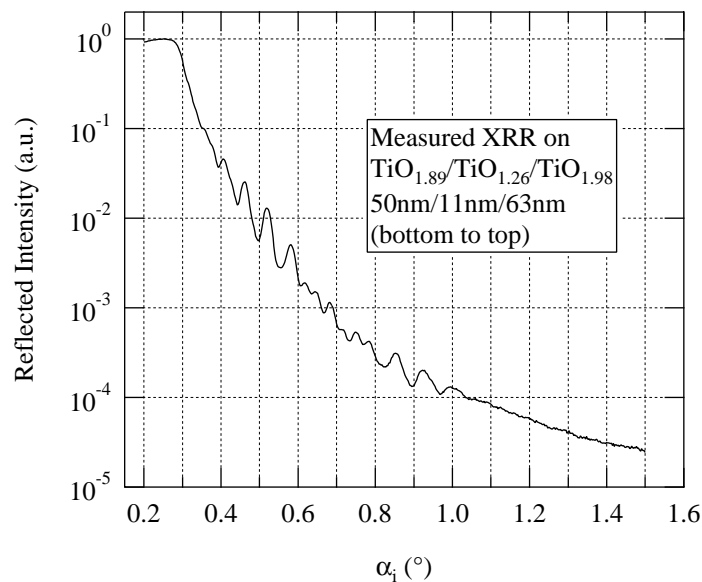


Figure 7.5: Reflected X-ray intensity as a function of the angle of incidence.

For detailed interpretation of these data the reflectivity behavior needed to be modelled. The approach presented in Paragraph 6.3.2.4 could not be used in the case of samples consisting of more than one layer. For the models a structure of distinct homogeneous layers was assumed. Interface and surface roughness were taken into account as a Gaussian distributed variation in layer thicknesses. The input parameters for the fitting process for the roughnesses and layer thicknesses were estimated from the TEM observation (Table 7.1). For the chemical composition and density of every layer the start parameters were estimated from the RBS and EELS measurements (Equation 4.5).

As a consequence of the roughness, the interference fringes were strongly damped. Thus the information contained in the XRR data was limited and correlation between parameters occurred. Furthermore, since titanium is a relatively light metal the difference in the densities between the layers was small, and thus, the contrasts seen by XRR were low. For these reasons electron density information could not be extracted from the XRR curves.

7.2.2 Chemical composition

7.2.2.1 RBS depth profile

RBS and ERDA analyses were performed to investigate the chemical composition of the different layers. The measured and modelled spectra obtained on a 53nm/17nm/53nm sample on silicon substrate are represented in Figure 7.6. The titanium contribution can clearly be distinguished at low energy loss. Superposed on the silicon signal of the substrate, the oxygen component appears at higher energy loss. The hump in the titanium and the depression in the oxygen signal, respectively, correspond to the titanium-rich layer.

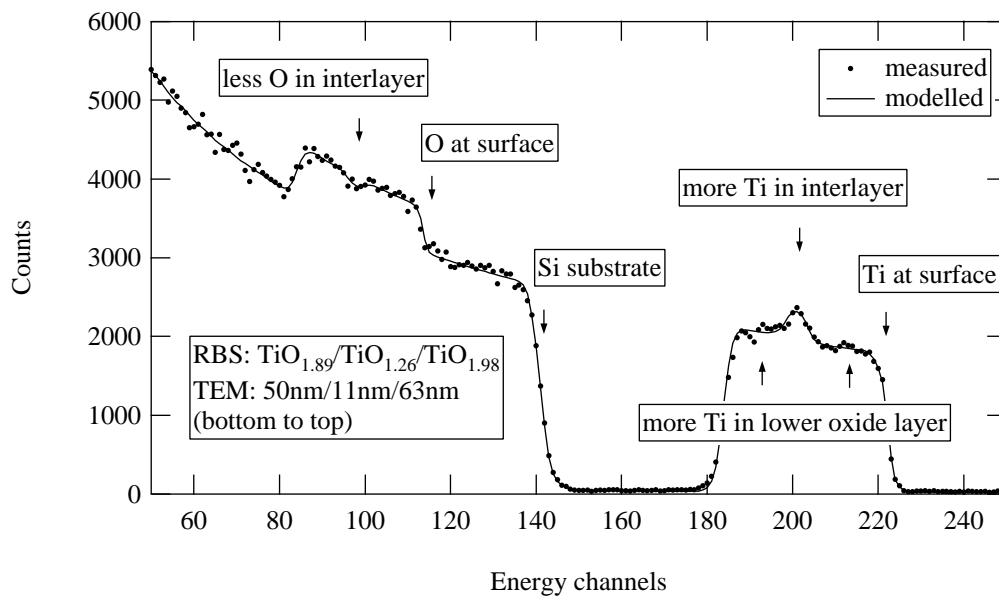


Figure 7.6: Measured (points) and modelled (lines) 2 MeV He⁺ RBS spectrum of a 53nm/17nm/53nm sample for a grazing incidence angle of 76° between ion beam and the sample normal. The scattering angle was 150°. The lower TiO₂ layer was enriched in Ti by grain boundary diffusion.

The modelled spectrum shown in Figure 7.6 was obtained by dividing the film into four layers, namely: the lower and upper oxide layers with a Ti-rich interlayer and a contaminated surface layer. The corresponding depth profile is presented in Figure 7.7. Hydrogen was observed by ERDA in an 8 nm thick surface layer. This is commonly observed on thin film samples (see also Section 6.3.1). It was attributed to water and hydrocarbon contaminations at the surface. RBS was not the right technique to decide if the change in concentration was discrete as in the model or whether it was gradual. The chemical composition x in TiO _{x} was determined to be 1.89 for the lower and 1.98 for the upper oxide layer, respectively. The increased titanium content in the lower oxide layer was due to a diffusion of titanium into the spaces between the columns. Grain boundaries are known to be preferred ion diffusion paths in TiO₂ [7, 8]. With $x = 1.26$ the intermediate layer had a lower oxygen content than the oxide layers. In addition to TiO₂ and pure Ti, the oxygen-titanium phase diagram (Figure 2.3) shows many phases that are stable at room temperature. The amorphous morphology of the interlayer could be due to a mixture of several substoichiometric phases.

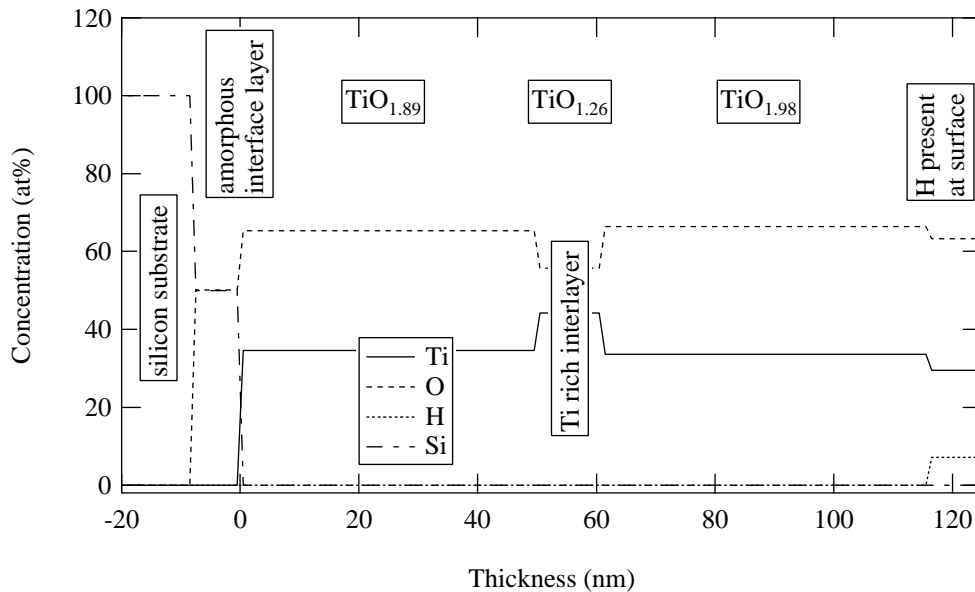


Figure 7.7: Chemical depth profile of a 53nm/17nm/53nm sample obtained from RBS and TEM measurements. Corresponding values are listed in Table 7.1.

The density of every layer was evaluated according to Equation 4.5 and is listed in Table 7.1. Compared to bulk rutile and anatase, density values of 3.5 g/cm^{-3} for the lower and 3.2 g/cm^{-3} for the upper oxide layers were low. For the determination of the density of the intercalated layer a thickness of 14 nm was assumed. This corresponds to an intermediate thickness halfway in between the nominal value of 17 nm and the layer thickness measured from TEM (11 nm). The density of 4.7 g/cm^{-3} obtained in this way compares to 4.52 g/cm^{-3} for Ti bulk and 4.93 g/cm^{-3} for TiO bulk [10].

7.2.2.2 EELS chemical composition on the cross section

A specimen prepared for the TEM observation was used for an EELS investigation on the film cross section. This technique has the important advantage that the sample cross section can be probed at any point with a local resolution of about 1.5 nm. EELS spectra were acquired at several points on the oxide layers, on the interfaces and in the middle of the Ti-rich interlayer. The results are presented in Figure 7.8 and put in relation with RBS results. Since the specimen was relatively thick for this kind of measurement the oxygen and titanium signals were low compared to the background and correspondingly precision was limited. The chemical composition in the oxide layers is close to stoichiometric TiO₂. There was some oxygen present in the intercalated Ti-rich layer but the chemical composition was still lower than that of monoxide. The change of the chemical composition between the layers was more gradual than could be accounted for by RBS. This was true for both lower and upper interfaces. Since no standard sample has been used the values of chemical composition are of relative character and the absolute values need to be taken with caution.

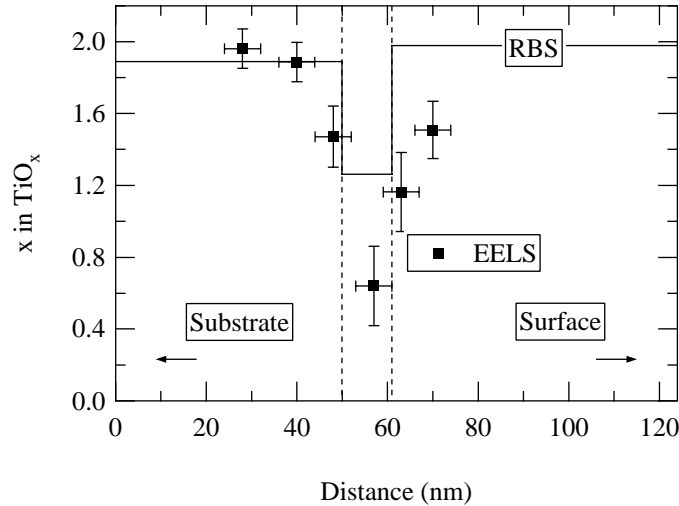


Figure 7.8: Chemical composition measured by EELS (squares) and RBS (lines). The EELS measurements were performed on a TEM cross section specimen prepared of a 53nm/17nm/53nm sample. The substrate was on the left, the interfaces between the oxide and the Ti-rich layer are marked with dashed lines.

7.2.3 Electrical properties

The evolution of the resistance of the samples as a function of the metal layer thickness can give indications about the degree of oxidation and percolation of the intercalated titanium. Ideally the in-plane resistance R_{film} would decrease linearly with the metal layer thickness. It was measured in the van der Pauw geometry on glass substrates. Because of the high resistance of the oxide layers the current was assumed to pass through the titanium-rich layer only. Since the thickness t_{metal} of the titanium-rich layer was not well known for all samples the discussion hereafter will be based on the measured conductance R_{film}^{-1} . Figure 7.9 shows the conductance of samples with varying metal layer thicknesses as a function of temperature. Samples with a nominal Ti layer thickness of less than 4 nm were too resistive to be measured in this configuration ($R_{film} \geq 10^8 \Omega$). The steep increase of conductance at RT was not a linear function of to the increase in the nominal titanium layer thickness. When the nominal Ti thickness was doubled from 2 to 4 nm, 4 to 9 nm, and 9 to 17 nm the conductance increased by a factor of $>10^3$, 35, and 7, respectively. The saturation in the increase in conductance indicates that the percolation threshold is attained and the oxidation of the Ti-rich layer at the interfaces becomes less important.

With increasing temperature the conductance increased. The activation energy at room temperature decreased from 95 meV for nominally 4 nm titanium to 11 meV for 17 nm titanium. For thin titanium layers the activation energy decreased with increasing temperature whereas for 17 nm titanium the activation energy was well defined over the investigated temperature range. A negative thermal coefficient of resistivity has been reported for titanium monoxide by Banakh et al. [3]. Thus a reduced activation energy might indicate the presence of titanium monoxide.

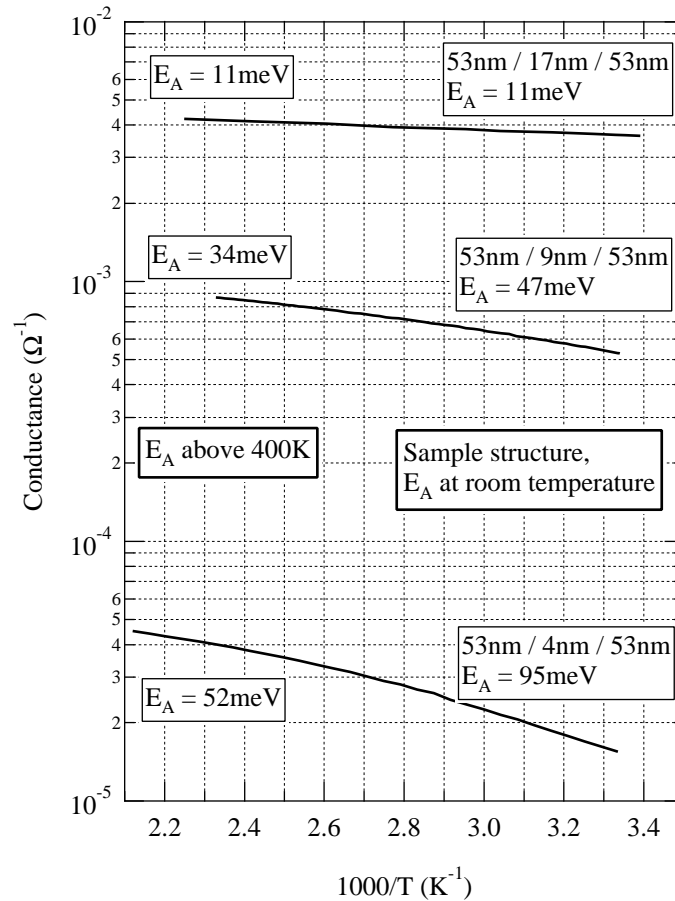


Figure 7.9: In-plane conductance of TiO₂/Ti/TiO₂ films as a function of temperature T . The oxide and metal layer thicknesses and the activation energies at low and high temperatures are indicated.

In Figure 7.10 the conductance at room temperature is compared with the conductance of continuous metal layers of variable thickness. These layers were assumed to consist of either titanium or titanium monoxide. The calculated conductances appear as diagonal lines in the figure. The measured conductances for three samples with different Ti layers are represented as horizontal lines. A titanium-rich layer of 11 nm was observed by TEM for a sample with the 53nm/17nm/53nm structure. This corresponds to a loss of the equivalent of 6 nm of titanium to oxidation and diffusion. The loss is indicated in the figure by an arrow. In this sample the conductivity of the titanium-rich layer is close to the conductivity of TiO. Assuming the same loss of Ti (6 nm, arrow in the figure) in a 53nm/9nm/53nm sample the corresponding titanium-rich layer is slightly more resistive than TiO and/or is not continuous. For the samples with nominally 4 nm of titanium the titanium-rich layer is too resistive to be continuous. This implies that the interface roughness must be close to 4 nm (also see Table 7.1 on p. 75).

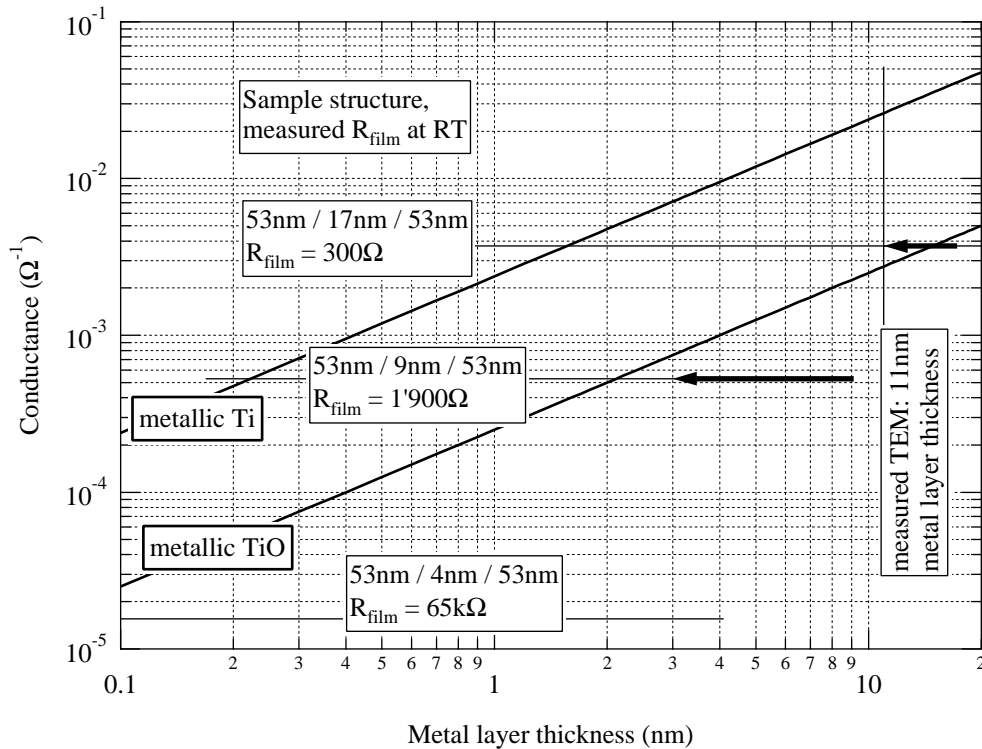


Figure 7.10: Measured conductance of triple layers at room temperature (horizontal lines) in comparison with the conductance of Ti and TiO layers of variable thickness (diagonal lines). The calculation was based on $\sigma_{DC}(\text{Ti}) = 2.38 \cdot 10^6 \text{ Sm}^{-1}$ [10] and $\sigma_{DC}(\text{TiO}) = 2.5 \cdot 10^5 \text{ Sm}^{-1}$ [1, 3]. The measured thickness of the titanium-rich layer in a 53nm/17nm/53nm sample is indicated at 11 nm (vertical line). Arrows mark an estimated loss of 6 nm titanium equivalent between the nominal and real metal layer thickness.

7.2.4 Optical properties

Samples with comparable TiO₂ layer thicknesses changed continuously from transparent to dark brownish with increasing metal layer thickness. The films deposited on glass substrates were measured in a transmission configuration at normal incidence. The samples on silicon substrates were characterized by ellipsometry and spectrophotometry in reflection at 30° incidence. Figure 7.11 shows the transmittance spectra of a series of triple layered samples with varied metal layer thickness but comparable oxide layer thicknesses. For a metal layer thickness of less than 4 nm the transmittance spectra changed little compared to TiO₂. This was also true for reflectance and ellipsometry spectra (not shown). For the sake of clarity in Figure 7.11, the corresponding spectra have been omitted. For 9 and 17 nm interlayer thickness a decrease in transmittance over the whole width of the spectrum can be seen clearly. The absorption edge appears unchanged (Figure 7.12).

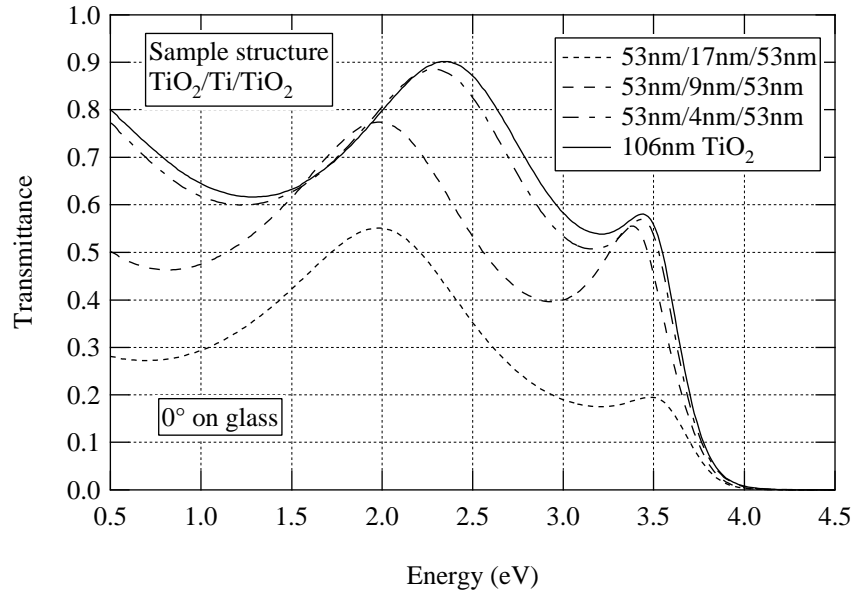


Figure 7.11: Transmittance spectra of TiO₂/Ti/TiO₂ films on glass substrates with varying metal layer thickness.

7.2.4.1 Modelling of the optical properties

The optical response of the triple layered samples is sensitive not only to the layer thicknesses but also to the interface roughnesses and the properties of the layers. Thus from a model accounting for the optical properties important indications about the morphology of the samples and the involved phases could be obtained.

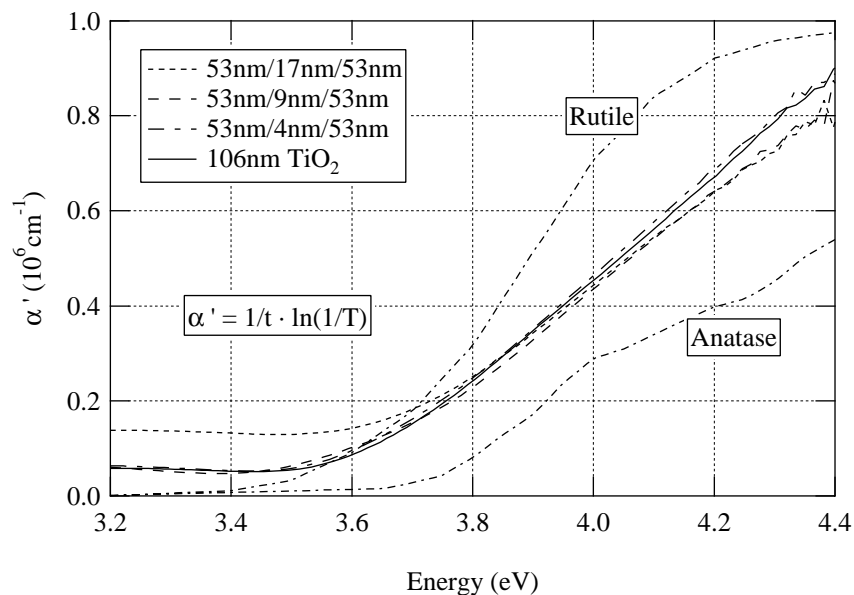


Figure 7.12: Absorption edge of the spectra shown in Figure 7.11. The absorption coefficient α' has been approximated according to the law of Lambert and Beer. Absorption coefficients for polycrystalline rutile and anatase are shown for comparison.

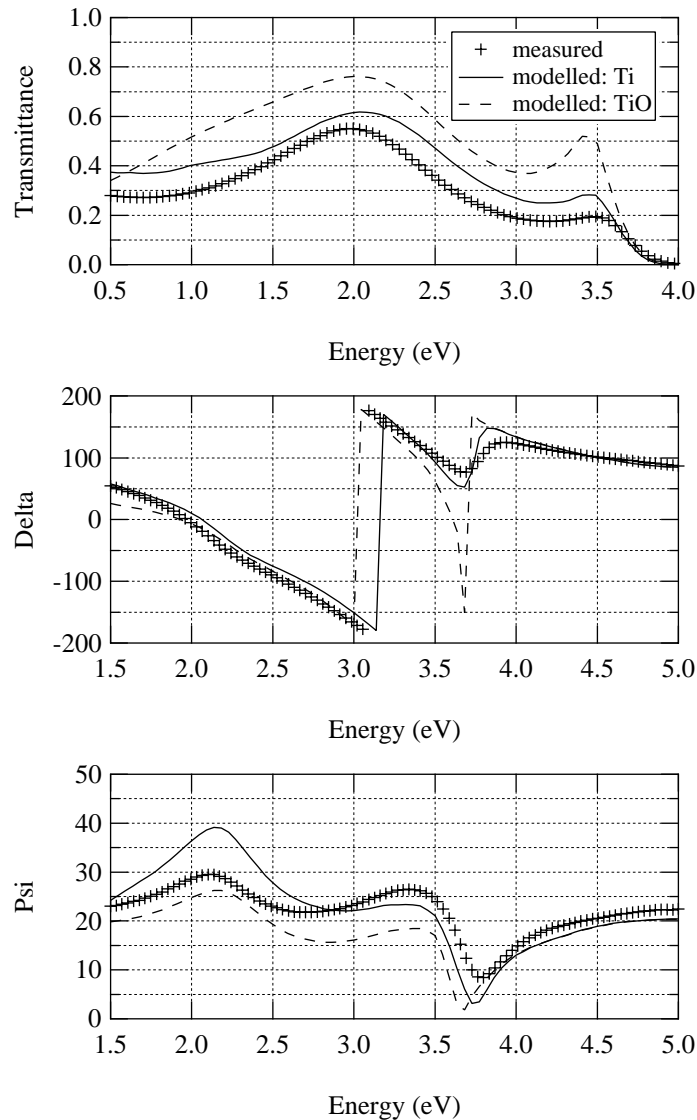


Figure 7.13: Measured (crosses) and modelled (line) spectra of a 53nm/17nm/53nm sample. The model considered the parameters listed in Table 7.1. The spectra were modelled assuming Ti (solid line) and TiO (dashed line) for the metallic interlayer, respectively. Note the difference in energy axes.

The models were tested for a well characterized sample with the structure 53nm/17nm/53nm. In a first step the sample was assumed to consist of three homogeneous layers. The structure model was defined according to the TEM observations. For the oxide layers the dielectric functions were modelled by effective medium approximations taking into account the crystalline phase composition $f_A/f_R = 0.18$ as found by Equation 5.1 from XRD measurements. The void fractions of the oxide layers were estimated according to Equation 5.2 from the layer densities obtained by RBS. The void content was 16 vol% for the lower and 24 vol% for the upper oxide layer, respectively. These appear as high values for a sputtered thin film. D. Mergel [11] has reported void fractions as high as 20 vol% in a 100 nm thick amorphous TiO₂ film. Such high void fractions are probably not real. They are likely to reflect the presence of amorphous titanium dioxide. The interface roughness was represented by roughness layers with an effective dielectric constant corresponding to a mixture of the neighboring layers. With these restrictions the only free parameter was the dielectric function of the Ti-rich interlayer of a known thickness.

In Figure 7.13 the measured and modelled transmittance and ellipsometry spectra are shown. The corresponding parameters are listed in Table 7.1. The interlayer was assumed to consist either of titanium or of monoxide. Both models yield the qualitative shape of the spectra. Especially in transmittance the assumption of the interlayer consisting of titanium yielded a better fit. The monoxide had a strong tendency for stronger absorption at low energies. In both cases, the modelled transmittance was too high over the whole spectral range. An improvement of the modelled transmittance was obtained with titanium by assuming a thicker Ti-rich layer: 15 nm instead of 10 nm as observed by TEM. This corresponds closely to the nominal metal layer thickness of 17 nm. However, at the same time the hump in Ψ around 2 eV increased. This was possibly due to an incorrect assumption for the distribution of the metal-rich regions in the sample.

Clearly the assumption of perfect oxide stoichiometry was incorrect. The optical response of reduced TiO_{2-x} can be modelled by introducing a Lorentzian term in the dielectric function of TiO₂ (Chapter 6 and 8). The Lorentzian would depend on the chemical composition. In addition, possible diffusion of titanium into the bottom oxide layer (and therefore a gradient in composition) was accounted for by inserting an additional layer. The EELS measurements suggested that the chemical composition at the interfaces changed gradually. Therefore, the roughness layers were expanded to thicker values and correspondingly the thickness of the Ti-rich layer was reduced. None of these models yielded a significant improvement compared to the triple layer model presented in Figure 7.13. The main problem was that neither the involved phases, nor their precise arrangement were known.

7.3 Discussion

Native silicon dioxide of about 20 Å thickness is commonly found on polished silicon wafers. By ellipsometry the oxide thickness on the Si wafers was determined to be 18 Å. This was in contradiction to the larger value (80 Å) measured by TEM. Possibly an interface reaction occurred between the SiO₂ of the substrate and the TiO₂ during the deposition. The formation of compounds such as TiSi₂ cannot be excluded. Another explanation could be initial oxidation of the substrate. The oxygen plasma contained free radicals and thus was very reactive. Therefore, one could imagine an oxidation of the substrate in the oxygen plasma at the very beginning of the deposition.

Important interactions between growing Ti films and TiO₂ substrates have been reported [12]. Ti can partially reduce a TiO₂ substrate and become oxidized itself [13, 14]. J.T. Mayer et al. [8] have studied the adsorption of titanium on rutile TiO₂ (110) by X-ray photoelectron spectroscopy (XPS) and low energy ion scattering (LEIS). They have concluded that the deposition (by evaporation in UHV) of 4 Å of Ti resulted in the formation of an interface layer of 12 Å of gradually more reduced titanium oxides. The interface oxide was completely covered only after additional 20 Å of Ti were deposited. Similar effects must occur at the beginning of the titanium deposition in the present study. Very likely they are even more important because the temperature of the substrate was 550 K whereas the investigation of Mayer has been performed at 150 K only [8]. For reactive magnetron sputtering Kusano et al. [15] have reported that excess O₂ supplied during oxide layer formation was gettered and diffused into a Ti layer deposited earlier. This diffusion made it difficult to estimate the chemical composition from the deposition process parameters [15]. It is likely that a similar

effect was happening during the preparation of my films. In addition, the freshly deposited titanium layer was exposed to oxygen in the sputtering atmosphere while the target was conditioned with closed shutters. Finally, as in the case of the Si substrate, initial oxidation of the titanium layer was possible. In summary, loss of oxygen to the interface reaction with the Si substrate and to the deposited Ti layer explains a reduced thickness for the lower oxide layer. This gives an explanation for the slightly lower chemical composition observed by RBS in the bottom oxide layer. The top layer may have gained in thickness by oxidizing a part of the underlying titanium.

The films discussed in the present chapter have been deposited in three steps by reactive magnetron sputtering. The structure was investigated on the cross section by TEM and a corresponding triple layer model was sufficient to account for RBS measurements. However, simple triple layer models including roughness layers failed to fit the XRR and optical measurements. Furthermore, EELS measurements on the cross section suggested a gradual change of the chemical composition. An important portion (equivalent of 6 nm) of the nominal titanium thickness was lost to oxidation and diffusion into the oxide layers. RBS, EELS and electrical measurements indicate that the titanium layers were partially oxidized with a composition close to that of TiO. Properties such as crystallite size, anatase content, and conductivity showed a tendency for saturation above 4 nm interlayer thickness. This gives a rough estimation of the interface roughness.

A different approach for investigating the TiO₂/Ti interface could be observations by surface sensitive techniques, such as X-ray photoelectron spectroscopy and Auger electron spectroscopy, on a titanium dioxide surface while successively depositing titanium. This would need to be done in-situ at very low oxygen base pressure. For reports on investigations of this kind consult e.g. [14, 16, 17 and references therein].

7.4 Conclusions

Thin films with a titanium-rich layer intercalated between two titanium dioxide layers were deposited by DC reactive sputtering. Their total thickness corresponded well to what was expected from the deposition parameters of the component layers. An increase in interlayer thickness was accompanied by an increase in DC conductivity and a decrease in transparency.

The films consisted of a mixture of anatase, rutile and amorphous phases, no titanium or titanium monoxide was observed by XRD. A correlation between the neighboring titanium-rich and oxide layers was observed: for thicker interlayers both the anatase content and the anatase crystallite size decreased.

Triple layer models did not fully account for the sample properties. The Ti-rich interlayer consisted probably of a mixture of different titanium-oxide phases. The chemical composition changed gradually towards the oxide layers. An important amount of the deposited titanium was oxidized and/or intermixed with the lower neighboring layer. At least 4 to 9 nm of titanium are needed to obtain a continuous metallic layer.

References

1. A.R. Bally, P. Hones, R. Sanjinés, P.E. Schmid, and F. Lévy, *Surface and Coatings Technology* **108-109** (1998), 166.
2. A. Bally, *Electronic properties of nano-crystalline titanium dioxide thin films*. Département de physique, Ecole polytechnique fédérale de Lausanne EPFL, Lausanne (1999).
3. O. Banakh, P.E. Schmid, R. Sanjinés, and F. Lévy, *Surface and Coatings Technology* **151-152** (2002), 272.
4. B.-S. Jeong, D.P. Norton, and J.D. Budai, *Solid-State Electronics* **47** (2003), 2275.
5. N. Martin, A.R. Bally, P. Hones, R. Sanjinés, and F. Lévy, *Thin Solid Films* **377-378** (2000), 550.
6. *PDF-database*. JCPDS, International centre for diffraction data (ICDD), 1601 Park Lane, Swarthmore, PA 19081, USA.
7. P. Knauth and H.L. Tuller, *J. Appl. Phys.* **85** (1999), 897.
8. J.T. Mayer, U. Diebold, T.E. Madey, and E. Garfunkel, *Journal of Electron Spectroscopy and Related Phenomena* **73** (1995), 1.
9. M.A. Henderson, *Surf. Sci.* **419** (1999), 174.
10. *CRC Handbook of chemistry and physics*. 67th ed., CRC Inc., Boca Raton (1986).
11. D. Mergel, *Thin Solid Films* **397** (2001), 216.
12. I. Vaquila, M.C.G. Passeggi Jr., and J. Ferron, *Phys. Rev. B* **55** (1997), 13925.
13. C.T. Campbell, *Surface Science Reports* **27** (1997), 1.
14. U. Diebold, *Surface Science Reports* **48** (2003), 53.
15. E. Kusano, A. Kinbara, and I. Kondo, *Journal of Non-Crystalline Solids* **218** (1997), 58.
16. V.E. Henrich and P.A. Cox, *The surface science of metal oxides*. 1st ed., Cambridge University Press, Cambridge (1994).
17. C.E. Sittig, *Charakterisierung der Oxidschichten auf Titan und Titanlegierungen sowie deren Reaktionen in Kontakt mit biologisch relevanten Modellösungen*, Eidgenössische Technische Hochschule ETHZ, Zürich (1998).

Chapter 8 Periodicity in the oxygen supply

8.1 Introduction

Bulk oxygen vacancies are known to generate shallow electron donors that contribute to the electrical conductivity of TiO_2 . Recent theoretical calculations have proposed that reduced crystal surfaces also produce donor states [1]. This opens the possibility of reaching a high doping level in nanocrystalline TiO_2 by introducing donor states at the grain boundaries. We have investigated the effects of partially reduced grain boundaries on nanocrystalline TiO_2 , and simulated the effects related to the grain size. The samples were deposited with oxygen as reactive gas. By introducing a periodicity in the reactive gas supply the deposition of a stacked arrangement of oxygen defect rich layers was attempted. The periodicity in the sputtering parameters allowed influencing the crystallite size.

TiO_2 is commonly combined in multilayers with SiO_2 for optical filters [2, 3]. Stratified structures of Ti and TiN have been investigated for mechanical properties [4, 5]. To my knowledge, little work has been done on multilayers combining titanium and titanium dioxide. Kusano et al. [6] have deposited such multilayer films by reactive magnetron sputtering. By modulating the oxygen gas flow they obtained films with a continuous, sinusoidal, change in chemical composition over the depth of the films. In their films the period thickness was in the order of 150 nm. Unfortunately, the authors have not given any further information about the optical, electrical and mechanical properties of their films. N. Martin et al. [7] have proposed a pulsed reactive gas technique for the sputter deposition of titanium oxides. By periodically modulating the oxygen supply they achieved a significant increase in the deposition rate of titanium dioxide. Their objective was not to obtain multilayers. With periods of 16 seconds (corresponding to 0.7 nm thickness) the pulsing rate was too quick for the formation of stratified structures. Fabreguette and Chiamonte et al. [8, 9] have reported epitaxial growth of $\text{TiO}_2/\text{TiN}_x\text{O}_y$ superlattice structures. Their films had a thickness of about 300 nm with intercalated TiN_xO_y layers of 1 to 2 nm in 100 nm thick TiO_2 layers. The nitrogen to oxygen ratio in the TiN_xO_y layer was approximative 2.6. However, little efforts have been spent on investigating the optical and electrical properties of such multilayered films.

8.2 Sample preparation

Titanium-rich layers were incorporated in films of titanium dioxide deposited by reactive magnetron sputtering. Thin films of about 400 nm overall thickness were prepared. In a first series, a constant ratio of metal to oxide layer thickness but variable period (defined as a pair of oxide and metal layer) kept the overall chemical composition constant but changed the number of interfaces in the sample. The structures of these samples are summarized in Table 8.1. In a second series, the number of titanium layers was kept constant but the titanium layer

thickness was changed, resulting in a variation of the overall chemical composition. The first and last layers in the stacks were TiO₂ layers.

Number of periods	TiO ₂ thickness equivalent (nm)	Ti thickness equivalent (nm)
72	5	0.5
36	10	1
18	20	2
9	40	4
TiO ₂ reference	400	0

Table 8.1: Overview of sample structures.

Argon was introduced as working gas at a constant flow rate of 22.7 sccm. To the ambient 4 sccm of oxygen were added while depositing oxide layers. The total pressure (Ar + O₂) was $2.66 \cdot 10^{-3}$ mbar. The pumping speed was 160 ls⁻¹. A constant discharge current of 300 mA was used. The rate of deposition was obtained from quartz microbalance and profilometer measurements on reference samples to 1.1 Ås⁻¹ for titanium and 0.4 Ås⁻¹ for titanium dioxide. Si wafers and microscope slide glass were used as substrate materials (Table 3.1). During the deposition the substrates were heated to 250 °C and electrically grounded.

To achieve the alternation between oxide and metal layers, oxygen was added periodically to the constant argon gas flow. Figure 8.1 shows the behavior of the target voltage when the oxygen supply is interrupted for a short period. Breaks of 5 to 40 seconds are shown. When a constant current is applied on the target the discharge voltage depends on the resistivity of the target surface. Hence it gives an indication of the oxidation state of the target [7, 10]. In the presence of oxygen the high target voltage corresponded to an oxidized target surface. After cutting off the oxygen supply the target surface was rapidly reduced. Correspondingly, the voltage decreased. The decrease was fitted by an exponential function with a time constant of 1.3s. This corresponded to the slowest of the following processes: the time necessary for the flow regulator to shut, the tubes and the chamber volume to be purged off oxygen and the target to change to the metallic state. With the interruption of the oxygen supply the deposition rate monitored by the quartz microbalance increased and the mass spectrometer signals corresponding to mass numbers 16 (O⁺) and 32 (O₂⁺) fell to zero.

In the following discussion samples will be identified by their structure. For instance, 18×(20nm/2nm) stands for a sample with 18 pairs of one nominally 20 nm thick TiO₂ layer and one 2 nm thick Ti layer deposited successively on top of an initial TiO₂ layer.

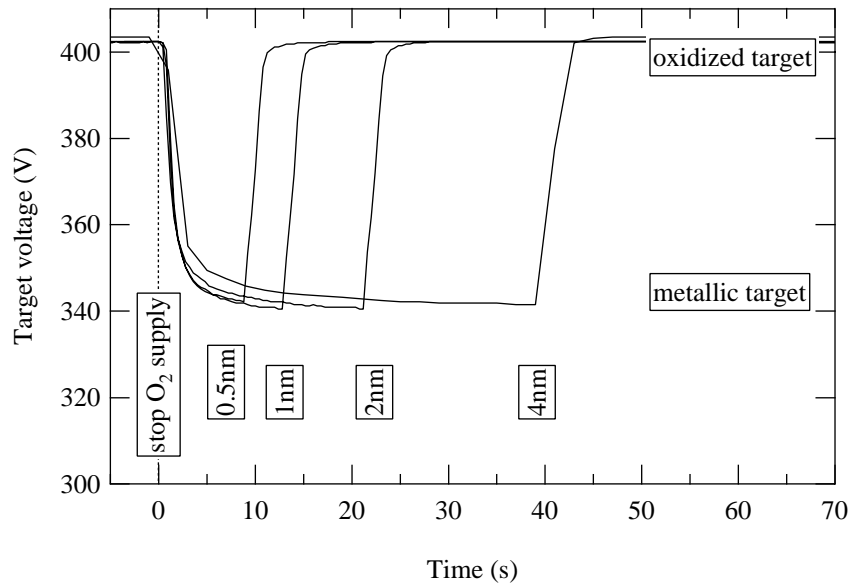


Figure 8.1: Behavior of the target voltage during oxygen supply interruptions. The target voltage decrease is exponential with a time constant of 1.3 s. The metal layer thickness depends on the duration of the pulse. It varied between 0.5 and 4 nm.

8.3 Results

The samples were characterized by the techniques presented in Chapter 4. Spectrophotometry and spectroscopic ellipsometry were performed. The knowledge of structural properties was important for the construction of the optical models.

8.3.1 Morphology and crystalline structure

Film thicknesses measured by profilometry was roughly 10 % more than what was expected according to the deposition parameters. The thickness values measured for the same deposition on glass and Si substrates were within measurement errors. These measurements were complemented by cross-section TEM observations.

8.3.1.1 X-ray diffraction

X-ray diffraction patterns of a series of samples with different deposition periods are reported in Figure 8.2. The background due to the glass substrate has been subtracted. Samples deposited with short periods are shown at the bottom of the figure. They had a crystallinity in the order of 20 %. For thicker periods the crystallinity increased to 60 %. Rutile was the predominant crystalline phase in all samples. This predominance of the rutile phase in the presence of a slight disturbance is well known [11]. A reference TiO_2 film deposited with the same process parameters crystallized in the anatase phase. It was 80 % crystalline.

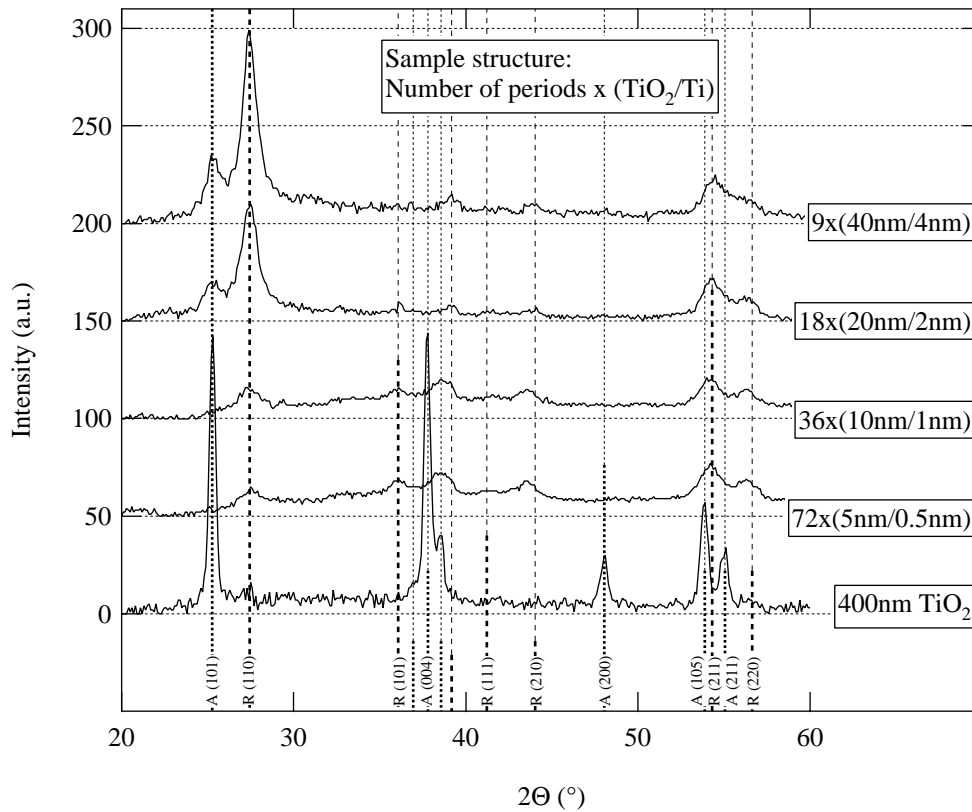


Figure 8.2: Grazing incidence XRD pattern of multilayered samples on glass substrates. The intensity contribution of the glass substrate has been subtracted. The vertical lines (intensities and positions according to [12]) mark the peak positions of anatase (dotted, label A) and rutile (dashed, label R).

All the observed peaks could be assigned to either rutile or anatase. No peak corresponding to metallic titanium, nor to titanium monoxide, nor to any other substoichiometric phase could be distinguished. All samples had crystallite sizes in the order of 10 nm. The size of rutile crystallites is reported in Figure 8.3 (left). It increased with increasing period thickness. TiO_2 reference samples consisted of mostly anatase and had a crystallite size of about 40 nm. This indicates that the small amount of titanium was sufficient to provoke a preferential formation of rutile, and that even the shortest Ti pulses (equivalent to a thickness of 0.5 nm) interrupted the TiO_2 crystallite growth. This points at a possible method to modify the crystallite size in a polycrystalline film without significantly changing the chemical composition.

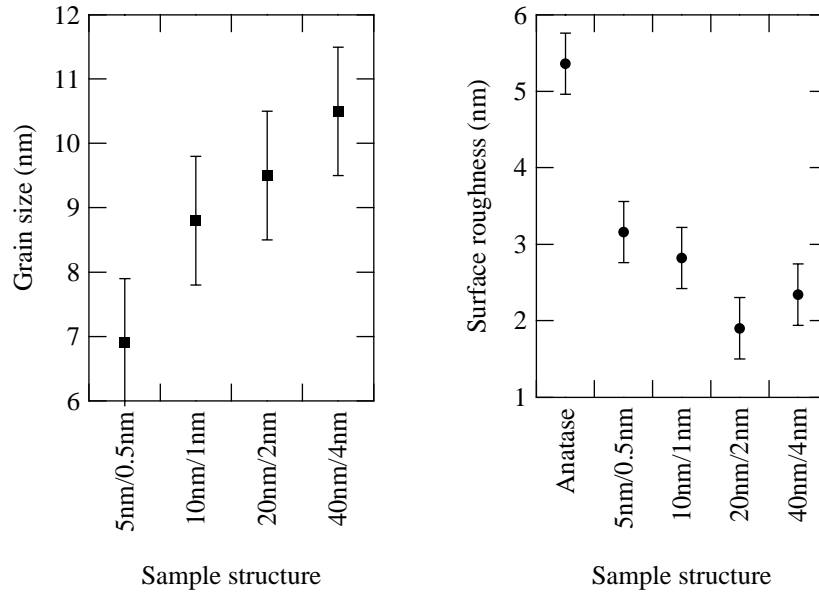


Figure 8.3: Rutile crystallite size determined from the X-ray diffraction pattern (left). Root mean square surface roughness measured by AFM on 500 nm \times 500 nm scans (right). The sample structure is given by oxide and metal layer thicknesses.

8.3.1.2 Surface characterization by AFM and STM

Atomic force microscopy (AFM) observations in non-contact mode were performed on the samples. The grain size estimated from AFM pictures (500 nm \times 500 nm) were about a factor of 4 larger than the size found from the X-ray patterns. Scanning tunneling microscopy (STM) observations indicated that the large, flat grains of TiO₂ actually consisted of several crystallites. The size of these crystallites corresponded well to the values obtained by XRD. Examples of an AFM and an STM picture taken on 200 nm \times 200 nm squares on the surface of a 9 \times (40nm/4nm) sample are shown in Figure 8.4. The surface roughness measured by AFM showed a tendency to decrease in films with longer periods but comparable total film thickness. This is reported on the right in Figure 8.3. For samples with the structure 18 \times (20nm/ t_{metal}) the roughness decreased from 3.8 to 2.3 nm with an increase in the metal layer thickness t_{metal} from 1 to 2 nm. The surface roughness gives an upper limit for the interface roughness. The decrease in roughness was possibly due to Ti partially filling up the voids between the grains.

8.3.1.3 Cross section characterization by TEM

Cleaved edges of the samples were investigated by cross-sectional TEM. Two dark field images are shown in Figure 8.5. The silicon substrates can be seen in the right bottom corner. A 7 ± 1 nm thick amorphous silicon oxide layer is visible between the substrate and the titanium oxide film. A TEM specimen of a multilayered sample was prepared by mechanical polishing and ion milling. All three specimens showed columnar morphologies. Column diameters were approximately 40 nm for all samples. This compares well with the grain diameter measured on the sample surface by AFM. No multilayered structure or interruption of the columnar growth was clearly visible.

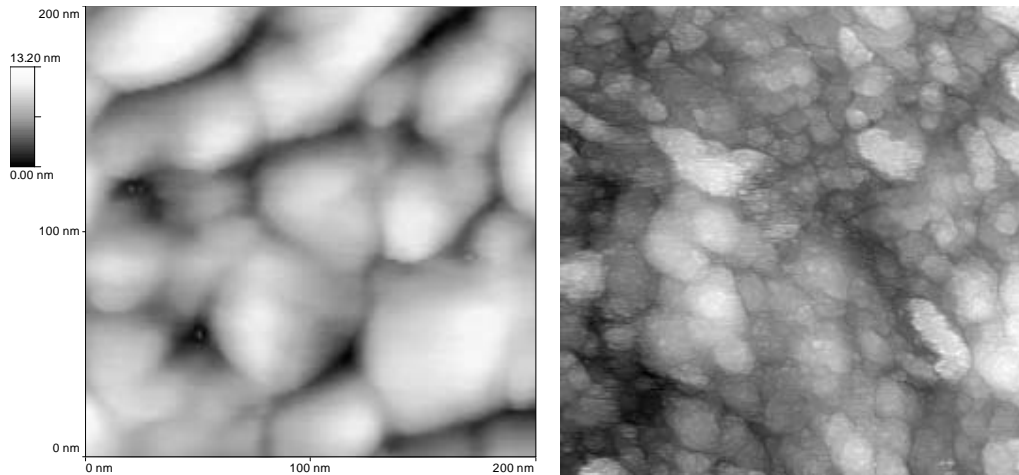


Figure 8.4: AFM (left) and STM (right) topography images of the surface of a sample with the structure $9 \times (40\text{nm}/4\text{nm})$. The shown area is $200\text{ nm} \times 200\text{ nm}$ in both cases. Large grains seen by AFM in air appear as agglomerates of several small grains by STM in vacuum.

In the dark field image bright areas correspond to regions with the same (110) rutile orientation. Grains with a different orientation and defects appear as dark areas. The sample with longer periods (left) had a coarser grain structure than the sample with the $72 \times (5\text{nm}/0.5\text{nm})$ structure (Figure 8.5 (right)). For this sample one recognizes regular arrangements of defects with a spacing of $6 \pm 2.5\text{ nm}$. This is close to the deposition period of 5.5 nm . This was less clear for the sample structure $9 \times (40\text{nm}/4\text{nm})$ (image shown on the left). The TEM observations are in agreement with the interpretation that in the absence of reactive gas, titanium is deposited preferentially between the oxide grains rather than as a homogeneous metal layer.

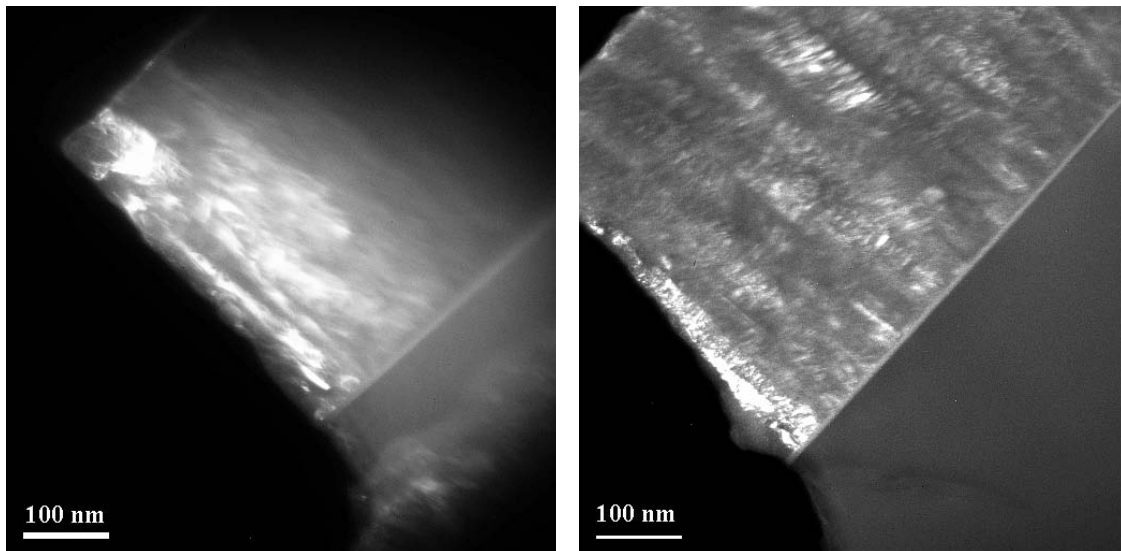


Figure 8.5 Dark-field TEM images (Rutile (110) diffraction spot) taken on cleaved corners of multilayered samples on Si substrates: left: $9 \times (40\text{nm}/4\text{nm})$, right: $72 \times (5\text{nm}/0.5\text{nm})$. The Si substrate appears at the bottom on the right. The gray line between substrate and films corresponds to amorphous silicon oxide.

8.3.2 Electrical properties

The in-plane DC electrical conductivity of samples prepared on glass substrates was measured in the van der Pauw geometry. The corresponding Arrhenius plots are presented in Figure 8.6. The samples had a constant overall oxide to metal layer thickness ratio (10 to 1), but different sublayer thicknesses (Table 8.1). The samples exhibited a semiconducting behavior. The thermal activation energy E_A was of the order of 100 meV, with a tendency to decrease at higher T. The films showed good reproducibility of the conductivity values when heating several times to 500 K.

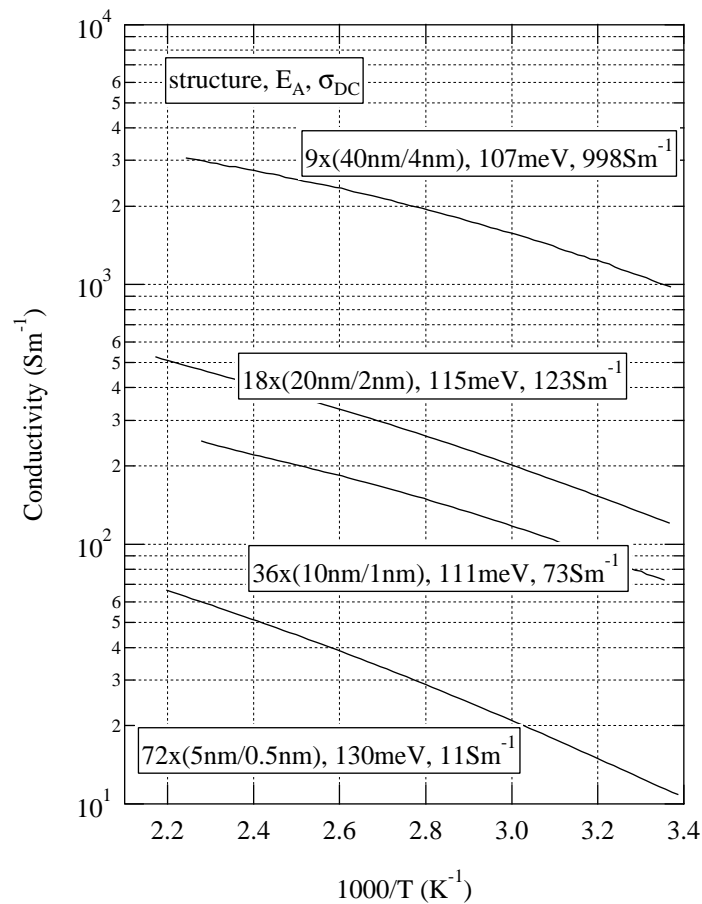


Figure 8.6: Temperature dependence of the in-plane DC conductivity for different layer thicknesses at constant TiO_2/Ti ratio. In the boxes are marked: sample structure, thermal activation energy and the conductivity at room temperature.

For thicker and fewer TiO_2/Ti periods the conductivity increased dramatically even though the overall titanium content remained constant (see Section 8.4.1 for further discussion). The room temperature conductivity was 10^2 to 10^4 times lower than one would expect in the presence of continuous TiO or Ti layers of the nominal thicknesses. This and the fact that σ_{DC} was thermally activated confirms that the incorporated titanium did not form a continuous metallic layer. It was partially oxidized and/or dispersed in isolated grains.

In Figure 8.7 the room temperature conductivity and the activation energy are plotted versus the sample structure. With increasing nominal Ti layer thickness (and therefore increasing grain size and crystallinity) the conductivity increased. This will be explained below by a combined increase of the carrier density and their mobility. The values for the thermal activation energy E_A varied between 105 and 130 meV. The lowest activation energy was found for the samples deposited with the longest deposition periods.

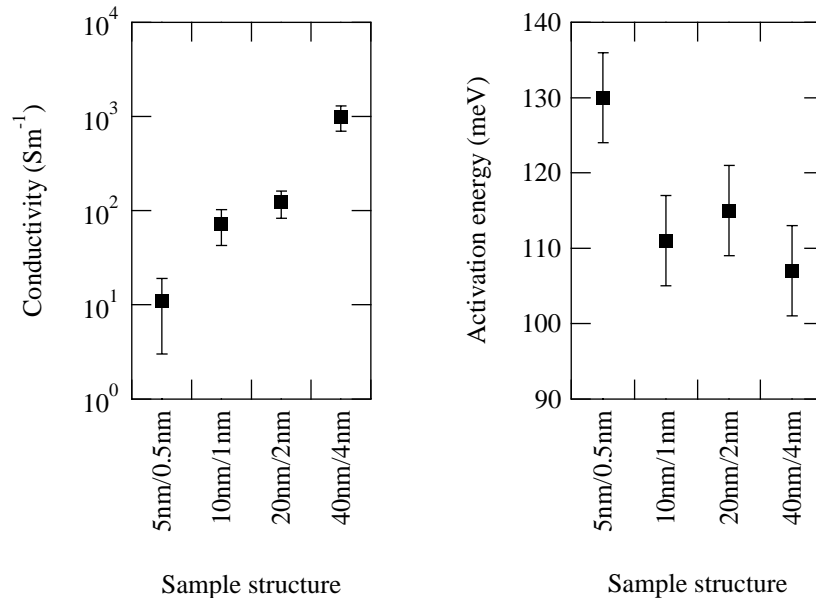


Figure 8.7: In-plane DC conductivity at RT (left) and thermal activation energy E_A (right) versus sample structure.

8.3.3 Optical properties

Spectrophotometry and spectroscopic ellipsometry measurements were performed on glass and Si substrates. The transmittance spectra of a series of samples are reported in Figure 8.8. Interference fringes are visible below the fundamental absorption edge. Their spacing is due to the total film thickness and is not due to multiple reflections within one sublayer. The films deposited with thin Ti layers were highly transparent (more than 60 % for the substrate-film system) as in the case for undoped TiO_2 films. For thicker Ti layers an absorption band appeared around 1 eV.

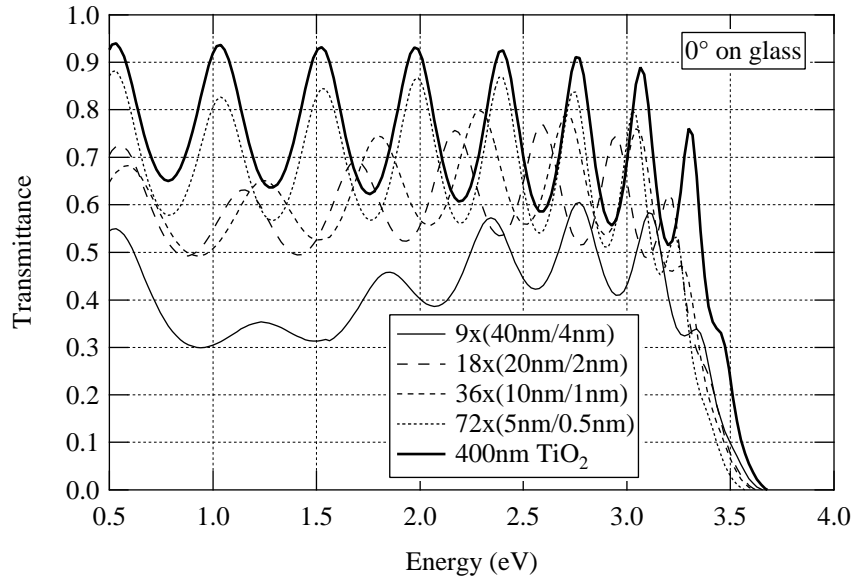


Figure 8.8: Normal incidence transmittance spectra of multilayered TiO_2/Ti samples with different period thickness on glass substrates.

In Figure 8.9 the region around the absorption edge is shown. Due to the high amorphous fraction (40 to 80 %) the onset of the absorption is softer than in rutile and anatase. For increasing period thickness the absorption edge was shifted to higher photon energies. From the least to the most conducting sample the photon energy for $\alpha' = 10^5 \text{ cm}^{-1}$ shifted towards higher energies by 65 meV. The Burnstein-Moss effect [13] could only account for 10 meV. A possible reason for the blue shift of the absorption edge can thus be the increase in grain size and/or the increasing anatase content (see Figure 8.2).

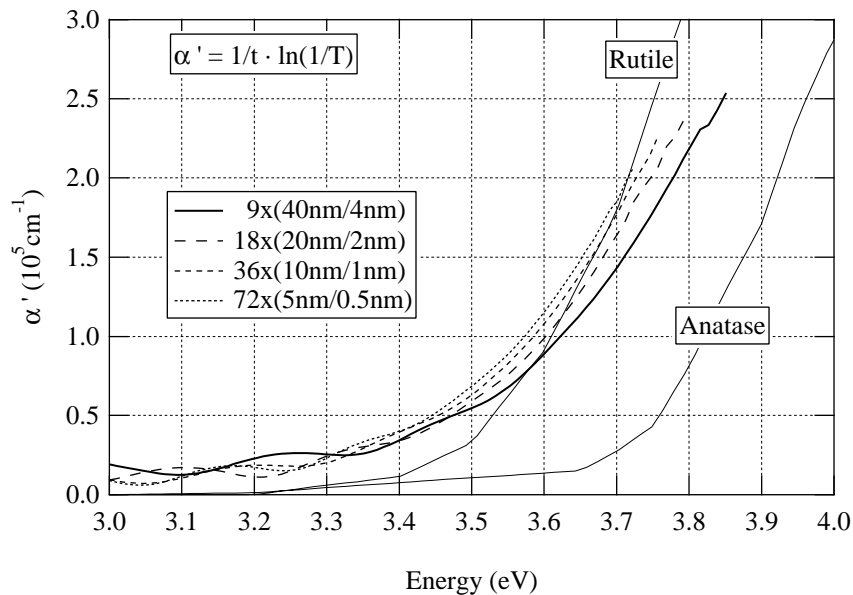


Figure 8.9: Absorption edge for the spectra shown in Figure 8.8. The absorption coefficient α' has been approximated according to the law of Lambert and Beer. Absorption coefficients for polycrystalline rutile and anatase are shown for comparison.

Several model structures have been evaluated for the interpretation of the optical properties. They are summarized in Table 8.2. In a first approach (Models I and II) the films were assumed to consist of TiO_2 intermixed with metallic phases (Ti or TiO). Indications about the arrangement of the phases present in the films can be obtained from the evaluation of the optical response of different structure models. Due to the periodicity in the sputtering parameters Ti-rich regions were expected to be arranged in strata, but not as continuous layers. The second approach (Model III) assumed that the TiO_2 was reduced and no Ti or TiO was present in the film. In all models the dielectric function of the dioxide was modelled by a Bruggeman combination of anatase, rutile and voids. For rutile the optical axis was assumed to lie in the sample plane.

Model	Structure	Equations
I	Arbitrary stratified structure of oxide and metal layers (EMA)	B.1, B.2
II	Metallic inclusions arranged in layers	A.17, B.4
III	Homogeneous oxide layer with additional absorption band	C.2

Table 8.2: Overview of optical models investigated for the multilayered samples. The column on the right refers to the most important formulae for the respective models. They are given in the appendices.

8.3.3.1 Model I: EMA for a stratified structure

In Model I a stratified structure was assumed for the effective medium approximation (Appendix B). The model was evaluated for a mixture of TiO_2 and either Ti or TiO interlayers. The dielectric properties $\epsilon_o(\omega)$ in the sample plane were modelled according to Equation B.1, whereas $\epsilon_e(\omega)$ normal to the sample was modelled according to Equation B.2. This model did not specify the exact structure of the stacked layers: neither number nor exact thickness of the stacked planes were involved as parameters. The model is also valid for independent metallic tiles of different sizes lying in the sample plane. This is in accordance with the fact that no continuous layers have been observed by DC conductivity measurements or by TEM on the cross section. The model does not apply anymore as soon as there are vertical structures such as metallic inclusions that have diffused along the grain boundaries.

Parameter	Nominal (Ti)	Titanium	Monoxide
f_{metal} (%)	10	3	8
t (nm)	406 ⁽ⁱ⁾	405	410
x in TiO_x	1.7	1.9	1.9

Table 8.3: Summary of parameters for Model I of a $9 \times (40\text{nm}/4\text{nm})$ structured sample: metal volume fraction f_{metal} and sample thickness t . The chemical composition x has been calculated from these parameters taking into account the density and molar mass to convert the metal content from vol% to at%. (i) Measured by profilometry.

The only free parameter of this model was the metal content f_{metal} . It was optimized to find reasonable values for transmittance over a wide spectral range. The model parameters are summarized in Table 8.3 and corresponding modelled spectra are presented in Figure 8.10. The example shown had the structure $9 \times (40\text{nm}/4\text{nm})$. Starting values for the other

parameters, such as film thickness t , surface roughness t_{RMS} , and crystalline phase composition f_A/f_R , were obtained from XRD and AFM observations. The model parameters were optimized to match the interference fringes and the absorption edge.

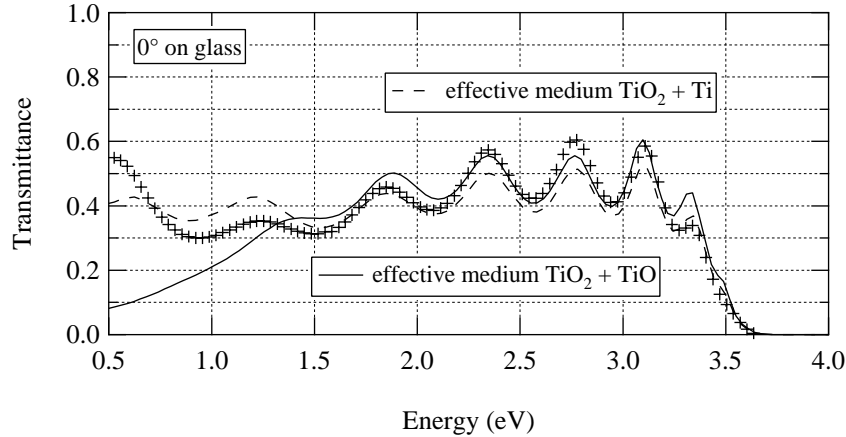


Figure 8.10: Measured (crosses) and modelled (lines) normal incidence transmittance spectra of a $9 \times (40\text{nm}/4\text{nm})$ sample. The modelled spectra are based on an EMA for a stratified sample structure. Model parameters are listed in Table 8.3.

When metallic titanium layers were considered (dashed line), f_{metal} was approximately 3 %. The transmittance was reduced over the whole photon energy range and it was not possible to account for the absorption band around 1 eV while at higher energies the absorption was already too low. With TiO layers the model fitted reasonably well above 2 eV. At lower energies the transmittance decreased too rapidly. This was due to plasmonic absorption that has been reported for titanium monoxide thin films [14].

8.3.3.2 Model II: Metallic inclusions arranged in layers

In Model II the oxide layers were alternated with metal-rich layers (matrix formalism, Chapter 5 and Appendix A). The metal-rich layers were assumed to consist of TiO_2 with inclusions of metallic (Ti or TiO) grains. The dielectric function of these layers was calculated according to the Maxwell-Garnett effective medium approximation (Equation B.4). The crucial parameter was the metal content. It was determined by the thickness t_{metal} of the metal-rich layers and the metal volume fraction f_{metal} within these layers. Neither t_{metal} nor the thickness t_{oxide} of the oxide layers were accessible by independent measurements. For t_{metal} the nominal thickness was assumed and f_{metal} was left as free fitting parameter.

The results for the sample discussed above are presented in Figure 8.11 and Table 8.4. In the case of Ti inclusions (dashed line) the transmittance at high energies decreased too quickly. In the case where the metallic grains consisted of TiO an absorption band around 1 eV appeared in the model spectra (solid line). However, it tended to be too strong and too narrow compared to the measured spectra.

Parameter	Nominal (Ti)	Titanium	Monoxide
t_{oxide} (nm)	40	41	41
t_{metal} (nm)	4	4	4
f_{metal} (%)	100	30	40
t (nm)	406 ⁽ⁱ⁾	406	406
x in TiO_x	1.7	1.9	1.95

Table 8.4: Overview of parameters for Model II: thickness of oxide layers t_{oxide} , thickness of metal-rich layers t_{metal} , metal content f_{metal} in the metal-rich layers, and total film thickness t . The chemical composition x has been calculated from these parameters. (i) Measured by profilometry.

Further modifications of Model II were tested, too. In particular, the Maxwell Garnett EMA was replaced by the Bruggeman approximation (Equation B.5) and/or the metallic inclusions were dispersed over the whole thickness of the film. None of these simple models assuming Ti or TiO inclusions allowed obtaining a satisfactory representation of spectrophotometry and spectroscopic ellipsometry spectra. The example presented in Figure 8.10 and Figure 8.11 corresponded to a sample with the structure $9 \times (40\text{nm}/4\text{nm})$, i.e. it was deposited with relatively thick periods. This was the most likely structure, to exhibit a stratified arrangement of metallic inclusions, whereas samples with shorter periods were expected to be more dispersed.

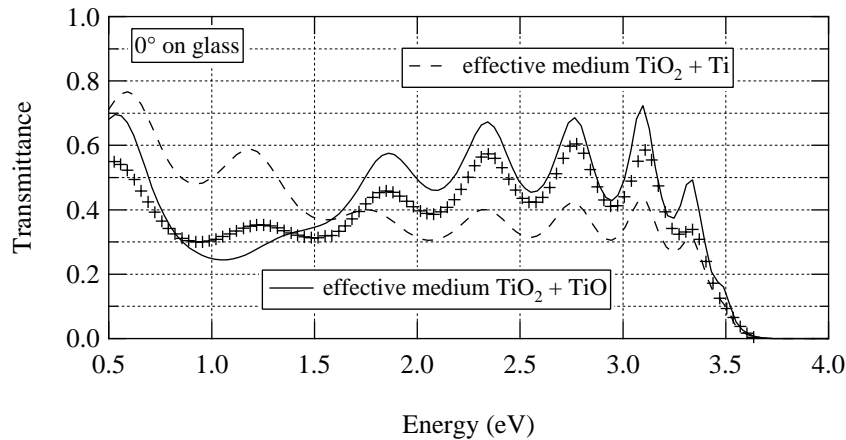


Figure 8.11: Measured (crosses) and modelled (lines) transmittance spectra of a $9 \times (40\text{nm}/4\text{nm})$ sample. The modelled spectra are based on stacks of layers of TiO_2 with and without metallic inclusions (Ti (dashed line) or TiO (solid line)) Model parameters are reported in Table 8.4.

An estimate of the maximum concentration of elemental titanium and titanium monoxide could be obtained from the models. A maximum of 1 to 2 vol% of metallic titanium or 2 to 3 vol% of titanium monoxide can be included in the optical calculations while keeping the modelled transmittance higher than the measured transmittance. More TiO in the film increases the absorption in the IR whereas more Ti results in an increased absorption in the VIS spectral range (see also Figure 8.10 and Figure 8.11). This indicates that the deposited titanium was oxidized and was not present as metallic inclusions.

8.3.3.3 Model III: Homogeneous layer with absorption band

The approach followed up to now was to combine constituents with known dielectric functions and search for the unknown geometrical arrangement. But the phases present in the films were not completely known (see also the discussion in Chapter 7). Even though no signal of Ti_2O_3 or other substoichiometric phases appeared in the X-ray diffraction patterns (Figure 8.2), the presence of such phases could not be excluded completely. Titanium monoxide has a wide homogeneity range (cf. phase diagram Figure 2.3 and Section 2.1). The optical properties of TiO_x with $x \approx 1$ depend on the chemical composition [14].

Parameter	Measured	Optical model
t_{RMS} (nm)	2.3 ± 0.2 (AFM)	2.5 ± 2
t (nm)	406 ± 11 (Profilo.)	405 ± 2
t_{SiO_2} (nm)	7 ± 1 (TEM)	7 ± 1
f_A (%)	19 ± 10 (XRD)	19 ± 10
f_{vac} (%)	---	5 ± 2

Table 8.5: Measured film properties and parameters in the Model III for a $9 \times (40\text{nm}/4\text{nm})$ sample.

Model III assumes a less complex film structure and few fitting parameters. In this model it has been supposed that no metallic inclusions were present but the TiO_2 was reduced. Accordingly the whole film was modelled as one single layer and any anisotropy due to the periodic modulation of the deposition parameters was neglected. The substoichiometry of the films was accounted for by introducing a Lorentzian in the IR.

This model yielded good results for the samples discussed in the present chapter. The parameters found for a sample with the structure $9 \times (40\text{nm}/4\text{nm})$ are summarized in Table 8.5. The IR absorption band was represented by a Lorentzian with $\hbar\omega = 1.15$ eV, $f_l = 1.6$, $\hbar\gamma = 1.9$ eV (Table 8.6). The corresponding spectra are shown in Figure 8.12 and Figure 8.13. In transmittance the absorption band can be nicely fitted. As already discussed in Chapter 6 the discrepancies between model and measurement around 3 to 3.5 eV are due to modifications around the absorption edge not accounted for in the reference data. The reflectance spectra fitted well in the infrared and above the absorption edge. Probably due to texture in the nanocrystalline structure insufficiently accounted for in the model, the calculated reflectance was somewhat lower than the measurement between 1.5 eV and 3 eV. In particular, the amorphous component has been neglected so far. The corresponding ellipsometry spectra are reported in Figure 8.14. Δ was well represented by the proposed model whereas in Ψ the modelled contrasts were higher than the measured ones. However, the Ψ spectrum shown is a better representation than the Ψ spectra obtained from Models I and II.

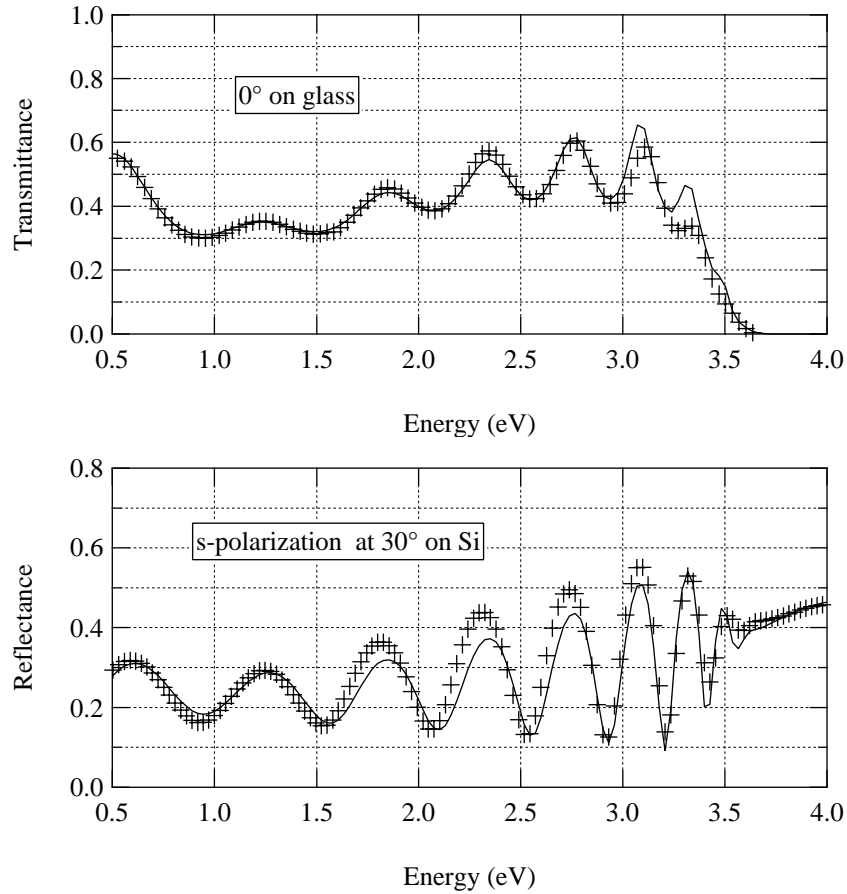


Figure 8.12: Spectrophotometry measurements (crosses) and corresponding model (lines) of a $9 \times (40\text{nm}/4\text{nm})$ sample. The upper part shows transmittance spectra at normal incidence and the lower part shows polarized reflectance spectra at 30° incidence. Spectra were calculated according to Model III. Model parameters are listed in Table 8.5. Lorentzian parameters were $\hbar\omega = 1.15$ eV, $f_l = 1.6$, and $\hbar\gamma = 1.9$ eV.

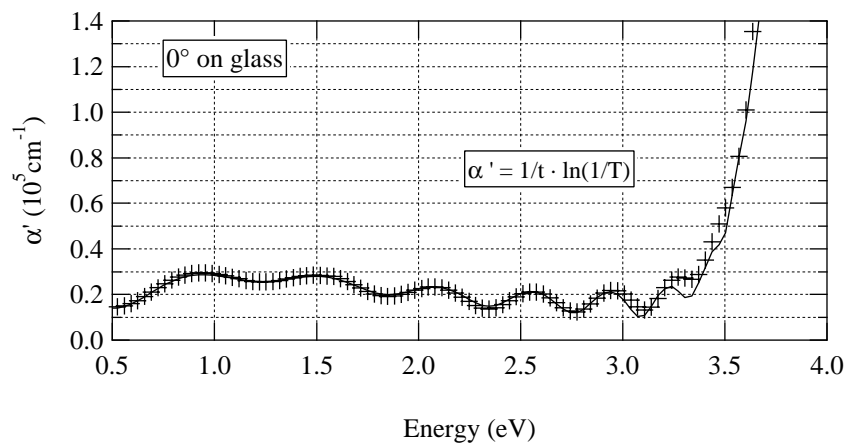


Figure 8.13: Measured (crosses) and modelled (lines) absorption coefficient α' corresponding to the spectra shown in Figure 8.12. α' has been approximated by the law of Lambert and Beer. The measured (thin film) absorption onset is softer than in the model (based on single crystal data).

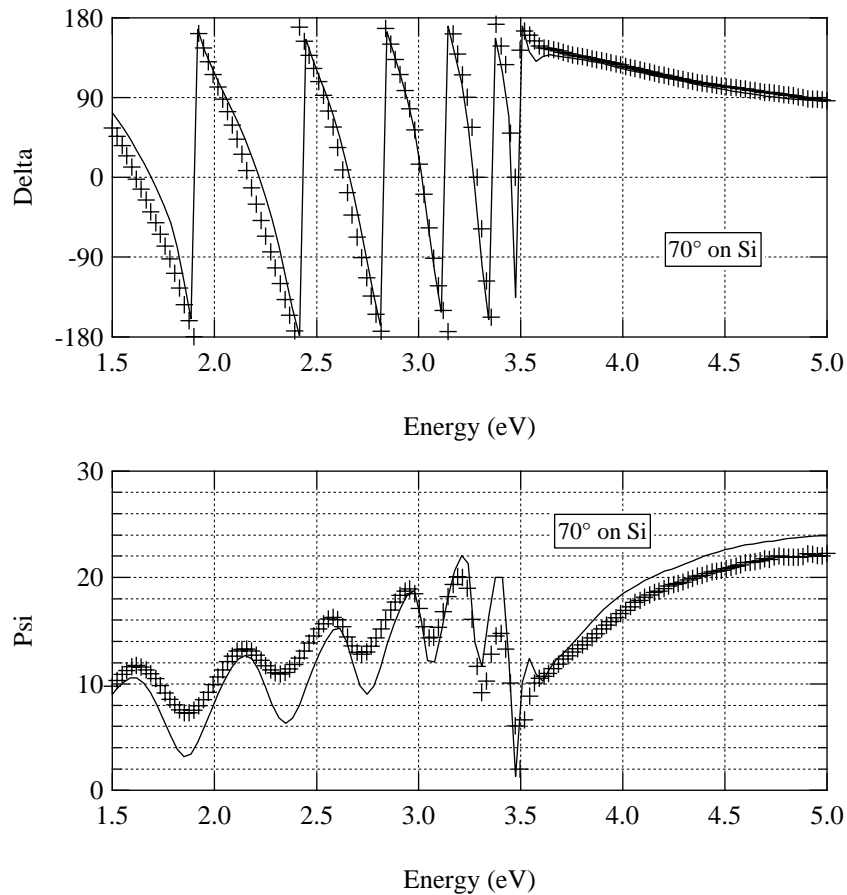


Figure 8.14: Measured (crosses) and modelled (lines) ellipsometry spectra of a $9 \times (40\text{nm}/4\text{nm})$ sample. The model was the same as in Figure 8.12.

The Lorentzian parameters found by fitting Model III to the measured spectra are summarized in Table 8.6. The corresponding dielectric functions are presented in Figure 8.15. The following discussion about the electrical properties will be based on these results.

Sample structure	$\hbar\omega$ (eV)	f_l	$\hbar\gamma$ (eV)
$9 \times (40/4)$	1.15 ± 0.05	1.6 ± 0.05	1.9 ± 0.1
$18 \times (20/2)$	1 ± 0.05	0.65 ± 0.05	1.7 ± 0.1
$36 \times (10/1)$	1 ± 0.05	0.6 ± 0.05	1.6 ± 0.1
$72 \times (5/0.5)$	1 ± 0.05	0.18 ± 0.05	1.6 ± 0.1

Table 8.6: Lorentzian parameters describing the absorption band in the optical Model III. Parameters are defined in Equation C.2.

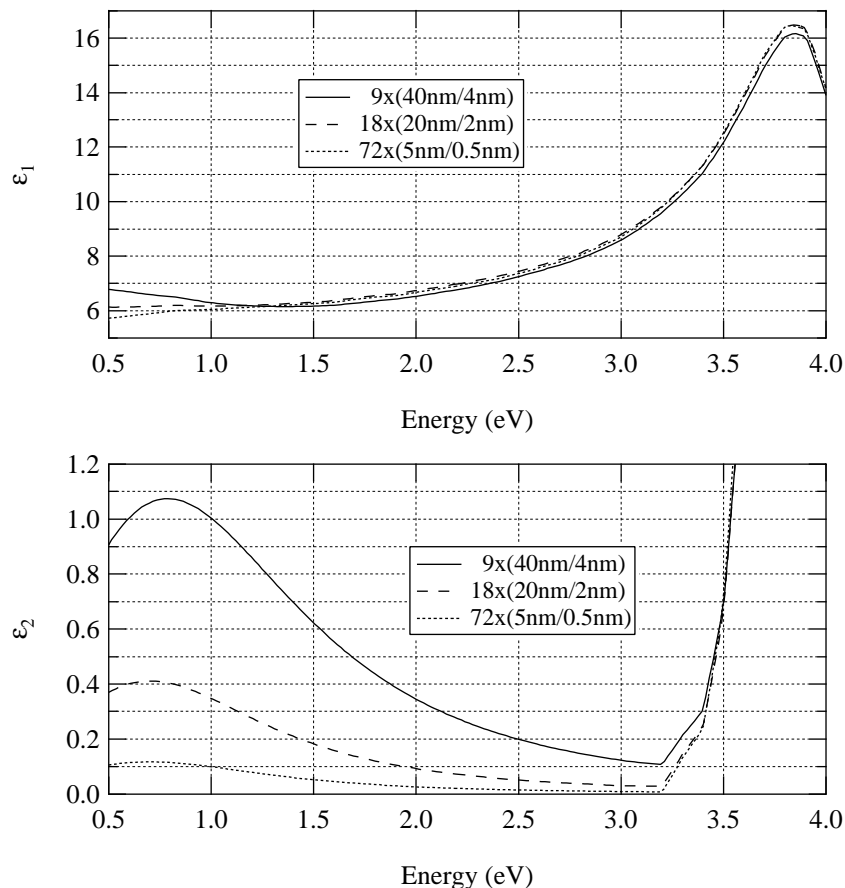


Figure 8.15: Dielectric functions (according to Model III) corresponding to the spectra shown in Figure 8.8.

8.4 Discussion

8.4.1 Optical and electrical properties

The multilayered samples investigated in the present chapter revealed the presence of an absorption band in the infrared spectral region (Figure 8.8). This resembles in position and width the absorption band in TiO_{2-x} reported in Chapter 6. Its amplitude depended on the period in the reactive gas supply. From the modelled dielectric function (Model III) the absorption coefficient $\alpha(\hbar\omega)$ was calculated (Equation 6.2). A normalized absorption coefficient $\alpha(\hbar\omega)/\sigma_{DC}$ is presented in Figure 8.16. The different sample structures are indicated in the figure and literature values for a rutile single crystal have been added [15]. For all samples the observed absorption band had its maximum α_{max} between 1 eV and 1.2 eV, in good agreement with the results of Chapter 6.

Unlike α_{max}/σ_{DC} for the single layer samples prepared with water vapor, α_{max}/σ_{DC} was not constant for the multilayers prepared with a pulsed O_2 supply. For thin periods it was as high as 19 $\text{k}\Omega$. This value decreased for thicker periods and reached with 2.1 $\text{k}\Omega$ for the 9x(40nm/4nm) structure the same level as the water-deposited samples of Type B (Table 6.5).

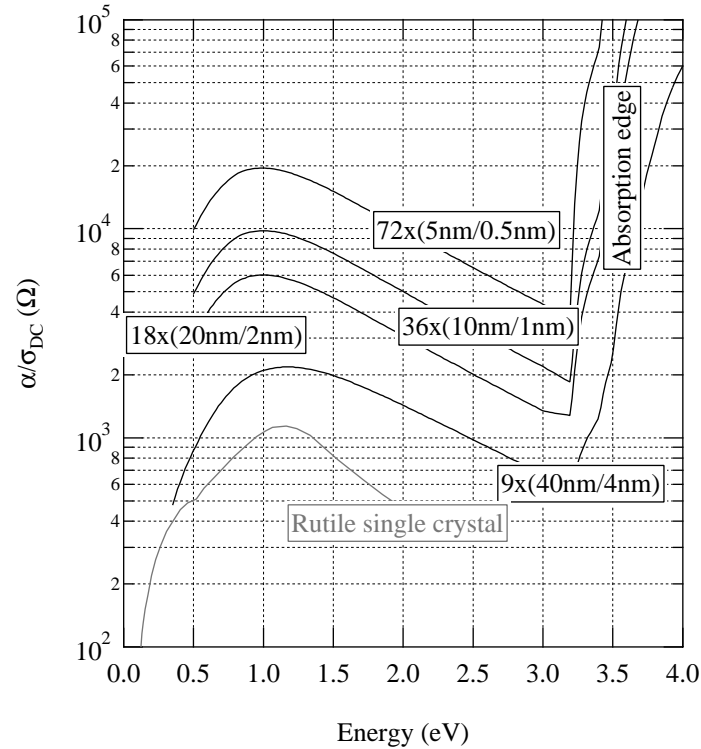


Figure 8.16: Normalized absorption coefficient α/σ_{DC} versus photon energy. The values for the rutile single crystal have been taken from literature [15].

As in Section 6.4.1 the charge carrier density was estimated from the absorption spectra assuming a constant ratio $\alpha_{max}/n = 9 \cdot 10^{-17} \text{ cm}^2$. This is based on the assumption that the absorption process was the same in the present samples as in the water-deposited samples of Chapter 6. The charge carrier density n compared well to that observed in Type B water-deposited films. It is put in relation to the deposition periods in Figure 8.17 (left). For longer periods the carrier density increased by a factor of 10 from $2.3 \cdot 10^{19}$ to $2.3 \cdot 10^{20} \text{ cm}^{-3}$. In parallel, the E_A values decreased from 130 to 105 meV (Figure 8.7). If a constant concentration of donor states was assumed and the activation energy would correspond to the donor ionization energy, this decrease in activation energy would explain an increase in carrier concentration by a factor of 2.4 only. Conversely, if the donor concentration is assumed to scale with σ_{DC} , the activation energy should show a stronger decrease. Nominally, the films discussed here had the same ratio of metal to oxide layer thickness. The increase in charge carrier density could be explained by an increasing amount of not completely oxidized Ti with longer sputtering periods. The activation energy of the DC conductivity is thus likely to reflect either the presence of intergrain potential barriers, or a thermally activated hopping mobility.

The effective DC electrical mobility μ_{DC} was calculated according to $\sigma_{DC} = n \cdot e \cdot \mu_{DC}$. It is reported on the right side of Figure 8.17. The mobility varied between $0.03 \text{ cm}^2 \text{ V}^{-1} \text{ s}^{-1}$ and $0.27 \text{ cm}^2 \text{ V}^{-1} \text{ s}^{-1}$ for longer deposition periods. Note that in parallel the grain size increased and the amorphous fraction decreased. The mobility values correspond to what has been reported in the literature ($0.01 \text{ cm}^2 \text{ V}^{-1} \text{ s}^{-1}$) for rutile with high defect concentration [17]. Potential barriers due to grain boundaries and the amorphous matrix contribute to the measured activation energy of σ_{DC} . The barrier height at grain boundaries in polycrystalline

semiconductors decreases with increasing carrier density [18, 19]. In the present samples a decrease in E_A was associated with an increase in the carrier density (Figure 8.7(right) and Figure 8.17(left)). These variations favor an increased effective mobility. An increase in the carrier density and the mobility in parallel explain the strong increase in σ_{DC} (2 orders of magnitude, Figure 8.7(left)) and the changes in the normalized absorption coefficient α/σ_{DC} (Figure 8.16).

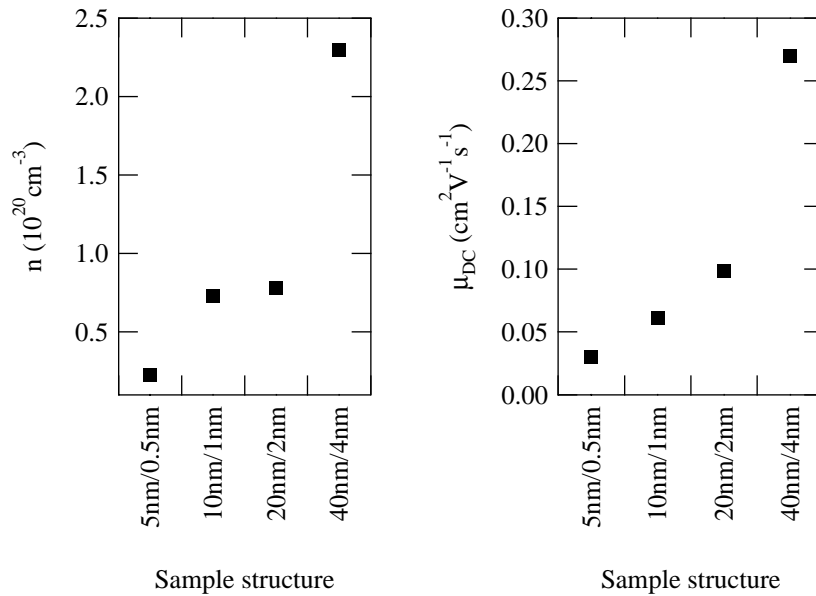


Figure 8.17: Charge carrier density n (left) and DC mobility μ_{DC} (right) versus sample structure. Values were determined from the absorption coefficient assuming a constant $\alpha_{max}/n = 9 \cdot 10^{-17} \text{ cm}^2$ (see Chapter 6 and [15, 16]).

Because of the rough backside of the Si substrates used for this series of samples, transmittance data were restricted to photon energies above 0.5 eV. Thus the occurrence of an additional small plasmonic absorption as it was found in water-deposited films of Type C (Chapter 6) at low energies could not be excluded. However, from the available transmittance measurements above 0.5 eV, the very low mobility, the elevated activation energy and the high α_{max}/σ_{DC} values no indication of the presence of metallic conductivity was found.

8.4.2 Periodicity in process parameters and nanostructure of the films

Because of the similarities in the shape, width and energy of the absorption band it is likely that it was of the same origin as the absorption observed in water-deposited samples in Chapter 6. The present films were deposited with oxygen as reactive gas and thus interstitial H is unlikely to be a potential source of donors. This supports the assumption that the role of water vapor in the reactive gas is of catalytic nature. With the pulsing of the oxygen supply a possibility has been found to achieve a doping level comparable to that in water-deposited films. But in the multilayered films the α_{max}/σ_{DC} ratio was higher, corresponding to a lower mobility. This was possibly due to smaller grains and the very high content in amorphous material.

It has been concluded in Chapter 7 that an important amount of a titanium interlayer between two dioxide layers is lost by oxidation and intermixing. The minimum amount of titanium necessary to form a continuous metallic layer was estimated to some 9 nm. Therefore one would not expect to find metallic layers in the samples discussed in this chapter with titanium equivalents of 4 nm and less. In cross-section TEM observations no layered structure could be clearly distinguished. Optical models taking TiO_2 and a stratified structure into account failed, whereas good fits were obtained with a homogeneous, TiO_{2-x} , model structure. This was also true for samples with thick periods ($9 \times (40\text{nm}/4\text{nm})$).

The suspension of the oxygen supply caused an interruption in the crystallite growth. This gives a tool to deposit films with different grain size and crystallinity. Grains found in the films of the present chapter were significantly smaller than those found in the single layered films (roughly 10 nm instead of 30 nm). Longer titanium deposition periods resulted in important modifications in the charge carrier mobility and density. These result in higher conductivity and an absorption band in the MIR. By the presented technique it was possible to obtain highly conducting and transparent samples. This is difficult to obtain by standard sputtering techniques by reducing the oxygen partial pressure during deposition. With oxygen as a reactive gas Bally et al. [20, 21] and Jeong et al. [22] reported either transparent, resistive titanium dioxide films or opaque and conducting samples films containing $\text{Ti}_n\text{O}_{2n-1}$ phases.

8.5 Conclusions

TiO_2 thin films intercalated with the equivalent of nanometer-thick layers of titanium were prepared by reactive magnetron sputtering. For depositing the titanium-rich layers, the O_2 reactive gas supply was periodically interrupted. The films contained nanometric rutile crystallites and an important amorphous fraction. The grain size changed with the period in reactive gas supply. The titanium was partially oxidized and filled up the voids between the TiO_2 grains. No evidence of a multilayer structure was found because the interface roughness was too large for the small amount of titanium.

Pulsing the reactive gas changed the grain size and modified the film properties. With longer Ti deposition periods the DC conductivity increased. Together with the higher charge carrier density an absorption band in the infrared appeared. The absorption band compares well with that observed in water-deposited films and is possibly of the same origin. The samples were highly conductive (up to 10^3 Sm^{-1}) and had a good transparency in the visible and infrared range. This was probably the first time that transparent, conductive TiO_2 films have been deposited by reactive magnetron sputtering using O_2 as reactive gas. The high carrier density (of the order of 10^{20} cm^{-3}) and the activation energy were very close to those of thin films of Type B prepared with water vapor as a reactive gas (Chapter 6). The periodicity in reactive gas supply not only influenced the morphology but also the charge carrier density and mobility, and therefore, the conductivity and optical properties of the samples. Thus the control of nanostructure seems to be of much importance for further research on titanium dioxide thin films.

References

1. A.T. Paxton and L. Thien-Nga, *Phys. Rev. B* **57** (1998), 1579.
2. T. Nakayama, *J. Electrochem. Soc.* **141** (1994), 237.
3. X. Orignac, H.C. Vasconcelos, X.M. Du, and R.M. Almeida, *Journal of Sol Gel Science and Technology* **8** (1997), 1.
4. E. Kusano, M. Kitagawa, H. Nanto, and A. Kinbara, *J. Vac. Sci. Technol. A* **16** (1998), 1272.
5. M.B. Daia, P. Aubert, S. Labdi, C. Sant, F.A. Sadi, P. Houdy, and J.L. Bozet, *J. Appl. Phys.* **87** (2000), 7753.
6. E. Kusano, A. Kinbara, and I. Kondo, *Journal of Non-Crystalline Solids* **218** (1997), 58.
7. N. Martin, A.R. Bally, P. Hones, R. Sanjinés, and F. Lévy, *Thin Solid Films* **377-378** (2000), 550.
8. F. Fabreguette, J. Guillot, L.P. Cardoso, R. Marcon, L. Imhoff, M.C. Marco de Lucas, P. Sibillot, S. Bourgeois, P. Dufour, and M. Sacilotti, *Thin Solid Films* **400** (2001), 125.
9. T. Chiamonte, L.P. Cardoso, R.V. Gelamo, F. Fabreguette, M. Sacilotti, M.C. Marco de Lucas, L. Imhoff, S. Bourgeois, Y. Kihn, and M.-J. Casanove, *Applied Surface Science* **212-213** (2003), 661.
10. M. Ohring, *Material science of thin films: Deposition and structure*. 2nd ed., Academic Press, San Diego (2002).
11. F. Bregani, C. Casale, L.E. Depero, I. Natali-Sora, D. Robba, L. Sangaletti, and G.P. Toledo, *Sensors and Actuators B* **31** (1996), 25.
12. *PDF-database*. JCPDS, International centre for diffraction data (ICDD), 1601 Park Lane, Swarthmore, PA 19081, USA.
13. B.I. Shklovskii and A.L. Efros, *Electronic properties of doped semiconductors*. Springer Verlag, Berlin (1984).
14. O. Banakh, P.E. Schmid, R. Sanjinés, and F. Lévy, *Surface and Coatings Technology* **151-152** (2002), 272.
15. D.C. Cronmeyer, *Phys. Rev.* **113** (1959), 1222.
16. R.G. Breckenridge and W.R. Hosler, *Phys. Rev.* **91** (1953), 793.
17. Z.M. Jarzelski, *Oxide Semiconductors*. Permagon Press, (1973).
18. J.W. Orton and M.J. Powell, *Rep. Prog. Phys.* **43** (1980), 1263.
19. V. Demarne and R. Sanjinés, *Thin film semiconducting metal oxide gas sensors*, in *Gas sensors: Principles, Operation and Developments*, G. Sberveglieri (Editor). Kluwer Academic Publishers, Dordrecht, Boston, London (1992).
20. A.R. Bally, P. Hones, R. Sanjinés, P.E. Schmid, and F. Lévy, *Surface and Coatings Technology* **108-109** (1998), 166.
21. A. Bally, *Electronic properties of nano-crystalline titanium dioxide thin films*. Département de physique, Ecole polytechnique fédérale de Lausanne EPFL, Lausanne (1999).
22. B.-S. Jeong, D.P. Norton, and J.D. Budai, *Solid-State Electronics* **47** (2003), 2275.

Chapter 9 **Conclusions**

Highly doped titanium dioxide thin films were deposited by reactive magnetron sputtering using water vapor as reactive gas or a pulsed oxygen supply. The films exhibited mixtures of polycrystalline anatase, polycrystalline rutile and amorphous phases with crystallite sizes in the 10 to 50 nm range. The focus was set on transparent samples close to stoichiometric composition.

Several modifications of reactive sputtering were used. One arrangement consisted in using water vapor as reactive gas instead of oxygen. In a second arrangement the oxygen supply was interrupted periodically. As a result the crystalline phase composition, the crystallite size and the density of oxygen defects were modified. The changes influenced directly macroscopic properties such as optical absorption and electrical conductivity.

The link between macroscopic properties and the nanostructure was established with optical models. They were based on effective medium approximations combining the bulk properties of anatase and rutile. The optical anisotropy of anatase and rutile was accounted for according to the preferential orientation of the crystallites. The morphology of the films was modelled by choosing an appropriate effective medium approximation. Structural characterization of the samples helped to restrict the range and number of the modelling parameters. Optical absorption due to substoichiometry was accounted for by Drude and Lorentzian oscillators.

When working with water vapor, an increasing absorption band appeared in the mid-infrared with decreasing H₂O partial pressure. It was matched by increasing electrical conductivity. Good fits to the optical spectra were achieved by introducing a Lorentzian-shaped absorption band. The charge carrier density was of the order of 10^{19} cm^{-3} and the carrier mobility was approximately $0.2 \text{ cm}^2 \text{ V}^{-1} \text{ s}^{-1}$. Models accounting for the electrical and optical properties have been proposed. The absorption band could be assigned to polaronic absorption or to variable range hopping between impurity states in rutile. Due to a lack of experimental evidence and controversial theoretical models the question remains open.

Water-deposited films containing anatase struck by a low IR absorption ($3 \cdot 10^3 \text{ cm}^{-1}$) in parallel with a high electrical conductivity in the order of $1'000 \text{ Sm}^{-1}$, and a low activation energy of roughly 30 meV. This behavior occurred in parallel with the appearance of a weak plasmonic absorption at low photon energies. It was attributed to free electrons in anatase. Films with such unusual behavior have been observed only when water vapor was used for the deposition. This evokes the important question of the influence of the reactive gas. Water vapor in the plasma is believed to act as catalyst for the reduction of the grain boundaries. In addition, hydrogen interstitials could act as donors. To the detection limit of 0.5 at% no hydrogen was found in the films. However, a doping level as low as 0.1 at% would be enough to account for the observed free electron density.

Strong interface reactions and intermixing was observed when depositing titanium on top of titanium dioxide or vice versa. A fixed amount of the titanium was oxidized, whereas the neighboring titanium dioxide was reduced. When the oxygen supply was stopped periodically, the crystallite growth was interrupted. This gives the possibility for inserting

additional oxygen defects and modifying the sample morphology and in consequence its electrical and optical properties.

For longer periods in the oxygen supply the grain size and the degree of crystallinity increased. In parallel the charge carrier density, the mobility and thus the conductivity increased. The electrical and optical properties of these samples compared to those of water-deposited films devoid of anatase. A broad absorption band in the mid-infrared was possibly of the same origin as the band observed for the water-deposited films. Due to a smaller grain size and an important amorphous component the mobility of the carriers was lower than in the water-deposited films. The similarities with the water-deposited films, and the fact that in these sample series no hydrogen was added to the process, support the hypothesis that the role of hydrogen is mainly catalytic. This was the first time that transparent TiO_{2-x} films sputter-deposited with oxygen showed an electrical conductivity as high as in the case of TiO_{2-x} deposited with water vapor.

The combination of relative high hardness, chemical resistance, transparency and conductivity, and the ease of their preparation by sputtering makes highly doped TiO_{2-x} films interesting for technological applications. Favoring the presence of anatase in the films was found to be the critical factor leading to both high conductivity and high electron mobility.

Appendix A Optical properties of a stratified medium

The most important reference for the following summary was the book of Azzam and Bashra [1]. For the matrix formalism see also [2-4]. The description of the optical properties of anisotropic media is treated by F. Pockels [5]. See also [6] and [7].

The time dependence for the harmonic field has been chosen to follow $\exp(i\omega t)$. Accordingly, the complex index of refraction is $N = n - ik$ where n is the index of refraction and $k \geq 0$ is the extinction coefficient of the material. The complex dielectric function is $\varepsilon = \varepsilon_1 - i\varepsilon_2$ with $\varepsilon_2 \geq 0$. N and ε are functions of the photon energy $\hbar\omega$. They are related to each other by $\varepsilon = N^2$ or $N = \varepsilon^{1/2}$, i.e. the square root of ε which has a positive real part [6, 8].

$$\text{Equation A.1} \quad \varepsilon_1 = n^2 - k^2 \quad \varepsilon_2 = 2nk$$

$$\text{Equation A.2} \quad n = \left[\frac{1}{2} \left(\sqrt{\varepsilon_1^2 + \varepsilon_2^2} + \varepsilon_1 \right) \right]^{1/2} \quad k = \left[\frac{1}{2} \left(\sqrt{\varepsilon_1^2 + \varepsilon_2^2} - \varepsilon_1 \right) \right]^{1/2}$$

A.1 Definitions

We consider a stratified system of layers j in an ambient a . Hereafter the following definitions are used.

ε_a	dielectric function of the isotropic ambient
N_a	index of refraction of the isotropic ambient
φ_a	angle of incidence in the isotropic ambient
λ_a	wavelength of the light in the ambient ($= 2\pi c / (N_a \omega)$, where c is the light velocity and $\hbar\omega$ is the photon energy)
ε_j	complex dielectric function of layer j
N_j	complex index of refraction of layer j
φ_j	angle of propagation in the layer j
d_j	thickness of layer j

From Snell's law of refraction $N_a \sin \varphi_a = N_j \sin \varphi_j$ a constant is defined

$$\text{Equation A.3} \quad S := N_j \sin \varphi_j \quad \text{or} \quad S^2 := \varepsilon_j \sin^2 \varphi_j$$

for all layers j . Snell's constant S can readily be calculated for the ambient with ε_a , and the incidence angle φ_a . S corresponds to the transverse projection of the wave vector. For the forward projection of the wave vector \vec{k} we define

$$\text{Equation A.4} \quad \gamma_j := N_j \cos \varphi_j = \sqrt{\varepsilon_j - S^2}$$

The phase thickness of layer j is defined as

$$\text{Equation A.5} \quad \delta_j := \frac{2\pi}{\lambda_a} \cdot d_j$$

A.2 Fresnel coefficients for reflection and transmission at a planar interface between isotropic media

Any arbitrary polarization of an electromagnetic plane wave can be decomposed in p- and s-components normal to each other. The p-component (from German 'parallel') is defined to be parallel and the s-component (from 'senkrecht') to be perpendicular to the scattering plane, respectively [6]. For the two polarizations s and p the ratios of the incident and reflected complex amplitudes (E_{is} and E_{rs} , or E_{ip} and E_{rp}) or incident and transmitted complex amplitudes (E_{is} and E_{ts} , E_{ip} and E_{tp}) at an interface are called Fresnel coefficients for the respective polarization. For the plane interface between the isotropic layers 0 and 1 they are given as [1], pp. 271, 272

$$\text{Equation A.6} \quad r_{01,p} := \frac{E_{rp}}{E_{ip}} = \frac{N_1 \cos \varphi_0 - N_0 \cos \varphi_1}{N_1 \cos \varphi_0 + N_0 \cos \varphi_1} = \frac{\gamma_{0,p} - \gamma_{1,p}}{\gamma_{0,p} + \gamma_{1,p}}$$

$$\text{Equation A.7} \quad r_{01,s} := \frac{E_{rs}}{E_{is}} = \frac{N_0 \cos \varphi_0 - N_1 \cos \varphi_1}{N_0 \cos \varphi_0 + N_1 \cos \varphi_1} = \frac{\gamma_{0,s} - \gamma_{1,s}}{\gamma_{0,s} + \gamma_{1,s}}$$

$$\text{Equation A.8} \quad t_{01,p} := \frac{E_{tp}}{E_{ip}} = \frac{2N_0 \cos \varphi_0}{N_1 \cos \varphi_0 + N_0 \cos \varphi_1} = \frac{2\gamma_{0,p}}{\gamma_{0,p} + \gamma_{1,p}}$$

$$\text{Equation A.9} \quad t_{01,s} := \frac{E_{ts}}{E_{is}} = \frac{2N_0 \cos \varphi_0}{N_0 \cos \varphi_0 + N_1 \cos \varphi_1} = \frac{2\gamma_{0,s}}{\gamma_{0,s} + \gamma_{1,s}}$$

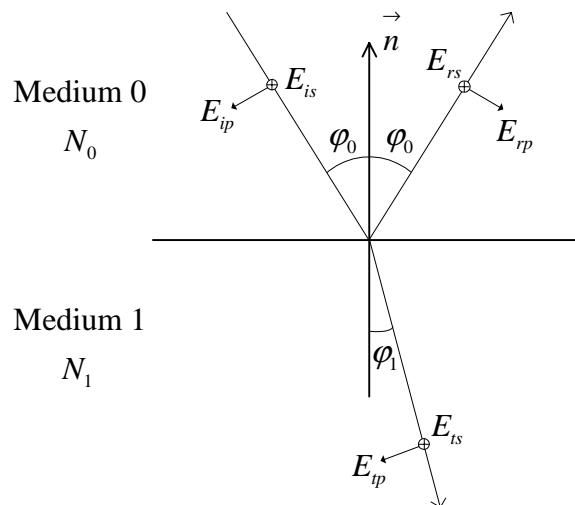


Figure A.1: Oblique reflection and transmission of a plane wave at the planar interface between two semi-infinite and isotropic media 0 and 1 [1].

A.3 Fresnel coefficients for reflection and transmission at a planar interface perpendicular to the optical axis of two uniaxial media

The definitions given so far concern isotropic layers. The optical properties of a homogeneous film are uniaxial with the optical axis perpendicular to the layer plane. Therefore a distinction between ordinary (in the layer plane, perpendicular to optical axis) and extraordinary (perpendicular to layer plane, parallel to optical axis) film properties is necessary. The corresponding independent complex dielectric functions are:

$$\begin{aligned}\varepsilon_{j,o} & \text{ ordinary complex dielectric function of layer } j \\ \varepsilon_{j,e} & \text{ extraordinary complex dielectric function of layer } j\end{aligned}$$

For a p-polarized plane wave propagating in an uniaxial layer j at an angle φ_j from the axis the value of the dielectric function ε_p is a function of the direction of propagation. It is given by

$$\text{Equation A.10} \quad \frac{1}{\varepsilon_p} = \frac{\cos^2 \varphi_j}{\varepsilon_{j,o}} + \frac{\sin^2 \varphi_j}{\varepsilon_{j,e}}$$

or with Snell's constant S

$$\text{Equation A.11} \quad \varepsilon_p = \varepsilon_{j,o} + S^2 \left(1 - \frac{\varepsilon_{j,o}}{\varepsilon_{j,e}}\right)$$

see [6] p. 60 and [7] p. 341. For the corresponding s-polarized beam ε_s is independent of the direction of propagation: $\varepsilon_s = \varepsilon_{j,o}$. The forward projection γ_j of the wave vector, in a uniaxial layer j is given by

$$\text{Equation A.12} \quad \gamma_{j,s} := \sqrt{\varepsilon_{j,o} - S^2} \qquad \gamma_{j,p} := \sqrt{\varepsilon_{j,o} - \frac{\varepsilon_{j,o}}{\varepsilon_{j,e}} S^2}$$

The Fresnel coefficients for reflection at the interface between two uniaxial layers j and $(j+1)$ are

$$\text{Equation A.13} \quad r_{j(j+1),s} = \frac{\gamma_{j,s} - \gamma_{(j+1),s}}{\gamma_{j,s} + \gamma_{(j+1),s}} \qquad r_{j(j+1),p} = \frac{\frac{\gamma_{j,p}}{\varepsilon_{j,o}} - \frac{\gamma_{(j+1),p}}{\varepsilon_{(j+1),o}}}{\frac{\gamma_{j,p}}{\varepsilon_{j,o}} + \frac{\gamma_{(j+1),p}}{\varepsilon_{(j+1),o}}}$$

The corresponding Fresnel coefficients for transmission are

$$\text{Equation A.14} \quad t_{j(j+1),s} = 1 + r_{j(j+1),s} \qquad t_{j(j+1),p} = (1 + r_{j(j+1),p}) \cdot \sqrt{\frac{\varepsilon_{j,o}}{\varepsilon_{(j+1),o}}}$$

A.4 Matrix formalism for a stratified medium

A matrix formalism has been used for the calculation of the optical response of a stack of layers. It was proposed by Abelès [9], and Hayfield and White [2] and has been expanded by Azzam and Bashara [1]. For the anisotropic case in particular see [1] pp. 356, [3, 4]. Hereafter we assume uniaxial symmetry. When the incident wave in the ambient is either p- or s-polarized, the excited waves in the uniaxial layers will possess the same polarization, i.e. p or s, respectively [1]. Thus each polarization can be treated independently and the indices p and s have been omitted. $E^+(z)$ and $E^-(z)$ denote the complex amplitudes of the forward- and backward-travelling plane waves at distance z in propagation direction. The total field at z can be described by a 2×1 -column vector

$$\text{Equation A.15} \quad E(z) = \begin{bmatrix} E^+(z) \\ E^-(z) \end{bmatrix}$$

The fields at two different locations z' and z'' are then related by a linear 2×2 -matrix transformation

$$\text{Equation A.16} \quad \begin{bmatrix} E^+(z') \\ E^-(z') \end{bmatrix} = \begin{bmatrix} M_{11} & M_{12} \\ M_{21} & M_{22} \end{bmatrix} \begin{bmatrix} E^+(z'') \\ E^-(z'') \end{bmatrix} \quad \text{or} \quad E(z') = ME(z'')$$

The scattering matrix M describes a multilayer, which is composed of m layers and is in the ambient a . It is given as a product of interface and layer matrices $I_{(j-1)j}$ and L_j , respectively:

$$\text{Equation A.17} \quad M = I_{a1} L_1 I_{12} \dots I_{(m-1)m} L_m I_{ma}$$

The interface matrices $I_{j(j+1)}$ contain the Fresnel coefficients $r_{j(j+1)}$ and $t_{j(j+1)}$ (Equations A.6 to A.9 for isotropic layers or Equations A.13 and A.14 for uniaxial layers) for reflection and transmission at the interface between layers j and $j+1$.

$$\text{Equation A.18} \quad I_{j(j+1),s} := \frac{1}{t_{j(j+1),s}} \begin{bmatrix} 1 & r_{j(j+1),s} \\ r_{j(j+1),s} & 1 \end{bmatrix} \quad I_{j(j+1),p} := \frac{1}{t_{j(j+1),p}} \begin{bmatrix} 1 & r_{j(j+1),p} \\ r_{j(j+1),p} & 1 \end{bmatrix}$$

The absorption and phase change in layer j is taken into account in the corresponding layer matrices L_j .

$$\text{Equation A.19} \quad L_{j,s} := \begin{bmatrix} e^{i\gamma_{j,s}\delta_j} & 0 \\ 0 & e^{-i\gamma_{j,s}\delta_j} \end{bmatrix} \quad L_{j,p} := \begin{bmatrix} e^{i\gamma_{j,p}\delta_j} & 0 \\ 0 & e^{-i\gamma_{j,p}\delta_j} \end{bmatrix}$$

When the thickness d_j of one layer is set equal to zero, the corresponding layer matrix equals the unit matrix. The multiplication of the remaining adjacent interface matrices results in the corresponding interface matrix of the new interface.

For either polarization the overall reflection and transmission coefficients r_s , r_p , t_s , t_p are contained in the scattering matrix M [1]:

$$\text{Equation A.20} \quad r = \frac{M_{21}}{M_{11}} \quad \text{and} \quad t = \frac{1}{M_{11}}$$

Reflectance R and transmittance T are given for either polarization by the square of the moduli of the reflection and transmission coefficients

$$\text{Equation A.21} \quad R = |r|^2 \quad \text{and} \quad T = |t|^2$$

References

1. R.M.A. Azzam and N.M. Bashara, *Ellipsometry and polarized light*. 1st ed., North-Holland publishing company, Amsterdam, New York, Oxford (1977).
2. P.C.S. Hayfield and G.W.T. White, in *Ellipsometry in the Measurement of Surfaces and Thin Films*, E. Passaglia, R.R. Stromberg, and J. Kruger (Editors). Natl. Bur. Std. Misc. Publ. 256, US Government Printing Office, Washington DC (1964).
3. S. Teitler and B.W. Hennis, *Journal of the Optical Society of America* **60** (1970), 830.
4. G.E. Jellison, Jr., *Thin Solid Films* **234** (1993), 416.
5. F. Pockels, *Lehrbuch der Kristalloptik*. B.G. Teubner, Leipzig (1906).
6. M. Born and E. Wolf, *Principles of Optics*. 6th ed., Pergamon Press, Oxford, New York (1980).
7. L.D. Landau, E.M. Lifshitz, and L.P. Pitaevskii, *Electrodynamics of continuous media*. 2nd ed., Pergamon Press, Oxford (1984).
8. A. Sadao, *Optical properties of crystalline and amorphous semiconductors: materials and fundamental principles*. Kluwer Academic Publishers, Norwell (1999).
9. F. Abelès, *Ann. de Physique* **5** (1950), 596.

Appendix B Dielectric function of heterogeneous media

If the characteristic size of the inhomogeneities is smaller than the wavelength of the light and larger than the mean free path of the electrons, the effective medium approximations (EMA) can be used. They propose that the dielectric function ϵ_{eff} of a heterogeneous system is a function of the dielectric functions ϵ_i of the constituents i , of their volume fractions f_i (with $\sum f_i = 1$) and of the morphology [1, 2]. Corresponding to a maximum energy of 4.5 eV the shortest wavelength we were interested in was 275 nm, whereas our grains are no larger than 50 nm. The most frequently used EMA are presented below. A review of effective medium approximations has been published by D.E. Aspnes [2].

In the case of materials consisting of plates or cylinders parallel to the electric field the formula corresponds to capacitors connected in parallel [2].

Equation B.1
$$\epsilon_{eff} = \sum_i f_i \epsilon_i$$

Plates perpendicular to the electric field correspond to capacitors connected in series [2].

Equation B.2
$$\frac{1}{\epsilon_{eff}} = \sum_i \frac{f_i}{\epsilon_i}$$

The Maxwell-Garnett (MG) theory [3, 4] models spherical inclusions of materials i embedded in a matrix of material m [2, 5]. The model considers that the inclusions have no virtual interactions. Therefore, this approximation is best for small f_i . The effective dielectric function ϵ_{eff} is given by

Equation B.3
$$\frac{\epsilon_{eff} - \epsilon_m}{\epsilon_{eff} + 2\epsilon_m} = \sum_i f_i \frac{\epsilon_i - \epsilon_m}{\epsilon_i + 2\epsilon_m}$$

An analytic representation of ϵ_{eff} has been derived by D.J. Bergman [6] and has been further discussed in [1, 7]. For grains of material A in a matrix B it is

Equation B.4
$$\epsilon_{eff} = \epsilon_B + \frac{Df_A\epsilon_B(\epsilon_A - \epsilon_B)}{D\epsilon_B + (1 - f_A)(\epsilon_A - \epsilon_B)}$$

where D indicates the 'dimensionality' of the geometry. Accordingly, $D = 2$ stands for columns perpendicular to the electric field, $D = 3$ stands for spheres, and intermediate values for elliptically shaped grains. For large filling factors the same equation applies for grains of material A covered by a thin shell of B .

If the layer material is more intermixed, the self-consistent Bruggeman EMA [8] is more appropriate [5]. This model is self-consistent, i.e. it considers grains of constituents i to be dispersed in the effective medium itself.

Equation B.5

$$0 = \sum_i f_i \frac{\epsilon_i - \epsilon_{eff}}{\epsilon_i + 2\epsilon_{eff}}$$

The Bruggeman approximation is expected to apply best for $f_i \approx 0.5$ [2, 5].

References

1. G.W. Milton, *Applied Physic Letters* **37** (1980), 300.
2. D.E. Aspnes, *Thin Solid Films* **89** (1982), 249.
3. J.C.M. Garnett, *Philosophical Transactions of the Royal Society of London* **203** (1904), 385.
4. J.C.M. Garnett, *Philosophical Transactions of the Royal Society of London A* **205** (1906), 237.
5. G.E. Jellison, Jr., *Thin Solid Films* **234** (1993), 416.
6. D.J. Bergman, *Physics Letters C: Physics Reports* **43** (1978), 377.
7. D.J. Bergman, *Physical Review Letters* **44** (1980), 1285.
8. D.A.G. Bruggemann, *Annalen der Physik* **24** (1935), 636.

Appendix C Modelling the dielectric function of a solid

The dielectric function ε of a crystal compatible with a band structure can be expressed as the sum of complex susceptibilities associated with intraband, interband and core level transitions

$$\text{Equation C.1} \quad \varepsilon = 1 + \chi_{inraband} + \chi_{interband} + \chi_{core}$$

The function $\chi_{interband}$ can be obtained from bandstructure calculations. It can be conveniently represented by a sum of Lorentzians [1-3]:

$$\text{Equation C.2} \quad \chi_{interband}(\omega) = \sum_l \frac{f_l \omega_l^2}{\omega_l^2 - \omega^2 + i\gamma_l \omega}$$

A Lorentzian oscillator represents a damped oscillation with resonance frequency ω_l , damping term γ_l and oscillator force f_l . The resonance frequency ω_l is the transition frequency of an electron between two states separated by the energy $\hbar\omega_l$, whereas f_l is the relative probability of such a transition. The intraband susceptibility $\chi_{inraband}$ is often modelled by a Drude term [1, 4] in the high energy limit. In the optical energy range it is often successful, too [2].

$$\text{Equation C.3} \quad \chi_{inraband}(\omega) = -\frac{\omega_p^2}{\omega(\omega - i\gamma_p)}$$

The plasma frequency ω_p is defined by

$$\text{Equation C.4} \quad \omega_p^2 := \left(\frac{n}{m}\right)_{eff} \cdot \frac{e^2}{\varepsilon_0} \approx \frac{n \cdot e^2}{\varepsilon_0 \cdot m^*}$$

The second part of the equation is true in the case of a semiclassical model for a single spherical band, where n is the free electron density and m^* the effective mass of the electron. The damping term γ_p is defined as the inverse of the mean free time τ between collisions

$$\text{Equation C.5} \quad \gamma_p := \frac{1}{\tau}$$

One can define a complex optical conductivity [5]

$$\text{Equation C.6} \quad \sigma = \sigma_1 + i\sigma_2 := i\varepsilon_0 \varepsilon \omega$$

In the discussions in Chapters 6 through 8 only the real part $\sigma_l = -\epsilon_0 \epsilon_2 \omega$ is used. It is termed 'optical conductivity' σ_{opt} . In the case of a semiclassical free electron gas it is for $\omega \rightarrow 0$

Equation C.7

$$\sigma_{opt}(\omega \rightarrow 0) = \left(\frac{n}{m} \right)_{eff} \cdot \frac{e^2}{\gamma_p} \approx \frac{\epsilon_0}{\gamma_p} \cdot \omega_p^2$$

Again, the second part is the semiclassical single spherical band expression. With $\sigma = ne\mu$ one obtains for the semiclassical single spherical band assumption the optical mobility as

Equation C.8

$$\mu_{opt} = \frac{e}{\gamma_p \cdot m^*}$$

where e is the charge of the electron and m^* is the effective mass of the charge carrier.

References

1. F. Wooten, *Optical properties of solids*. 1st ed., Academic Press, New York, London (1972).
2. J.D. Jackson, *Klassische Elektrodynamik*. 2nd ed., Walter de Gruyter, Berlin, New York (1983).
3. M. Born and E. Wolf, *Principles of Optics*. 6th ed., Pergamon Press, Oxford, New York (1980).
4. P. Drude, *Z. Phys.* **1** (1900), 161.
5. A. Sadao, *Optical properties of crystalline and amorphous semiconductors: materials and fundamental principles*. Kluwer Academic Publishers, Norwell (1999).

Appendix D Optical modelling of the substrates

In Figure D.1 the transmittance spectra of oxidized silicon and glass substrates are presented. General substrate properties can be found in Table 3.1. On occasion a 100 nm thick amorphous SiO₂ layer was present on the front and back side of the Si substrate. The thermal silicon oxide thickness was measured by ellipsometry on a bare substrate. Reference data for Si and SiO₂ have been taken from Palik [1]. The 100 nm SiO₂ layers on the front and back side of the Si substrates would have their first interference maximum at 4.5 eV, i.e. they added a slope to the IR range where our measurements have been performed (Figure D.1). The optical constants of the microscope slides used as glass substrates have been determined by Dr. G. Bader of the University of Moncton in Canada by ellipsometry in transmission. The glass properties have been found to be close to 'borosilicate crown glass' with $n = 1.63$, $k = 1.2 \cdot 10^{-5}$ at 300 nm and $n = 1.50$, $k = 1.0 \cdot 10^{-6}$ at 800 nm. The corresponding dielectric function is shown in Figure D.2.

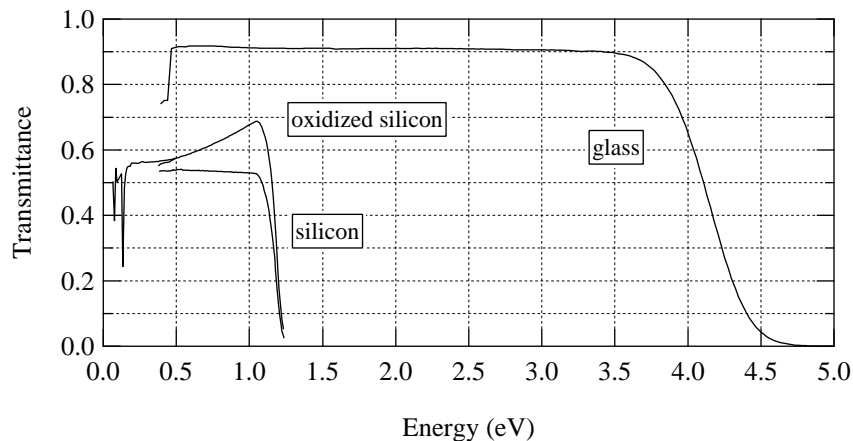


Figure D.1: Transmittance spectra of silicon, thermally oxidized silicon and glass substrates. The silicon substrates were polished on both sides.

Our 500 μm thick Si substrates, as well as our microscope slides, had a flatness not better than 1 μm . This was the main reason for the absence of interference effects in the optical response of the substrates. Accordingly, the optical model calculated the substrate contributions to the optical response in terms of intensities rather than in terms of field amplitudes. The system we were interested in consisted of a substrate (medium 1) intercalated between a medium 0 and a medium 2. Medium 0 and 2 can for instance consist in the ambient, roughness layers, and a thin film. Their properties are accounted for in the overall Fresnel coefficients for the 01 (r_{01} for reflection and t_{01} transmission) and the 12 interfaces (r_{12} , t_{12}). They are obtained from Equations A.13 and A.14. For the waves traveling from the substrate towards medium 0 the Fresnel coefficients are given as $r_{10} := -r_{01}$ and $t_{10} := (1 - r_{01}^2) / t_{01}$ [2] p. 283. Addition of the intensities of the multiply reflected partial waves leads to an infinite geometric series for reflectance and transmittance. The summation of the series gives

$$\text{Equation D.1} \quad \text{Reflectance} = |r_{01}|^2 + \frac{|t_{01}r_{12}t_{10}|^2 A^2}{1 - |r_{10}r_{12}|^2 A^2}$$

$$\text{Equation D.2} \quad \text{Transmittance} = \frac{|t_{01}t_{12}|^2 A}{1 - |r_{10}r_{12}|^2 A^2}$$

where $A := |\exp(-i\gamma_1\delta_1)|^2$ accounts for the absorption in medium 1, i.e. in the substrate (definitions for γ and δ see Equations A.4 and A.5). Also see [2] on p. 285. This approach suppressed the phase information and therefore the interferences inside the substrate.

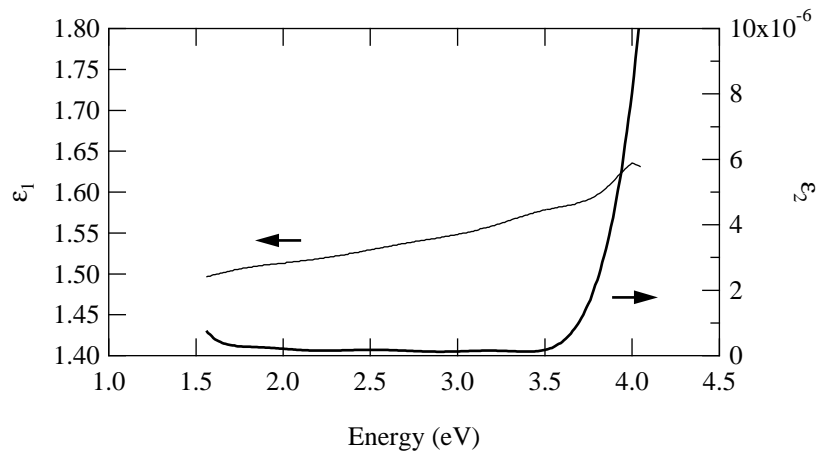


Figure D.2: Dielectric function of the glass substrates.

References

1. E.D. Palik, *Handbook of Optical Constants of Solids*. Academic Press, Orlando (1985).
2. R.M.A. Azzam and N.M. Bashara, *Ellipsometry and polarized light*. 1st ed., North-Holland publishing company, Amsterdam, New York, Oxford (1977).

Appendix E X-ray reflectivity

Since this technique is relatively young and has not been established in our group the present appendix contains a summary of the basic concepts of this method. Comprehensive review articles on grazing incidence X-ray reflectometry (XRR) have been published by E. Chason and T.M. Mayer [1], and N. Stoev and K. Sakurai [2]. O. Durand [3] and J. Als-Nielsen and D. McMorrow [4] present good introductions to specular reflectivity. The recent books of V. Holý et al. [5], and J. Daillant and A. Gibaud [6] discuss scattering theory, possible machine configurations and the analysis of specular and diffuse X-ray reflectivity on rough multilayer samples. If not indicated otherwise, the concepts introduced hereafter can be found in these references. An example of XRR measurements on titanium dioxide samples has been published by Aspelmeyer et al. [7].

E.1 Basic concepts of X-ray reflectivity

E.1.1 Geometry of the experiment

If the direction of an incident plane wave is described by its wave vector \vec{K}_i (see Figure E.1) and that of the scattered plane wave by its wave vector \vec{K}_f , the scattered intensity can be expressed as a function of the scattering vector

$$\text{Equation E.1} \quad \vec{Q} = \vec{K}_f - \vec{K}_i$$

The direction of \vec{Q} with respect to the sample surface determines the direction in which structural information is obtained. Q defines the length scale $2\pi/Q$ of the measurement. For coplanar diffraction geometries, the vectors of the incident and diffracted beams \vec{K}_i and \vec{K}_f and the surface normal \vec{n} lie in the common scattering plane. The length of each vector is

$$\text{Equation E.2} \quad K = \frac{2\pi}{\lambda}$$

which is in the present work $K = 4.0784 \text{ \AA}^{-1}$ for $\lambda(\text{Cu } K_{\alpha 1}) = 0.15406 \text{ nm}$. In the sample coordinate system the z -axis is parallel to the outward surface normal and the xz -plane coincides with the scattering plane. The incidence angle α_i and the exit angle α_f are defined as the angles between the beam and the sample surface (see Figure E.1). As an alternative coordinate system the scattered intensity can be described by its distribution in reciprocal space. When the reciprocal-lattice vectors of the specimen are aligned with the sample system

the components q_x , q_y , and q_z of the scattering vector \vec{Q} are

$$q_x := K(\cos \alpha_f \cos X - \cos \alpha_i)$$

Equations E.3

$$q_y := K \cos \alpha_i \sin X$$

$$q_z := K(\sin \alpha_i + \sin \alpha_f)$$

where X is the angle between the scattering plane and the sample normal (definition of the goniometer axes see Figure 4.1). XRR measurements are often performed in coplanar geometry and $X = 0$. In the case of specular reflectivity (i.e. $\alpha_i = \alpha_f$) Equations E.3 reduce to

$$q_x = 0$$

Equations E.4

$$q_y = 0$$

$$q_z = 2K \sin \alpha_i$$

On the goniometer the rotation of the sample was denoted by Ω and that of the detector by 2Θ , corresponding to the scattering angle between incident and reflected beam.

Equation E.5

$$\Omega := \alpha_i$$

Equation E.6

$$2\Theta := \alpha_i + \alpha_f$$

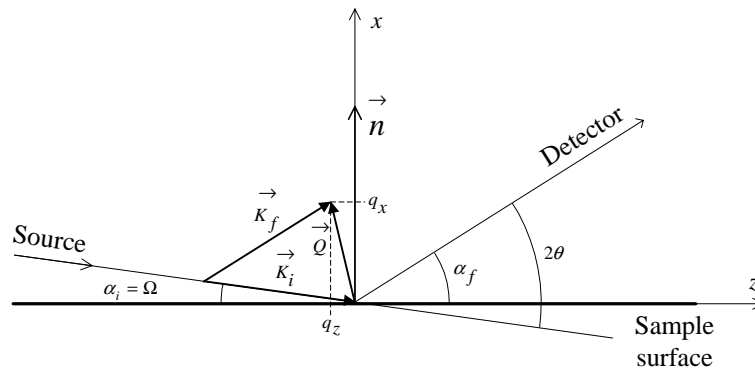


Figure E.1: Incident and scattered wave vectors in the sample and reciprocal space coordinates. Also see Figure 4.1 on p. 24 for the definition of the diffractometer axes.

E.1.2 Refractive index in the X-ray range

In the X-ray region of the spectrum, the index of refraction is obtained from the classical theory of dispersion [2 and references therein]. The complex refractive index n can be written as

$$\text{Equation E.7} \quad n = 1 - \frac{2\pi R_e \rho_a}{K^2} \{f^0 + f' + if''\}$$

where λ is the wavelength of the X-rays, ρ_a is the atomic density, and R_e is the classical

Thomson radius of the electron. It is given by

$$\text{Equation E.8} \quad R_e = \frac{e^2}{4\pi\epsilon_0 m_e c^2} = 2.8179 \cdot 10^{-5} \text{ \AA}$$

where e is the elementary electronic charge and m_e is the mass of the electron [8]. $\{f^0 + f' + i f''\}$ is the atomic scattering factor with dispersion corrections. The atomic scattering factor equals the atomic number: $f^0 = Z$. The complex dispersion correction $f' + i f''$ accounts for the fact that the scattering power of a bound electron is different from that of a free electron as assumed for f^0 . If we introduce

$$\text{Equation E.9} \quad \delta := \frac{2\pi R_e \rho_a}{K^2} \{f^0 + f'\}$$

and

$$\text{Equation E.10} \quad \beta := -\frac{2\pi R_e \rho_a}{K^2} f''$$

for the imaginary part, Equation E.7 can be written as

$$\text{Equation E.11} \quad n = 1 - \delta + i\beta$$

The real term δ is associated with the dispersion, while the imaginary term β is associated with the absorption of X-rays⁹. δ and β are small quantities in the order of 10^{-8} to 10^{-5} . The real part of the refractive index is smaller than unity for most elements in the X-ray region away from the absorption edges. This means that for incidence angles smaller than a critical angle α_c the X-ray radiation experiences a total external reflection at the sample surface. From Snell's law it can be shown that the critical angle α_c is related to the index n by

$$\text{Equation E.12} \quad \alpha_c = \sqrt{2\delta}$$

The critical wave-vector transfer is then

$$\text{Equation E.13} \quad q_c = 2K \sin \alpha_c$$

E.1.3 Specular and diffuse scans

Off-specular scans ($\alpha_i \neq \alpha_f$) allow measuring the diffuse scattering. This gives information on the horizontal and vertical structure of the interface, such as correlation length and fractal dimensions, and a distinction between rough and interdiffused interfaces. Table E.1 contains a summary of possible scans and the corresponding terms that are used in literature and diffractometer software. As reported in columns two and three of the table the scanning movements can easily be described in goniometer and sample coordinate systems. From the rocking curve the level of diffuse scattering can be determined. The width of the specular peak in the rocking curve gives an indication of the offset $\Delta\alpha$ that needs to be chosen for the offset scan. Usually $\Delta\alpha$ was about 0.05° . In the rocking curves taken at different 2Θ angles the specular peak width should be constant and roughly twice as large as the direct beam in a 2Θ -scan. If this is not the case the sample curvature needs to be accounted for. Offset scans were performed to determine the diffusely scattered intensity. Rocking and detector scans were used for the alignment of the sample.

⁹ The absorption coefficient μ is defined as $\mu := 4\pi\beta/\lambda$.

Scan	Goniometer	Sample	Reciprocal space	Information
Specular scan 2:1 absolute scan	$2 \cdot \Omega = 2\theta$	$\alpha_i = \alpha_f$	$q_x = \text{const.}$, scan q_z scattering vector \perp to surface plane	layer thicknesses, densities and roughnesses
Offset scan Longitudinal scan Diffuse-near-specular scan 2:1 relative scan	$2 \cdot \Omega + \Delta\alpha = 2\theta$ ($\Delta\alpha \approx \pm 0.05^\circ$)	$\alpha_i + \Delta\alpha = \alpha_f$ ($\Delta\alpha \approx \pm 0.05^\circ$)	$q_x \approx \text{const.}$ mainly scan q_z	vertical roughness information
Rocking scan Ω -scan Transverse-diffuse scan	$2\theta = \text{const.}$ sample is rocked	$\alpha_i + \alpha_f = \text{const.}$	$q_z \approx \text{const.}$ mainly scan q_x	in-plane roughness information
Detector scan Radial scan 2θ -scan	$\Omega = \text{const.}$ detector is moved	$\alpha_i = \text{const.}$		

Table E.1: Definition of different scan modes in the diffractometer, sample and reciprocal space coordinate systems [2, 5, 6].

E.2 Features in the X-ray reflectivity curve

As an example Figure E.2 plots the specular reflectivity curve modelled¹⁰ for a rough 120 nm thick rutile film deposited on an oxidized Si substrate. Different regimes can be distinguished. If the scan starts at very low angles the slope of the direct beam can be seen (not in the Figure). While the sample is turned into the beam the reflected intensity increases with a sine shape (footprint effect). Once the beam footprint is smaller than the sample the intensity reaches the plateau of total external reflection (very narrow in the figure). In the absence of absorption, the reflected intensity would be unity. At $\alpha_i = \alpha_c$ the reflected intensity is reduced to $\frac{1}{2}$ (neglecting absorption). For higher angles the mean intensity follows a α^{-4} power law (assuming smooth surface and interfaces) [6]. The surface roughness influences the slope of the over all decrease. The quick oscillations are called Kiessig fringes and are due to interference between interfaces of the TiO₂ layer. The wide oscillations are due to the SiO₂ layer located between the substrate and the oxide layer. Surface and interface roughness or intermixing has a damping effect on the Kiessig fringes of the corresponding layers.

¹⁰ The modelling was done with the REFLEX software, see Section E.3.4.

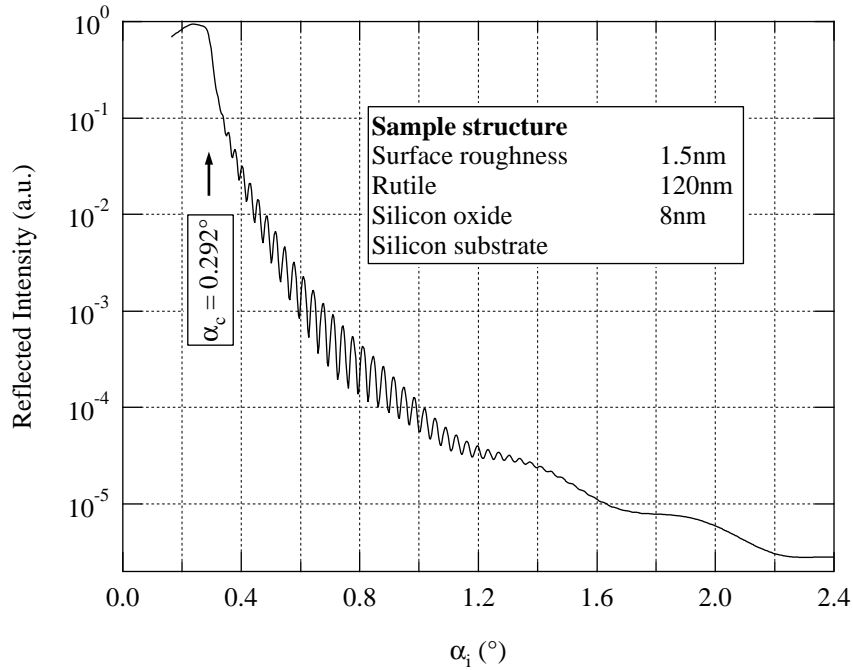


Figure E.2: Example of a XRR pattern modelled for a rutile layer on an oxidized silicon substrate.

E.2.1 Critical angle and density

The Henke-Gullikson-Davis database [9] was an important source of information. It can be found online under [10]. It contains the atomic scattering factors and corrections, and the optical constants δ and β for all the elements in a wide range of photon energies. In Table E.2 an overview of the respective values for the materials occurring in this work is given. For binary compounds the critical angle, wave-vector transfer and optical constants were calculated according to the formulae presented in this summary. The correction f' is small compared to $f^0 = Z$ and it is often neglected. The atomic density ρ_a in Equation E.9 is related to the electron density ρ_e by

$$\text{Equation E.14} \quad \rho_e = \rho_a \cdot Z$$

and to the mass density ρ by Avogadro's number N_A and the molar mass M

$$\text{Equation E.15} \quad \rho = \frac{M}{N_A} \rho_a$$

The mass density can be determined from the index according to

$$\text{Equation E.16} \quad \rho = \frac{M}{N_A Z} \cdot \frac{K^2}{2\pi R_e} \cdot \delta$$

and from the critical angle according to

$$\text{Equation E.17} \quad \rho = \frac{M}{N_A Z} \cdot \frac{K^2}{4\pi R_e} \cdot \alpha_c^2$$

In the case of the binary system TiO_x the atomic density ρ_a , the mass M and the atomic

scattering factor are replaced by the corresponding values for the TiO_x formula unit.

$$\text{Equation E.18} \quad Z_{\text{TiO}_x} = Z_{\text{Ti}} + x \cdot Z_{\text{O}} = 22 + x \cdot 8$$

$$\text{Equation E.19} \quad M_{\text{TiO}_x} = M_{\text{Ti}} + x \cdot M_{\text{O}} = (47.88 + x \cdot 16.00) \text{ g mol}^{-1}$$

Therefore, the determination of the mass density ρ depends on the chemical composition. The accurate determination of the critical angle α_c is not simple, because it demands a resolution in the range of 0.001° in α_i [5, 11]. From Equation E.17 the accuracy of the density determination from α_c may be estimated as

$$\text{Equation E.20} \quad \frac{\Delta\rho}{\rho} = 2 \frac{\Delta\alpha_i}{\alpha_c}$$

To achieve a precision in the density of $\Delta\rho = 0.04 \text{ g/cm}^3$ or 1 % if $\rho = 4 \text{ g/cm}^3$ an angle adjustment to a precision of $\Delta\alpha_i \leq 0.0015^\circ$ (at α_c of 0.3°) is needed. Therefore, the main error of a precise density determination is often caused by an inaccurate sample alignment [5]. Koiijma et al. [12, 13 and references therein] discuss the application of XRR for density determination.

Material	f'	f''	ρ (g/cm ³)	δ (10 ⁻⁵)	β (10 ⁻⁷)	α_c (°)	q_c (Å ⁻¹)
Rutile	---	---	4.25 [14]	1.296	6.61 [9]	0.292	0.0415
Anatase	---	---	3.89 [14]	1.186	6.17 [9]	0.279	0.0397
TiO	---	---	4.93 [8]	1.499 [9]	9.41 [9]	0.314	0.0447
Ti (Z = 22)	0.2433 [9]	1.86808 [9]	4.52 [8]	1.352 [9]	11.35 [9]	0.298 [9]	0.0424
O (Z = 8)	8.0523 [9]	0.03370 [9]	---	---	---	---	---
SiO₂	---	---	2.2 [9]	0.7136 [9]	0.921 [9]	0.217	0.0308
Si (Z = 14)	0.30 [9]	0.3248 [9]	2.33 [9]	0.7603 [9]	1.728 [9]	0.223 [9]	0.0318
Float glass	---	---	---	7.7 [6]	1.3 [6]	0.225	0.0320 [6]

Table E.2: Crystal densities ρ and corresponding parameters δ , β and critical angle α_c , and critical momentum transfer q_c for materials occurring in this work (for Cu K $_{\alpha 1}$ wavelength). For elements dispersion corrections in the atomic scattering factors are listed, too. Reference [10] is an online database which is based on [9]. Values without references were calculated from the given values.

E.2.2 Kiessig fringes and thickness

Once the beam enters the layer, multiple reflections at the lower and upper interfaces are possible. The resulting interference fringes are called Kiessig fringes. In reciprocal space the Kiessig fringes of a single layer film are uniformly spaced by Δq_z depending on the thickness

$$\text{Equation E.21} \quad t = \frac{2\pi n}{\Delta q_z} \approx \frac{2\pi}{\Delta q_z}$$

where n is the refractive index (Δq_z is considered inside the film) [1, 5]. When there are more layers, Fourier analysis of the Kiessig fringes provides estimates of the distances between interfaces [15-17].

The amplitude of the oscillations in the spectrum is proportional to the electron density difference between the film and the substrate. Density differences in the order of 2 % or greater are readily observed, while smaller density differences may require long data accumulation times to obtain a sufficient signal-to-noise ratio to observe the fringes [1].

E.2.3 Damping and roughness

Surface roughness causes an overall decrease of the specularly reflected intensity progressively with the angle, whereas buried interface roughness gives rise to a progressive damping of the interference fringes at higher scattering angles [1, 5]. Often a Gaussian-distributed roughness profile is assumed for modelling XRR curves. A measurement of a buried interface roughness is reliable for density differences of more than 5 % across the interface [1]. The assumption of a Gaussian distribution does not hold when the roughness is of the same order of magnitude as the layer thickness [6]. In specular scans the wave vector transfer is always perpendicular to the stratified structure. Off-specular diffuse scans provide more information about the surface and interface morphology such as lateral correlation length, fractal dimension and a distinction between interface roughness and graded interface profiles due to interdiffusion.

E.3 Methods of analysis

E.3.1 Data reduction

Diffuse scattering adds a background contribution to the specular scattering. This diffuse intensity is measured by a longitudinal scan with $\Delta\alpha \approx \pm 0.05^\circ$. The true specular reflectivity is obtained by subtracting the off-specularly reflected intensity. This correction is mainly visible in the slope at high α_i values. Therefore, without the subtraction the surface roughness is underestimated.

At incidence angle α_i the width of the sample surface illuminated by the beam, the footprint F , is given by

Equation E.22
$$F = \frac{B}{\sin \alpha_i}$$

where B is the beam width. For instance for $B = 100 \mu\text{m}$ and a critical angle of 0.3° one gets a minimum sample width of 20 mm. A flat region in the XRR curve just below the critical angle indicates that the footprint is smaller than the sample. Since this was not the case for most of the samples, a knife-edge was mounted close to the sample surface. This reduced the effective sample surface and restricted the beam width to roughly twice the sample to knife distance.

E.3.2 Kiessig fringe position

The positions of the interference minima in the reflectivity of a single layer of thickness t with smooth interfaces are given by [18]

$$\text{Equation E.23} \quad \frac{(2m-1)\pi}{t} = \sqrt{q_m^2 - q_c^2}$$

or

$$\text{Equation E.24} \quad q_m^2 = \left(\frac{\pi}{t}\right)^2 (2m-1)^2 + q_c^2$$

Where m is the order of the interference fringe and q_m the corresponding wave vector transfer. For interference maxima the term $(2m-1)$ is replaced by $2m$ [5]. Plotting q_m^2 versus the square of the Kiessig fringe order $(2m-1)^2$ yields the thickness t of a smooth single layer from the slope of the linear dependence and the critical wave vector transfer q_c from the axis intersection [5, 18].

E.3.3 Determining thickness and index from the Kiessig fringes

Rusli et al. [19] proposed an algorithm that allows the direct determination of the properties of a single layer on an unspecified substrate from the position of the interference fringes¹¹. From a recursive equation for the X-ray reflection coefficient they deduced the following error function

$$\text{Equation E.25} \quad F_m = \text{Re} \left[\sqrt{n^2 - \cos^2 \alpha_{i,m}} - \sqrt{n^2 - \cos^2 \alpha_{i,m-1/2}} \right] = \frac{\lambda}{4t}$$

where Re denotes the real part of the complex term in brackets, n is the refractive index of the layer, $\alpha_{i,m}$ ($\alpha_{i,m-1/2}$) is the incidence angle for the maximum (minimum) of the interference fringe of order m , λ is the X-ray wavelength and t the thickness of the layer. The right side is constant. With the correct index n the errors F_m will be close to each other and exhibit a minimum standard deviation. We can vary n and locate the value at which the standard deviation of F_m is a minimum. δ and β are related by a known constant

$$\text{Equation E.26} \quad \frac{\delta}{\beta} = \frac{Z + f'}{f''}$$

which is obtained from Equations E.9 and E.10. Thus δ and β can be determined from the index n . The thickness is obtained from Equation E.25 as

$$\text{Equation E.27} \quad t = \frac{\lambda}{4 \langle F_m \rangle}$$

where $\langle F_m \rangle$ is the mean of the set of F_m with a minimum standard deviation. The advantage of this algorithm is that it does not depend on modelling of the reflectivity curve.

¹¹ In the same article to other algorithms are proposed to determine the surface and interface roughness from the constructive and destructive interference envelopes.

E.3.4 Modelling of the XRR curves

XRR can be modelled either in the formalism of classical optics, assuming continuous media with dielectric boundaries, or in the formalism of diffraction¹², considering the material as a collection of scatterers. In the optical formalism Fresnel coefficients are used to calculate the reflection coefficients from stratified structures. The calculations can be done by a matrix approach similar to the one presented in Chapter 5 and Appendix A. An alternative often used for XRR is the recursive algorithm initially developed by Parratt [2, 20]. Both techniques ignore diffuse scattering [1].

In the present study the modelling was done with the REFLEX routines programmed by G. Vignaud and A. Gibaud [21]. It is especially useful to see directly the influence of every involved thickness, density or roughness parameter. The commercially available X-ray analysis software RAYFLEX (Rich. Seifert & Co.) was used also. It is based on the Parratt algorithm and assumes Gaussian roughnesses [22]. Both programs include corrections for limited resolution, beam width and footprint effects.

¹² Kinematical (Born approximation) and dynamical scattering theories and derivatives thereof.

References

1. E. Chason and T.M. Mayer, *Critical Reviews in Solid State and Materials Sciences* **22** (1997), 1.
2. K.N. Stoev and K. Sakurai, *Spectrochimica Acta B* **54** (1999), 41.
3. O. Durand, *Le Vide* **304** (2002), 387.
4. J. Als-Nielsen and D. McMorrow, *Modern X-ray physics*. John Wiley & Sons, Ltd., New York (2001).
5. V. Holý, U. Pietsch, and T. Baumbach, *High-Resolution X-ray Scattering from Thin Films and Multilayers*. Springer, Berlin (1999).
6. J. Daillant and A. Gibaud, *X-ray and neutron reflectivity: principles and applications*. 1st ed., Springer, Berlin (1999).
7. M. Aspelmeier, U. Klemradt, W. Hartner, H. Bachhofer, and G. Schindler, *Journal of Physics D* **34** (2001), A173.
8. *CRC Handbook of chemistry and physics*. 67th ed., CRC Inc., Boca Raton (1986).
9. B.L. Henke, E.M. Gullikson, and J.C. Davis, *Atomic Data and Nuclear Data Tables* **54** (1993), 181.
10. B.L. Henke, E.M. Gullikson, and J.C. Davis, *X-ray interactions: photoabsorption, scattering, transmission, and reflection at $E = 50\text{-}30000$ eV, $Z = 1\text{-}92$* . Lawrence Berkeley National Laboratory, http://www-cxro.lbl.gov/optical_constants/, Berkeley (1993).
11. W. Sirkel, *J. Appl. Phys.* **74** (1993), 1776.
12. I. Kojima and B. Li, *The Rigaku Journal* **16** (1999), 31.
13. I. Kojima, B. Li, and T. Fujimoto, *Thin Solid Film* **355-356** (1999), 385.
14. *PDF-database*. JCPDS, International centre for diffraction data (ICDD), 1601 Park Lane, Swarthmore, PA 19081, USA.
15. K.N. Stoev and K. Sakurai, *The Rigaku Journal* **14** (1997), 22.
16. E. Smigiel, A. Knoll, N. Broll, and A. Cornet, *Modelling Simul. Mater. Sci. Eng.* **6** (1998), 29.
17. E. Smigiel and A. Cornet, *Journal of Physics D* **33** (2000), 1757.
18. A. Richter, R. Guico, and J. Wang, *Review of Scientific Instruments* **72** (2001), 3004.
19. Rusli, K. Chew, S.F. Yoon, H.K. Chan, C.F. Ng, Q. Zhang, and J. Ahn, *International Journal of Modern Physics B* **16** (2002), 1072.
20. L.G. Parratt, *Phys. Rev.* **95** (1954), 359.
21. G. Vignaud and A. Gibaud, *RefleX, Specular Reflectivity*. 1.0 ed., Université du Maine, Faculté des Sciences, <http://lpec.univ-lemans.fr/reflex/reflex.htm>, Le Mans, France.
22. A. Schafmeister and M. Servidori, *Rayflex Software*. 2.29 ed., Rich. Seifert & Co., (1998).
23. L.S. Zevin and G. Kimmel, *Quantitative X-ray diffractometry*. 1st ed., Springer, Berlin (1995).
24. H.P. Klug and L.E. Alexander, *X-ray diffraction procedures for polycrystalline and amorphous materials*. 2nd ed., John Wiley & Sons, Ltd., New York (1974).
25. J.W.M. DuMond, *Phys. Rev.* **52** (1937), 872.
26. M. Schuster and H. Gobel, *Journal of Physics D* **28** (1995), A270.

Acknowledgements

I would first like to thank Dr. **Philippe Schmid** who was the supervisor for my thesis. I appreciated his vast scientific knowledge and valuable suggestions in many instructive discussions. I am grateful to Professor **Francis Lévy** for welcoming me in his group and for his support and interest in the advancement of this project. The financial support of the Swiss National Science Foundation and the EPFL is greatly acknowledged.

I thank all the friends and colleagues who have accompanied this work with stimulating discussions and experimental contributions. Among them I want to acknowledge in particular

- Dr. **Jürgen Geng**, Dr. **Nicolas Martin** and Dr. **Alain Bally** for instructing me in the sputtering techniques.
- Prof. **Pierre Stadelmann**, Dr. **Elena Martinez**, **Thomas La Grange**, Dr. **Cosmin Sandu**, **Daniele Laub**, Dr. **Maja Remskar** and Dr. **Daniela Dumitriu La Grange** for helping me to get further insight into the structure of my samples by electron microscopy investigations.
- Dr. **Daniel Ariosa**, Dr. **Matthieu Diserens**, **Simon Bühlmann**, **Thomas La Grange**, **Philippe Bugnon** and Dr. **Cathy Meunier**, for their help and fruitful discussions on X-ray diffraction techniques.
- Dr. **Rosendo Sanjinés** for his help with AFM and STM measurements.
- Dr. **François Bussy** for his support in the EPMA measurements.
- Dr. **Peter Hones**, Dr. **Oksana Banakh**, Dr. **Nicolas Martin** for introducing me to and helping me with ellipsometry and optical characterization.
- **Henri Jotterand** and **Laurent Braun** for the technical support in the laboratory.
- **Sebastien Tanniger** for all kind of help and trouble shooting inside and outside the lab.
- The apprentices **Eric Hofmann**, **Sylvain Marendaz** and **Christelle Crot** for their precise and reliable experimental assistance.
- **Claudine Gueissaz**, **Claude Zwicky**, **Christine Vuichoud** and **Suzanne Claudet** for their help with all administrative questions.
- Dr. **Andreas Schüler**, **Thomas La Grange**, **Sebastien Tanniger** and **Olivier Couteau** for their aid in the preparation of the present manuscript.
- **Ana Maria do Espirito Santo**, **Pierre-André Baudat**, Prof. **Abdou Djouadi**, **Rachid Lamni** and **Moushab Benkahoul** for interesting discussions.

Some of the people I have met in Lausanne are now very good friends of mine and I hope to meet them again many times in the future. I am grateful for their good spirits, encouraging words and the great time we spent together.

Very special thanks are dedicated to Dr. **Rosendo Sanjinés** for his invariably open door and to Dr. **Andreas Schüler** who helped me a lot as a personal coach with his experience and understanding of physical problems. Last but not least, I am grateful for the support of **my family** and above all I thank **Mirjam** for her patience, empathy and many encouragements.

THANK YOU!
Lausanne, February 2004
Simon Springer

Curriculum vitae

Name Simon Gerhard SPRINGER
Born March 5th, 1974 in Oakland, California
Nationality Swiss and American
Address CH-4424 Arboldswil, Switzerland
e-mail simon.springer@a3.epfl.ch

Education

08.1990 - 12.1993 Gymnasium Liestal, Switzerland
12.1993 Matura Typus C (majors in Mathematics and Physics)
10.1994 - 09.1999 Studies at the Institut für Physik, Universität Basel, Switzerland
11.1996 Vordiploma in Physics and Mathematics
10.1998 Certificate in Molecular Biology (Wahlfach Biologie II)
03.1999 Diploma in Physics with minors in Mathematics and Chemistry,
Philosophisch-Naturwissenschaftliche Fakultät, Universität Basel

Professional experience

02.1997 - 06.1997 Solid State Physics group, Vrije Universiteit VU, Amsterdam,
Netherlands: Internship in thin film technology and electrochemistry.
06.1997 - 10.1997 Low Temperature Installations group, Paul Scherrer Institute PSI,
Villigen, Switzerland: Internship in low temperature physics and
nuclear magnetic resonance.
07.1998 - 08.1998 National Synchrotron Light Source NSLS, Brookhaven National
Laboratory BNL, Upton, New York: Internship in X-ray diffraction
and infrared microscopy with synchrotron radiation.
05.1999 - 09.1999 ESCA-Group, Institut für Physik, Universität Basel, Basel, Switzerland:
Diploma thesis: *Characterization of Al-Ni-Si-oxides produced by
magnetron sputtering for their possible application as solar
absorber coatings.*
11.1999 - 02.2004 Institute of Physics of Complex Matter, École Polytechnique
Fédérale de Lausanne EPFL, Lausanne, Switzerland: Research and
teaching in the field of thin film technology, PVD, optical coatings
and characterization methods.

Languages First language German, fluent in English and French,
basics in Spanish, Dutch, Latin